UNIVERSITAT POLITÈCNICA DE CATALUNYA
BARCELONATECH
Departament d'Enginyeria Electrònica

MONITORING SWITCH-TYPE SENSORS AND POWERING AUTONOMOUS SENSORS VIA INDUCTIVE COUPLING. APPLICATION TO REMOVABLE SEATS IN VEHICLES

Tesi presentada per obtenir el títol de Doctor per la Universitat Politècnica de Catalunya

Joan Miquel Albesa Querol

Director: Dr. Manel Gasulla Forner

BARCELONA, 14 DE JUNY DE 2012

Per a l'Anna, el Miquel, la Sílvia, l'Adrià i la Cristina: la meva esposa, els meus pares i els meus germans.

Abstract

In vehicles, wiring sensors installed in rotating parts such as wheels or removable parts such as seats can be unfeasible or unpractical. Two examples are tire pressure monitoring systems (TPMS) mounted on the wheel rim and belt detectors found in removable seats. TPMS are already mandatory in USA and will be in the EU for vehicle types of category M1 or N1 granted as from 1 November 2012 or first registered as from 1 November 2014. Currently, TPMS are powered by primary batteries. However, as the desired target for the lifetime of batteries is about 10 years, the use of batteries is challenging. In addition, the final disposal of millions of batteries will create environmental impacts and hazards. As for the removable seats, some vans and minivans incorporate them in order to flexibly arrange their internal space. Some commercial models incorporate at most a seat belt detector for the removable seats. In order to avoid wiring the seats, in some vehicle models, a passive detection is performed via an inductive link. However, more intelligent systems will be required. From 2012, an NHTSA regulation (USA) requires the use of intelligent airbags that minimize the risk to infants and children. Intelligent airbags must be deployed depending on whether the passenger is an adult, an infant car seat is present, or the seat is empty. The sensors used for these intelligent airbags may require power to operate. For removable seats, one alternative, although not necessarily the best, is to use of batteries.

This thesis explores the feasibility of using inductive links for a vehicle application where wiring an electronic control unit (ECU) to the sensors or detectors becomes unfeasible or unpractical. The selected application is occupancy and belt detection in removable vehicle seats. Two ways of using inductive links are considered: 1) passive detection of the state of the seat detectors from a readout unit and 2) remote power transmission to detection unit and subsequent data transmission by wireless transceiver.

Inductive links have been widely proposed for sensors placed in harsh or inaccessible environments, where wiring is unpractical. Usually, the sensor forms part of an *LC* resonant network. The resonant frequency is dependent on the quantity to be measured and is estimated from a coupled reader. This thesis proposes the use of inductive links for switch-type sensors, i.e. those that can be roughly modeled as switches in response to the sensed parameter. In our case, occupancy and belt detectors behave as switch-type sensors. First, we present a comprehensive analysis for an arbitrary number of sensors. Secondly, we show the feasibility of using inductive links for occupancy and belt detection in removable vehicle seats. The state (open or closed) of the related sensors was attained by first measuring the equivalent resistance of the readout inductor and then estimating its resonant frequency. Commercial ferrite-core coils were used to increase the detection distance. Experimental tests were carried out using an

impedance analyzer connected to the readout coil and commercial seat detectors connected to the resonant network. The resistance value at the resonant frequency decreased with an increasing distance between the coupled coils. Even so, detection of the sensors' state was feasible at all tested distances, from 0.5 cm up to 3 cm.

The second proposed alternative consists on remote powering, via an inductive link, the electronic device where the seat detectors are connected. Resonant coupled coils were used in order to increase the powering distance range and the power efficiency. To drive the transmitting resonant network a commercial class D amplifier was used. Working frequency was restricted to 150 kHz. Commercial small-size magnetic-core coils were selected and their resistance and quality factor over frequency measured. At the receiving network, a rectifier and a voltage regulator were required to provide a DC voltage supply to the electronic device, i.e. the autonomous sensor. Four type of voltage regulators were compared from the point of view of the system power efficiency. Both a theoretical analysis and experimental results are presented. Results showed that shunt regulators provide the best power efficiency over the three other alternatives, which are linear series and switching buck and boost regulators. On the other hand boost regulators led to an unstable behavior of the system in most of the cases. The use of rechargeable batteries was also considered in order to increase the power efficiency. Achieved power efficiencies were around 40 %, 25 %, and 10 % for coil distances of 1 cm, 1.5 cm, and 2 cm, respectively, which is remarkable considering the inner diameter of the coils, 0.6 cm. Experimental tests also showed that the autonomous sensor, which included the seat detectors and a wireless transceiver, was properly powered up to coil distances of 2.5 cm. The data about the state of the sensors were wirelessly transmitted to a base unit.

Finally, different types of coils were assessed and the effect of metallic structures analyzed for the intended application. The final aim is, on the one hand, to increase the powering distance and, on the other hand, to minimize the influence of the metallic structures. Three different coil types, two with ferrite-core coils and one with an air-core coil were used. Numerical results showed that ferrite-core coils, in especial that with an ETD-core coil, are less affected by the presence of metallic structures. Experimental results showed that the air-core coils provided the a larger powering distance thanks to its much larger winding diameter, 6.5 cm. However, when approaching a metallic plate, the transferred power with the air-core coils to the load was insufficient for the intended application. On the other hand, ferrite-core coils barely noticed the presence of the metallic plate, achieving the ETD-core coils the highest powering distance, around 3 cm. As for the passive detection, the presence of a metallic plate below the primary air-core coil slightly affected the measured resistance values but detection for the four possible states of the seat detectors was still possible. A distance of 7.5 cm between the coils was successfully tested when using the air-core coils.

Resum

Algunes aplicacions a l'entorn de l'automòbil no són possibles si no és mitjançant la connexió sense fils dels seus dispositius a causa que el cablejat és difícil o inviable. Alguns exemples els trobem en el monitoratge de sensors situats en parts rotatòries, com les rodes, o en elements extraïbles, com els seients. Els sistemes de monitoratge de la pressió de l'aire en les rodes (TPMS) són d'obligat compliment als EUA i ho seran en breu també als països membres de la UE per als vehicles de categories M1 o N1 aprovats a partir de l'1 de novembre de 2012 o per als vehicles matriculats a partir de l'1 de novembre de 2014. Actualment, els sistemes TPMS existents al mercat estan alimentats per piles. Amb tot, la vida útil exigida per a les bateries és d'uns 10 anys, esdevenint el seu ús un autèntic repte. Un altre element en contra de l'ús de bateries és la directiva 2006/66/CE que limita el nombre màxim permès en els vehicles. D'altra banda, moltes furgonetes o mini furgonetes i vehicles familiars incorporen seients extraïbles amb l'objectiu d'aprofitar al màxim l'espai interior. Alguns models comercials incorporen en el seient extraïble el detector de cinturó de seguretat. Per evitar el cablejat, existeixen sistemes de detecció passiva mitjançant acoblament inductiu. A partir del present any 2012, una regulació de la agència nord-americana NHTSA requereix de l'ús de coixins de seguretat intel·ligents per minimitzar els riscos en nens. Aquests seients intel·ligents haurien de detectar si el passatger és un adult, una cadira infantil o si està lliure per evitar problemes ocorreguts en anterioritat amb els sistemes coixí de seguretat. Els sensors usats per a aquests coixins de seguretat intel·ligents requeririen d'energia per operar. Una opció per als seients extraïbles és la transmissió de potència via acoblament inductiu des del terra del xassís del vehicle fins al seient. També és possible usar l'acoblament inductiu per detectar l'estat de diversos sensors existents en els seients extraïbles mitjançant detecció passiva. Precisament, la detecció d'ocupació i de cinturó de seguretat en seients extraïbles ha estat seleccionada per aplicar la investigació present que consisteix, d'una banda, en el monitoratge de sensors de tipus commutat (dos possibles estats) via acoblament inductiu i, per una altra, en la transmissió mitjançant el mateix principi físic de la potència necessària per alimentar els sensors autònoms remots. En els dos casos, una primera bobina es fixaria en el seient extraïble, connectada als sensors, i una segona bobina se situaria sota la primera, en el terra del vehicle.

La detecció d'ocupació i del cinturó de seguretat per a seients extraïbles pot ser implementada amb sistemes sense fils passius basats en circuits ressonants de tipus LC on l'estat dels sensors determina el valor del condensador i, per tant, la freqüència de ressonància del circuit ressonant. Els canvis en la freqüència de ressonància són detectats per la bobina situada en el terra del vehicle. Un sistema intel·ligent, l'ECU del vehicle per exemple, connectat a aquesta bobina, determinarà l'estat dels sensors, avisant en conseqüència al conductor quan el seient extraïble estigui ocupat i el cinturó de seguretat descordat. S'ha aconseguit provar el

sistema en un marge de distàncies entre 0.5 cm i 3 cm. Els experiments s'han dut a terme fent servir un analitzador d'impedàncies connectat a una bobina primària i sensors comercials de seients per a l'automòbil connectats a un circuit ressonant remot.

La transmissió remota d'energia mitjançant acoblament inductiu s'ha utilitzat per a l'alimentació d'implants biomèdics i en sistemes RFID (passaports electrònics, targetes clau per accedir a l'interior dels edificis o als mateixos vehicles, …). En el nostre cas, la bobina situada en el terra del vehicle alimenta un dispositiu autònom situat en el seient extraïble. Aquest dispositiu monitorarà l'estat dels detectors (d'ocupació i de cinturó) i transmetrà les dades mitjançant un transceptor comercial de radiofreqüència o pel mateix enllaç inductiu. S'han avaluat les bobines necessàries per una freqüència de treball per davall de 150 kHz i s'ha estudiat quin és el regulador de tensió més apropiat per tal d'aconseguir una eficiència global màxima. Per conduir la potència des del circuit primari, s'ha dissenyat i implementat un circuit ressonant basat en un amplificador comercial de tipus D, mentre que el circuit ressonant remot inclou un rectificador i els abans esmentats reguladors de tensió per alimentar els sensors autònoms. Quatre tipus de reguladors de tensió s'han analitzat i comparat des del punt de vista de l'eficiència de potència. Els resultats teòrics i experimentals s'han presentat. Aquests resultats mostren que els reguladors de tensió de tipus lineal shunt proporcionen una eficiència de potència millor que les altres alternatives, els lineals sèrie i els commutats buck o boost. D'altra banda, els reguladors commutats de tipus boost tenen un comportament inestable en la majoria dels casos. L'ús de bateries recarregables han estat considerades per tal d'incrementar l'eficiència total del sistema. Les eficiències aconseguides han estat al voltant del 40 %, 25 % i 10 % per les bobines a distàncies 1 cm, 1.5 cm, i 2 cm, respectivament, que és remarcable considerant els diàmetres interns de les bobines, 0.6 cm. Les proves experimentals desenvolupades han mostrat que els sensors autònoms, als quals es va incloure els detectors de seients i un transceptor sense fils, han estat correctament alimentats fins a distàncies de 2.5 cm. Les dades sobre l'estat dels sensors han estat enviades remotament fins a un ordenador que n'ha processat les dades.

Finalment s'han analitzat els efectes del objectes metàl·lics en les proximitats de les bobines per a les dues tècniques inductives. L'objectiu final era, d'una banda, incrementar la distància transmesa, i de l'altra, minimitzar la influència de les estructures metàl·liques. Tres tipus diferents de bobines, dos amb nucli de ferrita i una amb nucli d'aire, han estat emprades. Els resultats numèrics han mostrat que les bobines amb nucli de ferrita sofreixen menys els efectes de les estructures metàl·liques disposades al seu voltant. Els resultats experimentals han mostrat que les bobines d'aire proporcionen una major distància degut a que el diàmetre del seu bobinatge és molt més gran, 6.5 cm. Tanmateix, quan s'ha apropat un pla metàl·lic, la potència transferida a la càrrega s'ha vist reduïda considerablement, essent insuficient per l'aplicació

pretesa. D'altra banda, s'ha demostrat que les bobines amb nucli de ferrita redueixen els efectes de les estructures metàl·liques, aconseguint una distància màxima de 3 cm. Pel que fa a la detecció passiva, la presència d'estructures metàl·liques en les proximitats de la bobina primària, afecta lleugerament la mesura dels valors de la resistència de base tot i que la detecció dels quatre estats possibles per al seient es manté invariable. Una distància de 7.5 cm entre bobines ha estat provada amb èxit fent servir bobines d'aire.

Aknowledgments / Agraïments

Primer de tot, donar les gràcies pel suport incondicional rebut de la meva família. En especial a l'Anna, la meva esposa, que ha estat amb mi en tot moment, sense dubtar ni un instant, aguantant tots els excessos i esforços del treball diari. Sense tu no hauria estat possible. Gràcies! Menció especial als meus pares, per haver-m'ho ensenyat tot, sobretot el valor de l'esforç i la superació, per no desistir i sempre ser-hi. Als meus germans, per alegrar-me la vida. A la resta de família: avis, àvies, tiets, tietes, cosins i cosines. A la gent de l'Hospitalet de Llobregat, Batea, Sorita i Agramunt, sempre presents.

Al meu director de tesi, Manel Gasulla, per ensenyar-me tant, per aguantar-me, per estar quan tocava i per la seva sinceritat i amistat.

Als companys del grup ISI: Mayte, Francesc, Delia, Rafael, Ernesto, Abraham, Jorge, Vicky i Joan. Al Carles Aliau, per la seva amistat i els seus consells tècnics i científics de gran valor. Als professors Òscar Casas, Marcos Quílez i Óscar López per respondre quan ha calgut. Al professor Ramon Pallàs pel seu suport. Al Francis López per la seva col·laboració incalculable. I en general a tota la resta.

I would like to thank to all my friends and colleagues at IMTEK, University of Freiburg, particularly to Fabian, Max, Ulrich and Adnan. I am very grateful with professor Leonhard Reindl and Thomas Jäger.

Per acabar, agrair a les institucions que m'han donat suport aquests anys: primer de tot la Universitat Politècnica de Catalunya (UPC), la Càtedra SEAT-UPC i la SEAT S.A a través de les "beques UPC-empresa", després l'AGAUR a través de les "beques predoctorals per a la formació de personal investigador (FI)", també al Ministerio de Educación a través de les "Subvenciones para favorecer la movilidad de estudiantes en doctorados" i per últim de nou a la UPC en aquest darrer any.

Table of Contents

Chapter 1 Introduction

Electronic devices in vehicles have been increasing since the 70s, with the introduction of the electronic voltage regulator and the electronic ignition system, and the first use of microprocessors [1]. Nowadays, an average vehicle contains around 60 microprocessors. Before the economic breakdown of the late 2000s, the prediction of market for automotive electronics was about 7 percent annually for at least a decade. This trend will not reemerge until the industry recovers [2].

Sensors were broadly included in automobiles in the late 80s with the adoption of airbags and nowadays serve all main application areas of a vehicle, i.e. the powertrain, chassis and body. In 2003, the overall sensor market was around $42.2 billion, and the automotive sensor market was around $10.5 billion, making it the largest of the market segments for sensors [3]. For the sensor market, the average annual growth rate is estimated at 4 to 5 percent, whereas for the automotive sensor market, the average annual growth rate ranges from 5 to 7.5 percent [2].

Wiring sensors installed in rotating parts such as wheels or removable parts such as seats can be unfeasible or unpractical. Two examples are tire pressure monitoring systems (TPMS) mounted on the wheel rim and belt detectors found in removable vehicle seats. TPMS systems alert the driver when the tires are at a low pressure, which affects safety and fuel consumption. TPMS are already mandatory in USA and will be in the EU for vehicle types of category M1 or N1 [4] granted as from 1 November 2012 or first registered as from 1 November 2014 [5]. Presently, TPMS are being mainly powered by primary batteries. As the required lifetime of the TPMS is of 10 years, the use of batteries is challenging. In addition, the final disposal of millions of batteries will create environmental impacts and hazards. Several works propose to harvest mechanical energy from the same wheel [6]-[8]. In [9] some energy harvesting alternatives for automotive applications are presented. In particular, for TPMS two companies are mentioned which avoid the use of batteries. One of them (Transense) proposes a surface acoustic wave (SAW) based technology whereas the other one (Visityre) uses an electromagnetic closed-coupling technology.

On the other hand, some vans and minivans incorporate removable seats in order to flexibly arrange their internal space. Some commercial models incorporate at most a seat belt detector for the removable seats. In order to avoid wiring the seats, a passive detection is performed via an inductive link. However, more intelligent systems will be required. As for 2012, an NHTSA regulation (USA) requires the use of intelligent airbags that minimize the risk to infants and children. Intelligent airbags must be deployed depending on whether the passenger is an adult, an infant car seat is present or the seat is empty. These airbags should avoid the problems

encountered with previous airbag systems [10]. The sensors used for these intelligent airbags may require some kind of power supply.

The objective of this thesis is to explore the feasibility of using inductive links for a vehicle application where wiring an electronic control unit (ECU) to the sensors or detectors becomes unfeasible or unpractical. The selected application is occupancy and belt detection in removable vehicle seats. Two ways of using inductive links are considered, which will be described in the ensuing sections along with the selected detectors.

1.1 Seat Occupancy and Belt Detection in Vehicles

1.1.1 Background

Passive safety systems in vehicles aim to reduce injuries of the occupants in an accident. Ref. [11] reports that the risk of fatal injuries is reduced by 45 % in cars and 60 % in vans just by using the seat belt. The use of SBR (Seat Belt Reminder) systems is effective in reminding the vehicle occupants to buckle up and is reported as one of the most effective ways in avoiding deaths and injuries in traffic accidents [12]. Therefore, the Euro NCAP (New Car Assessment Program) provides additional points to vehicles that incorporate SBR systems [13], thus facilitating the achievement of the maximum score (5 stars) for safety performance. SBR systems may also be used for the proper control on the deployment of other passive safety devices such as air-bags.

In the EU, an SBR system for the driver seat consists of a seat belt detector wired to an (ECU). The passenger front-seat additionally includes an occupancy sensor in order to activate a warning only when the passenger is present and not buckled up. Euro NCAP defines occupancy as use by an occupant larger, taller or heavier than a small female (5 percentile) [13]. Both, the occupancy sensor and belt buckle switch behave as switch-type sensors. Next, we describe the commercial detectors used in this work. Next, we describe the commercial detectors used in this work.

1.1.2 Detectors

Fig. 1.1 shows the occupancy and belt detectors. The commercial occupancy detector (IEE company) consists of a flexible sensor mat, which is inserted into the vehicle seat. The mat itself is composed of two sandwiched carrier sheets held together by an adhesive. Increased pressure on the sensor mat causes a large electrical resistance variation, from a very high resistance when the seat is empty to a very low resistance when the seat is occupied. Thus, the sensor can be roughly modeled as a switch (i.e. two states: short- and open-circuit), which allows detecting the presence of a passenger using a simple electronic interface. The seat belt

detector (TRW Sabelt) consists of a buckle and the corresponding buckle housing, which can also be modeled as a switch. An unbuckled or buckled up seat belt can be respectively modeled as a short- or open-circuit.

Fig. 1.1 Pictures of the belt (left) and seat occupancy (right) detectors employed in this thesis. Figures respectively taken from [14] and [15].

1.2 Inductive Links

As mentioned before, some vehicles incorporate removable seats. Wiring this type of seats can be unpractical and in this work we investigate instead the use of inductive links in two different ways. Fig. 1.2 shows a possible configuration of the removable seat, detectors, and coils. One of the coils is placed on the vehicle floor and the other one is attached under the seat.

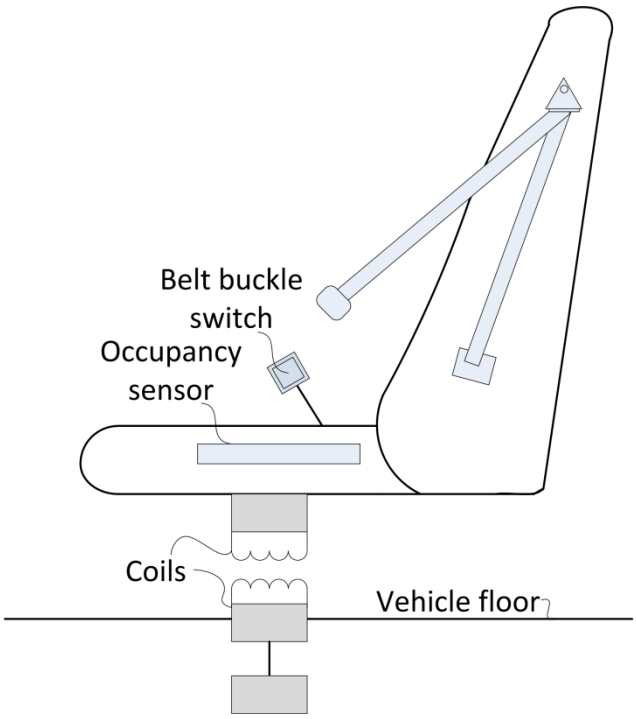

Fig. 1.2 A possible configuration of the removable seat, detectors, and coils.

1.2.1 Passive Inductive Links

Inductive links have been widely proposed to sense sensors, mainly capacitive, in harsh or inaccessible environments, where no wiring between the sensor and the processing unit is practicable [16]-[19]. For capacitive sensors, the sensor is disposed together with a coil forming an *LC* resonant circuit, whose resonance frequency changes according to the sensed parameter. The readout unit incorporates a coupled coil in order to wirelessly monitor the sensor.

The same principle has also been used to monitor switch-type (or threshold) sensors, i.e. sensors that can be roughly modeled as switches in response to the sensed parameter. The switch-type sensor is placed in series with a capacitor. Whenever the sensed parameter exceeds a given threshold, the sensor changes its state, thus modifying the equivalent capacitance and resonant frequency. In particular, in [20] and [21], a steel wire was used in order to monitor reinforcement corrosion in structures. The resonant network, which includes the sensor, is embedded within the concrete, near the reinforcement to be monitored. Whenever the reinforcement in the concrete is under corrosion, the steel wire is also corroded and breaks, thus changing the resonant frequency. A readout unit, which is fixed on the surface of the concrete structure, detects the change.

Switch-type sensors are also present in vehicles, e.g. for seat occupancy and belt detection. However, wiring removable vehicle seats, which are present in some vehicle models, to the ECU is unpractical. To solve this problem, inductive links have been proposed in a patent [22] for detecting the state of switch-type sensors in removable vehicle seats and are currently used in some vehicle models for belt detectors attached to the removable seats.

1.2.2 Inductive Power Transfer

Electrical power is transferred, in general, via a wired circuit by direct cable connections. With the development of modern technologies, the conventional power transfer technology is having difficulties in many applications, such as material handling systems, road lightings, battery charging systems, biomedical implants, etc.

The conventional methods to supply power to movable loads such as electrical trams or assembly lines are trailing cables, which has to follow the moving object to transfer power. Another method is a sliding bus bar, which can supply power to a fast moving object with less limitation. These conventional power delivery solutions are inappropriate in many applications with moving objects. The retracting trailing cables limit the speed and range of the displacement. Furthermore, the system increases its risk of failure and electric shock due to a long-term exposure to the weather. On the other hand, the sliding bus bar has electrical isolation

problems and the system safety and reliability is reduced because direct electrical contacts suffer from friction, spark and erosion problems.

There are applications, such as rotating tanks, or radio telescopes, where a continuous mechanical rotation is required on one side. An electric slip ring system is usually used to transfer power from a stationary base to a rotating side. Inside the slip ring, the mechanical contacts of its sliding brushes constrain the rotation speed, increase the friction and limit the displacement of the stationary and rotary parts.

Direct cable electrical power transfer is not feasible in some applications, in extremely clean or harsh environments. For instance, where the erosion of the cable could cause an explosion in some applications where flammable gases exist. In these cases contactless power transfer is needed.

Direct contact power transfer is not suitable either in some systems with special requirements, for instance, biomedical TET (Transcutaneous Energy Transmission) systems, because it imposes infection risks by having cables passing through the skin. Currently, batteries are the major solution to power low-power biomedical devices, but patients have to receive regular treatment for exchanging the batteries. The sufferings of the patient and the medical risk increase. In the cases where a higher power is required, powering by batteries is unpractical. Thus, for these applications is more suitable a contactless power transfer solution for battery charging without direct electrical contact or power delivery [31].

In addition, some new applications of contactless power transfer are also becoming popular, such as laptop computers, portable electric devices, consumer gadgets, and electrical vehicles. Therefore, there is a need to produce equipment and devices which can be charged without any cable connections.

Contactless power transfer has been known since Nikola Tesla started his experiments in 1890 [23]. Theoretically, power can be wirelessly transferred through many different methods: laser [24], electromagnetic waves [25], static electric field [26] and static magnetic fields [27].

Laser is an optical method which transfer power wirelessly. Many applications such as opto-couplers use this method which converts first the electric power to light for emission. After being received, the laser beam is then transferred back to electric power. This method requires the laser transmitter and receiver to be perfectly aligned, meaning it is not suitable for transferring power to moving devices. In addition, a direct line of sight is necessary. The technology is also very sensitive to the environment because the intensity of the laser beam decays quickly in air.

Transferring high power wirelessly is also feasible using electromagnetic waves [28]. Experiments using microwaves in the tens of kilowatts have been done in [29]. However, this power transfer technology presents difficulties for commercial products, due to the large size and complexity of the devices involved, a part of human and equipment safety issues.

Another contactless power solution is via electric field coupling, which is known as CPT (Capacitive Power Transfer). Two plates form a capacitor which allows powering across an air gap. The limitation of maximum electric field intensity and a low permittivity in the air channel [30] are the main limits of CPT. Unless very high permittivity dielectric materials are used as the medium between the plates, the low power transfer capability in air makes CPT inappropriate for high power and large gap applications.

Finally, wireless power transfer is can be achieved via magnetic fields. The simplest example of contactless energy transfer is the electrical transformer. However, remote movements are not allowed because the method is not really contactless due to the absence of an air gap; primary and secondary coils are tightly coupled. Inductive power transfer, termed IPT, has been proposed in order to transfer power across air gaps [31]. In general, IPT technology has a better performance than CPT technology [32].

The wireless power transfer technologies presented have advantages and constraints. However, in general, IPT technology seems one of the most feasible methods. IPT technologies are of interest for many research groups and industrial companies, which after many years of research and development have released many successful commercial applications. In fact, IPT is now being considered as a cost effective alternative in a broad range of areas. Both high- and low-power applications have been reported. High-power transfer includes battery recharging of electrical vehicles [33] and a broad range of industrial applications [34]-[40] whereas low-power transfer includes portable consumer electronic products [41]-[42]. IPT can also be an option for seat occupancy and belt detection in removable vehicle seats, being this topic explored in this thesis.

1.3 Scope of the Thesis

In vehicles, wiring sensors placed in removable or rotating parts to the ECU can become unpractical or unfeasible. This thesis proposes the use of inductive links for one of those applications such as occupancy and belt detection in removable vehicle seats. Two alternatives are considered: 1) passive sensing of the state of the seat detectors from a readout coil, and 2) remote power transmission to the detection unit and subsequent data transmission by a wireless transceiver. Next, a short description of the remaining chapters and annexes of the thesis is presented.

Chapter 2 presents the physical principles of magnetic induction. The fundamental laws of electromagnetism are reviewed and the relevant parameters involved in the scope of the thesis such as self-inductance, mutual inductance and coupling factor are presented. Some basic inductor models are introduced. Part of this chapter is devoted to finite element modeling of coils to calculate their self-inductances and mutual inductances with other coils. Finally we provide a summary of the regulations of the International Commission on Non-Ionizing Radiation Protection (ICNIRP) concerned with the health effects of electromagnetic field exposure.

Chapter 3 proposes the use of inductive links for switch-type sensors, i.e. those that can be roughly modeled as switches in response to the sensed parameter. First, we review the most relevant techniques proposed in the literature for the wireless readout of passive *LC* sensors. Then, one of the techniques is selected which estimates the value of the sensed parameter by first measuring the equivalent resistance of the readout inductor and then searching its resonant frequency. The technique is extended and a comprehensive analysis is presented for an arbitrary number of switch-type sensors. Later on, we show the feasibility of using the proposed approach for occupancy and belt detection in removable vehicle seats, where wiring is unpractical. Ferrite-core coils are used to increase the detection distance. Experimental tests are carried out using an impedance analyzer connected to the readout coil and commercial seat detectors connected to the resonant network. The resistance value at the resonant frequency decreases with an increasing distance between the coupled coils. Even so, detection of the sensor's state is feasible at all tested distances, from 0.5 cm up to 3 cm.

Chapter 4 proposes the use of inductive links for powering autonomous sensors and in particular for the intended application, i.e. occupancy and belt detection in removable vehicle seats, where wiring the seat sensors is unpractical. Resonant coupled coils are used in order to increase both the powering distance and the power efficiency. Analytical expressions are obtained and relevant parameters identified. Small-size magnetic-core commercial coils are selected and their resistance and quality factor over frequency measured. These parameters are used to perform computations, founded on the analytical expressions, of the received power versus distance. Working frequency is restricted to 150 kHz and the power required by the autonomous sensor was assumed of 100 mW. Experimental results agreed with computations. To drive the transmitting resonant network a commercial class D amplifier was used whereas the receiving network included a rectifier and a voltage regulator for powering the autonomous sensor. Powering distance is maximized when using a resonance frequency of 40 kHz with coils of 1 mH at the transmitter and of 10 mH at the receiver. A distance of 2.5 cm was achieved, i.e. more than four times the inner diameter of the coils. In addition, four type of voltage regulators are compared from the point of view of the system power efficiency. Both a theoretical analysis

and experimental results are presented. Results showed that shunt regulators provide the best power efficiency over the three other alternatives, which are series regulators and switching buck and boost regulators. The use of rechargeable batteries is also considered and found to increase the system performance.

Chapter 5 extends the work in Chapter 3 and Chapter 4 by the use of different types of coils and the assessment of the effects of metallic structures over the inductive link. The use of magnetic core material in the coils mitigates the effects of metallic structures.

The last chapter 6 summarizes the main contributions of the thesis.

There are also five appendices. Appendix A shows the calculation of the measurement uncertainty of the impedance analyzer used for the experimental tests in Chapter 3. Appendix B, C, and D add new results to that of Chapter 4. Finally, Appendix E provides a brief assessment on the accomplishment of the ICNIRP regulations.

Chapter 2 Magnetic Induction

This chapter covers the physical background of magnetic induction. The fundamental laws of electromagnetism are reviewed and are applied to analyze and model inductively coupled systems. The terms self-inductance, mutual inductance and coupling factor are defined and some basic inductor models are introduced. Another part of this chapter is devoted to finite element modeling of coils in order to numerically calculate their self-inductances and mutual inductances with other coils. The final part intends to provide a summary of the health effects of electromagnetic field exposure evaluating the regulations from the ICNIRP.

2.1 Maxwell Equations

Maxwell's equations relate the electric and magnetic fields vectors $\vec{E}$ and $\vec{B}$ and their sources, which are electric charges and currents. Two kinds of electric field are encountered in the four Maxwell's Equations: the electrostatic field produced by electric charges and the induced electric field produced by a varying magnetic field [43].

2.1.1 Gauss's Law for Electric Fields

The electric flux through a closed surface A is equal to the charge in the enclosed volume, i.e.

$$Q = \int_V \rho dV = \varepsilon_0 \oint_A \vec{E} d\vec{A} \tag{2.1}$$

where ρ is the total enclosed charge density, ε_0 is the electric permittivity of vacuum, V is the volume enclosed by the surface, $\vec{E}$ is the electric field, $d\vec{A}$ is the differential of surface area and Q is the total charge contained in that surface [44].

Another way to express this law is with the differential form

$$\vec{\nabla}\vec{E} = \frac{\rho}{\varepsilon_0} \tag{2.2}$$

which states that the electric field produced by electric charges diverges from positive charges and converges upon negative charges. The only places at which divergence of the electric field is not zero are those locations at which charge is present [45].

2.1.2 Gauss's Law for Magnetic Fields

The fact that no magnetic monopoles have been found suggests that the magnetic field is source-free. The total magnetic flux through a closed surface A vanishes, i.e.

$$\oint_A \vec{B} d\vec{A} = 0 \tag{2.3}$$

where $\vec{B}$ is the magnetic flux density.

Another way to express this law is with the differential form

$$\vec{\nabla}\vec{B} = 0 \tag{2.4}$$

which states that the divergence of the magnetic field at any point is zero [45].

2.1.3 Faraday's Law

This law states that a change of the magnetic flux through a conductor loop will cause a voltage at the ends of the conductor. If the ends of the conductor are connected, a current flows in the conductor. The induction theorem may be written in general form as follows

$$emf = \int_C \vec{E} d\vec{l} = -\frac{d}{dt}\int_A \vec{B} d\vec{A} \tag{2.5}$$

The differential form of the Faraday's law is given by

$$\vec{\nabla} \times \vec{E} = -\frac{\partial \vec{B}}{\partial t} \tag{2.6}$$

which states that a circulating electric field is produced by a magnetic field that changes with time [45].

2.1.4 The Ampere-Maxwell Law

This law is defined as

$$\oint_C \vec{B} d\vec{l} = \mu_0 \left(I + \varepsilon_0 \frac{d}{dt}\int_A \frac{d\vec{E}}{dt} d\vec{A} \right) \tag{2.7}$$

where μ_0 is the vacuum permeability.

The differential form of the Ampere-Maxwell law is

$$\vec{\nabla} \times \vec{B} = \mu_0 \left(\vec{J} + \varepsilon_0 \frac{\partial \vec{E}}{\partial t} \right) \tag{2.8}$$

where $\vec{J}$ is the total electric current density. Eq (2.8) states that a circulating magnetic field is produced by an electric current and by an electric field that changes with time [45].

2.2 Magnetic Field

Magnetic fields are produced by moving electric charge. The Biot Savart law allows the calculation of $\vec{B}$ due to wire-shaped conductors of arbitrary geometry. In reference to Fig. 2.1, the contribution at a specific point *P* from a small element of electric current is given by:

$$d\vec{B} = \mu_0 \frac{Id\vec{l} \times \hat{r}}{4\pi r^2} \tag{2.9}$$

where *I* is the current through the small element, $d\vec{l}$ is a vector with the length of the current element and pointing in the direction of the current, $\hat{r}$ is an unit vector pointing from the current element to the point P at which the field is calculated, and *r* is the distance between the current element and P.

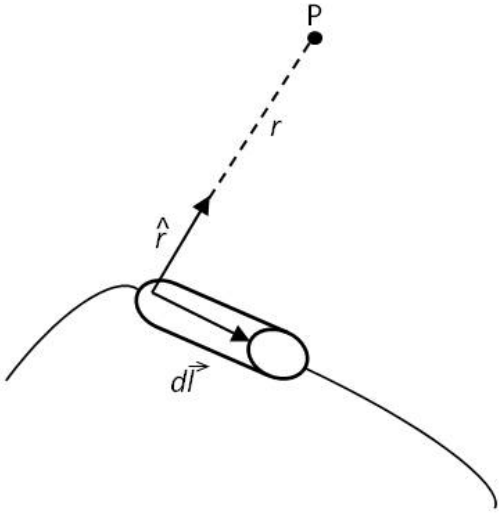

Fig. 2.1 Geometry for the Biot Savart law.

For this work, conductor loops (coils) are of special interest as they will be used both for passive sensing (Chapter 3) and remote powering (Chapter 4). Considering the circular loop of Fig. 2.2 of radius *r* and current *I*, from (2.9) we obtain that the $d\vec{B}$ generated by an element of current $Id\vec{l}$, in the *x* axis, is [46]

$$d\overrightarrow{B_x} = \frac{\mu_0 I r d\vec{l}}{4\pi\sqrt{(r^2 + x^2)^3}} \tag{2.10}$$

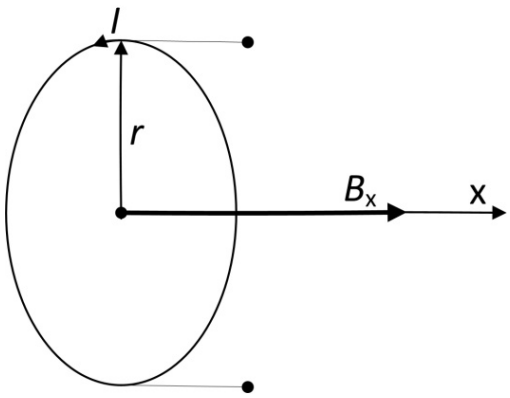

Fig. 2.2 Conductor loop of radius *r* with a current *I*. The magnetic field is evaluated across the *x* axis.

By symmetry, only the x axis component of $\vec{B}$ must be taken into account. Thus, by integrating eq. (2.10) along the circular loop, we obtain

$$B_x = \frac{\mu_0 I r^2}{2\sqrt{(r^2 + x^2)^3}} \tag{2.11}$$

Along the x axis, $B_x = \mu_0 I/2r$ at $x = 0$ and falls off as $1/x^3$ for $x^2 >> r^2$.

We can use the above result to calculate B on the axis of a solenoid such as that of Fig. 2.3.

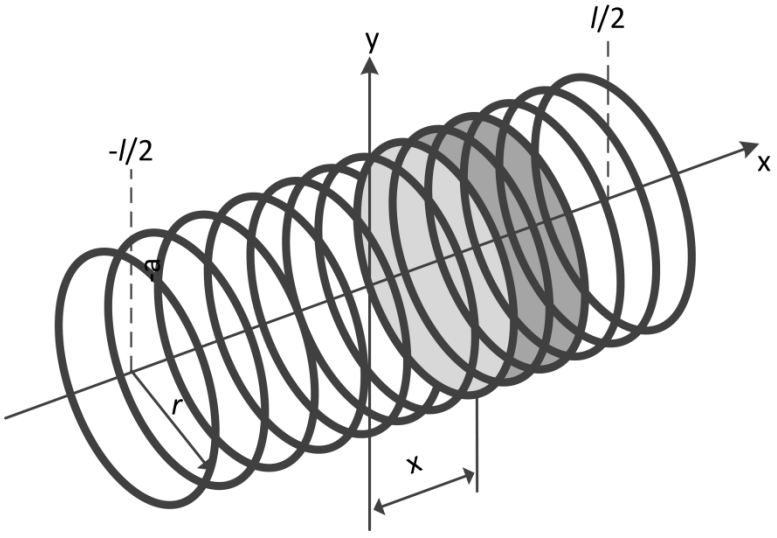

Fig. 2.3 Representation of a solenoid of length *l* and radius *r*, across the *x* axis [47].

Considering a solenoid of length l with N close-wound turns, and radius r, we obtain at the center of the solenoid axis [46],

$$B_x(x = 0) = \frac{\mu_0 N I r^2}{2l} \int_{-l/2}^{l/2} \frac{dz}{\sqrt{(r^2 + x^2)^3}} = \frac{\mu_0 N I}{2\sqrt{r^2 + (l/2)^2}} \tag{2.12}$$

and at the ends of the solenoid axis

$$B_x(x = \pm l/2) = \frac{\mu_0 N I r^2}{2L}\int_0^l \frac{dz}{\sqrt{(r^2 + x^2)^3}} = \frac{\mu_0 N I}{2\sqrt{r^2 + (l)^2}} \tag{2.13}$$

Thus, the magnetic flux density is larger at the center than at the ends. For a long solenoid, i.e. $l >> r$

$$B_x(x = 0) = 2B_x(x = \pm l/2) = \mu_0 N' I \tag{2.14}$$

being $N' = N/l$ the number of coil turns per unit length. The value of B_x at x = 0 can also be attributed at internal points on the axis remote from the ends . Further, this result can also be obtained by applying the Ampere's law. On the other hand, for very short solenoids, i.e. $l << r$

$$B_x(x = 0) = \frac{\mu_0 N I}{2r} \tag{2.15}$$

which equals (2.11) at $x = 0$ multiplied by N.

A particular case of interest is a Helmholtz coil, which generates a region of nearly uniform magnetic field. It consists of two identical circular magnetic coils that are placed symmetrically one on each side of the experimental area along a common axis, and separated by a distance equal to the radius R of the coils. Each coil has N turns and carries an equal electrical current I flowing in the same direction as can be seen in Fig. 2.4.

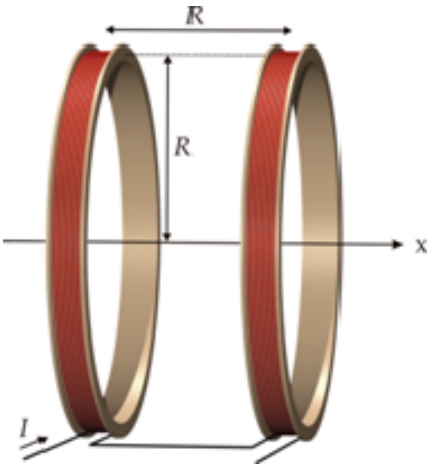

Fig. 2.4 Helmhotz Coil picture [from Wikipedia].

Then, at the midpoint between the coils, the magnetic flux density can be calculated from (2.11) considering the contribution of two coils, N loops and $x = R/2$, obtaining

$$B = \left(\frac{4}{5}\right)^{\frac{3}{2}} \frac{\mu_0 NI}{R} \tag{2.16}$$

2.3 Coil Self-inductance

The magnetic flux through a surface *A* is given by

$$\Phi = \int_A \vec{B} d\vec{A} \tag{2.17}$$

A circuit carrying a current *I* is linked by its own magnetic flux. The ratio

$$L = \frac{\Phi}{I} \tag{2.18}$$

is termed the *self-inductance* of the circuit and depends solely on the geometry of the circuit. From (2.5), (2.17) and (2.18), the induced voltage across the circuit due to changes of *I* with the time is

$$V_{ind} = -\frac{d\Phi}{dt} = -L\frac{dI}{dt} \tag{2.19}$$

The negative sign means that this voltage opposes the change in current. A particular circuit of interest is a coil. If the coil contains *N* turns, the total magnetic flux through the coil is *N* times the flux through each turn. That is

$$\Phi = N \int_A \vec{B} d\vec{A} \tag{2.20}$$

where *A* is the area of the flat surface bounded by a single turn. A single turn of a multi turn coil is not closed, so a single turn cannot actually bound a surface. However, if a coil is tightly wound a single turn is almost closed, and *A* is the area of the flat surface that it bounds.

The value of the self-inductance can be approximately calculated for some simple coil shapes. Here, we will present some derivations for circular loops and solenoids.

For a conductor loop with *N* turns, assuming that the magnetic flux density is constant and equal to (2.15) through the loop surface *A*, we obtain that the magnetic flux is

$$\Phi = \frac{\mu_0 N^2 IA}{2r} = \frac{\mu_0 N^2 \pi I r}{2} \tag{2.21}$$

and substituting in (2.18) we obtain

$$L = \frac{\mu_0 N^2 \pi r}{2} \tag{2.22}$$

For a long solenoid, assuming that the magnetic flux density is constant and equal to eq. (2.14), we obtain

$$L = \frac{\mu_0 N^2 A}{l} = \frac{\mu_0 N^2 \pi r^2}{l} \tag{2.23}$$

The self-inductance of a short solenoid is smaller and can be multiplied by a factor K that is a function of the ratio r/l. In [46] a table shows the relationship between r/l and the factor K for different values of r/l. Thus:

$$L = K \frac{\mu_0 N^2 \pi r^2}{L} \qquad K \leq 1 \tag{2.24}$$

When the solenoid has a magnetic core with a relative permeability μ_r, the self-inductance is given by

$$L = \frac{\mu_0 \mu_{ef} N^2 \pi r^2}{l} \tag{2.25}$$

where μ_{ef} is the effective permeability, which will be always lower than μ_r. The value of μ_{ef} asymptotically converges to μ_r for increasing values of L. Fig. 2.5 shows curves of μ_{ef} (in the graph μ_r) versus the ratio l/d, being l and d the length and diameter of the solenoid, respectively, for different values of μ_r (μ_i in the graph). As can be seen, μ_{ef} nearly equals μ_r for $l > \mu_r \times d$.

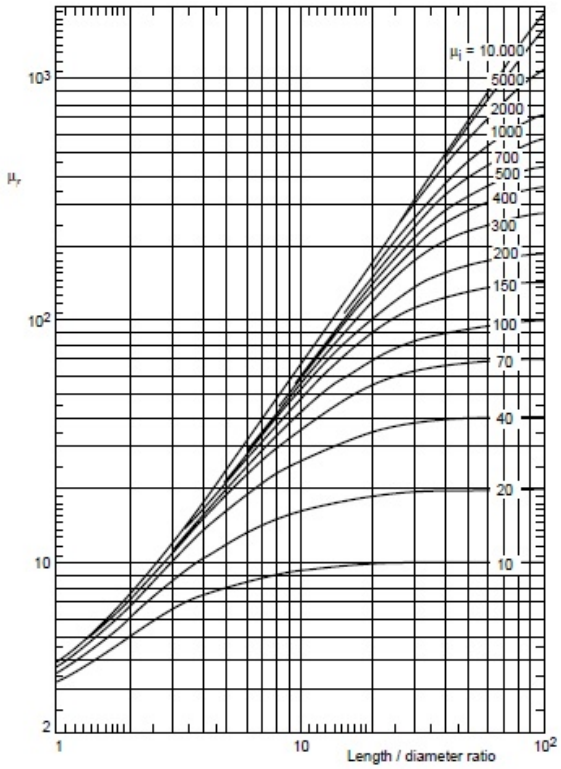

Fig. 2.5 Effective Permeability of the solenoid as a function of the length to diameter ratio with material permeability as a parameter [48].

More exact formulas for coils and solenoids can be found in [49] and [50].

2.4 Coil Model

An actual model of a coil must include, apart from the self-inductance, a parasitic series resistance and capacitance, such as shown in Fig. 2.6.

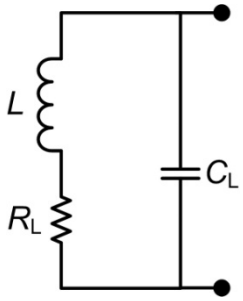

Fig. 2.6 Coil circuit model.

The resistor R_L represents the coil losses corresponding to the ohmic dissipation in the wire, the magnetic hysteresis of the coil core, and the skin and proximity effects. The parasitic capacitance C_L in Fig. 2.6 corresponds to the inter-winding capacitance existing between coil turns, of the same layer or different layers, and the turn-to-core and turn-to-shield capacitances. This parasitic capacitance appears in parallel to the coil inductance and provokes a parasitic resonance. Fig. 2.7 shows a general graph of the modulus and phase of the impedance of a coil.

The resonance frequency is an important parameter because limits the operating frequency of the coil.

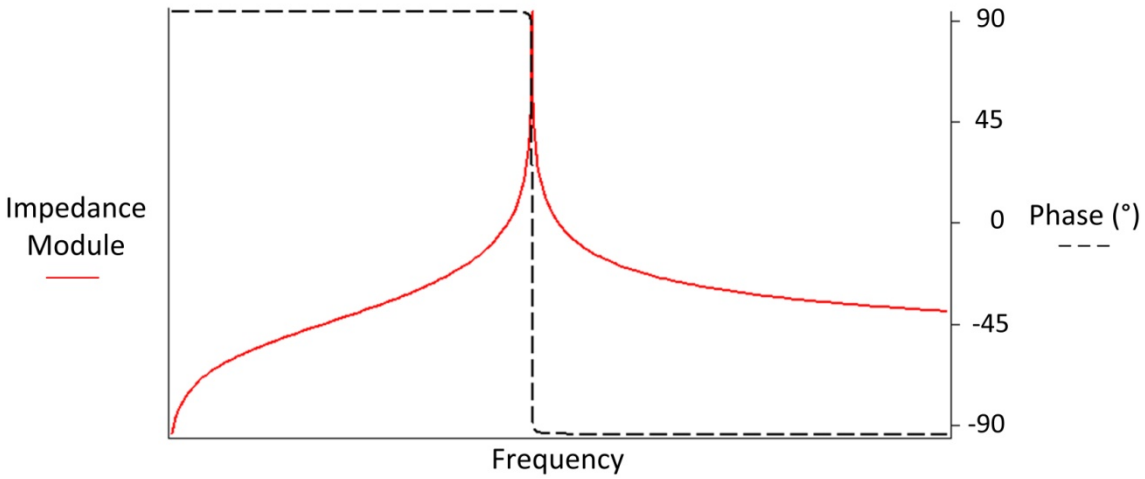

Fig. 2.7 Impedance module and phase of a coil modeled as in Fig. 2.6.

The skin and proximity effects express two identical effects with a different cause. Their influence on the winding resistance is important at higher frequencies because it reduces the active wire cross-section. The skin effect is caused by the internal AC magnetic field in a current-conducting wire. This field pushes the current charges to the outer layer near the surface of the conductor. Most of the current then flows where it is encircled by the smallest number of flux lines, i.e. the outer conductor surface. The skin depth (δ) is that distance below the surface of a conductor where the current has diminished to an 1/e factor of its value at the surface and is given by

$$\delta = \frac{1}{\sqrt{\pi\sigma\mu f}} \tag{2.26}$$

where f is the frequency, and σ and μ are respectively the conductivity and permeability of the wire conductor.

From [49] and [51], two corrected expressions for the coil resistance can be obtained depending on the working frequency and thus on the value of δ.

If $\delta > R/2$

$$R_{wire} = R_{DC}[1 + \frac{1}{3}\left(\frac{R}{2\delta}\right)^4] \tag{2.27}$$

If $\delta < R/2$

$$R_{wire} = R_{DC}[\frac{R}{2\delta} + \frac{1}{4} + \frac{3}{64}(\frac{2\delta}{R})] \tag{2.28}$$

where

$$R_{DC} = \frac{l}{\sigma\pi R^2} \tag{2.29}$$

is the dc resistance of a wire with radius R and length l. Thus, skin effect is more relevant when the skin depth is smaller than the wire diameter. The low-frequency wire resistance is proportional to a constant plus a quadratic frequency term. The high frequency expression when $R/2\delta >> 1$ can be expressed as

$$R_{wire} \approx R_{DC}\frac{R}{2}\sqrt{\pi\mu\sigma f} \tag{2.30}$$

Thus, R_{wire} increases with the square root of the frequency [49], [52], [53].

The current-redistribution effect is called proximity effect when is caused by the magnetic fields of currents in nearby conductors. This effect adds to the skin effect and makes the resistance increase even more prevalent. The relation between frequency and skin depth entirely depends on the given geometry and cannot be as simply expressed as for the skin effect. The power loss that is induced in a conductor is given by

$$P_{eddy} = \frac{\sigma\omega^2 B^2 t^2 V}{24} \tag{2.31}$$

where σ is the conductivity of the winding of the wire, B is the magnitude of the magnetic field in the conductor, V is the volume of the winding wire and t the thickness of the wire [51].

Finally, the hysteresis in the *B–H* curve of a magnetic material is responsible for the magnetic losses that warm up coil cores. The area enclosed by the *B-H* curve is a measure for the magnetic energy lost during one cycle. The hysteresis losses are proportional to the frequency and to the magnetic flux density. Fig. 2.8 shows a generic graph representing the hysteresis in the *B–H* curve.

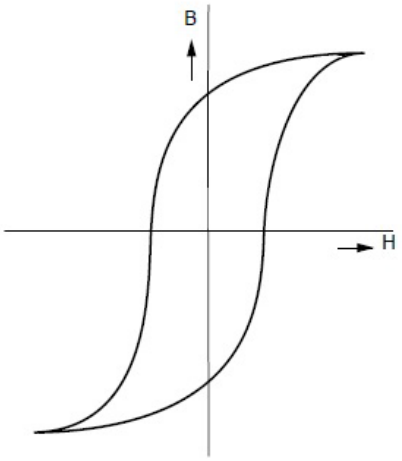

Fig. 2.8 Hysteresis in the B-H curve.

Based on results obtained by experiments with different ferromagnetic materials with sinusoidal currents, Charles Steinmetz proposed the empirical formula for calculating hysteresis loss analytically. The hysteresis loss per unit volume is given by

$$P_{hysteresis} = K_h f B^{\mathrm{n}} \tag{2.32}$$

where, the coefficient K_{h} depends on the material, n (known as Steinmetz exponent), may vary from 1.5 to 2.5, and B is the magnitude of the magnetic field within the conductor. For copper it may be taken as 1.6 [52], [53].

Overall, the coil resistance can be expressed as

$$R_L = R_{wire} + \frac{P_{hysteresis} + P_{eddy}}{I_{R_L}^2} \tag{2.33}$$

where I_{RL} is the current circulating thoroughly the coil.

The skin and proximity effects can be decreased by assembling the conductor from a number of thoroughly interwoven strands of thin wire connected in parallel at their ends and insulated throughout the rest of their length [49]. Such a stranded cable is called a Litz conductor. If the stranding is properly done, each wire links, on the average, with the same number of flux lines as each other wire, and the current divides evenly among the strands. If at the same time each strand is of small diameter, it will have relatively little skin effect over its cross section. Practical Litz conductors are very effective at frequencies below about 1 MHz. As the frequency becomes higher, the benefits disappear because the capacitance between the strands allows the current to hop across the strand insulation.

Coil inductance decreases with the frequency because skin and proximity effects change the current distribution. This redistribution occurs only inside the cross section of the coil wire and

the overall current flow remains unchanged. Whenever the diameter dimensions of the coil are much larger than the diameter of the wire, which is usually the case, the coil inductance does not noticeably change [51].

2.5 Quality Factor

The quality factor of a coil is the ratio of the imaginary part of its impedance to the real part and indicates the rate of stored energy relative to its energy loss. Assuming that the working frequency range is well below the resonant frequency shown in Fig. 2.7, the quality factor Q can be defined as

$$Q = \frac{\omega L}{R_L} \tag{2.34}$$

In [51] the self-inductance and the dc resistance of the coil are expressed, considering a fixed volume for the winding wire, as

$$\begin{aligned} R_{\mathrm{L}} &= N^2 R_{L,0} \\ L &= N^2 L_0 \end{aligned} \tag{2.35}$$

where $R_{\mathrm{L},0}$ and L_0 are the single-turn dc resistance and self-inductance, respectively. With these considerations, the authors make the assumption of constant quality factor irrespectively of the value of N.

The use of ferrite core coils lead to higher values of L. Whenever the hysteresis losses due to the ferrite core keep relatively low with respect to the other losses, a higher value of Q is achieved.

2.6 Mutual Inductance M

When two coils are close enough, a current I_1 in one coil L_1 sets up a nonnegligible magnetic flux Φ_{12} through the other coil L_2. The ratio

$$M_{12} = \frac{\Phi_{12}}{I_1} \tag{2.36}$$

is termed *mutual inductance*, being

$$\Phi_{12} = k_{12}\Phi_1 \frac{N_2}{N_1} \tag{2.37}$$

where the factor k_{12} accounts from the fraction of the magnetic flux generated by coil L_1 intercepted by coil L_2, and N_1 and N_2 are respectively the number of turns of coils L_1 and L_2. Substituting (2.37) in (2.36) we obtain

$$M_{12} = k_{12} L_1 \frac{N_2}{N_1} \tag{2.38}$$

The same procedure can be followed when generating a current in coil L_2. Thus,

$$M_{21} = k_{21} L_2 \frac{N_1}{N_2} \tag{2.39}$$

These constants are equal as can be demonstrated by using the reciprocity theorem which combines Ampere's law and the Biot Savart law. So,

$$M_{12} = M_{21} \equiv M = k\sqrt{L_1 L_2} \tag{2.40}$$

where the mutual inductance M only depends on the geometrical properties of the two coils and k is the coupling factor. The value of k can range from $k = 0$ (uncoupled coils) to $k = 1$ (maximum coupling). A high value of k is found in transformers whereas a low value of k is found in loose coupling applications such as those presented in this thesis.

The induced voltage in coil L_2 due to a current I_1 in coil L_1 is given by

$$V_{ind2} = -M \frac{dI_1}{dt} \tag{2.41}$$

whereas the induced voltage in coil L_1 due to a current I_2 in coil L_2 is given by

$$V_{ind1} = -M \frac{dI_2}{dt} \tag{2.42}$$

In section 2.3 the self-inductance of a circuit was defined. Both effects, self-inductance and mutual inductance, act at the same time in a circuit with a coupled pair of coils, L_1 and L_2. The voltage induced in each coil comes from the current in the own coil and from the current of the coupled coils. In reference to the circuit of Fig. 2.9, we can derive the following expressions

$$\begin{aligned} V_1 &= L_1 \frac{dI_1}{dt} - M \frac{dI_2}{dt} \\ V_2 &= -L_2 \frac{dI_2}{dt} + M \frac{dI_1}{dt} \end{aligned} \tag{2.43}$$

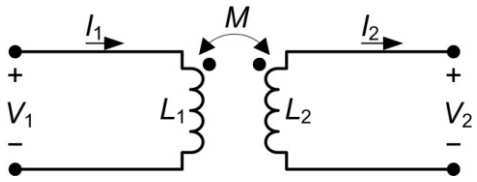

Fig. 2.9 Circuit of a pair of coupled coils.

Hereafter, the points in the coils will not be represented but will be assumed in the upper side.

2.7 The coupling Factor

The coupling factor will be derived from the previous expressions for a pair of conductor loops and for a pair of solenoids.

2.7.1.1 Conductor Loops

The mutual inductance between two conductor loops of radius r_1 and r_2 and number of turns N_1 and N_2, respectively, separated a distance d can be approximately calculated from (2.11) as

$$M = \frac{\Phi_2}{I_1}\Big|_{I_2=0} = \frac{\mu_0 \pi N_1 N_2 r_1^2 r_2^2}{2(d^2 + r_1^2)^{\frac{3}{2}}} \tag{2.44}$$

where we have considered $r_1 > r_2$. Obtaining L_1 and L_2 from (2.22), and substituting them jointly with (2.44) in (2.40) we obtain

$$k = \frac{(r_1^2 r_2^2)^{\frac{3}{2}}}{(d^2 + r_1^2)^{\frac{3}{2}}} \tag{2.45}$$

2.7.1.2 Solenoid

Following a similar procedure, the mutual inductance between two solenoids of radius r_1 and r_2, lengths L_1 and L_2, and number of turns N_1 and N_2, respectively, separated a distance d is given by (2.44)

$$M = \frac{\Phi_2}{I_1}\Big|_{I_2=0} = \frac{\mu_0 \pi N_1 N_2 r_1^2 r_2^2}{2(d^2 + r_1^2)^{\frac{3}{2}}} \tag{2.46}$$

where we have considered $r_1 > r_2$ and $d >> l_1, l_2$. Then, the coupling factor can be obtained as

$$k = \frac{(r_1^2 r_2^2)^2}{2(d^2 + r_1^2)^{\frac{3}{2}}} \sqrt{l_1 l_2} \tag{2.47}$$

2.8 Finite Element Modelling

The solution of an analytical expression can be complex or unfeasible to achieve. In this case, an alternative is to use a finite element (FE) method that numerically solves Maxwell's equations for a given geometry and electromagnetic source. The Ampere-Maxwell law showed in (2.8) with the inclusion of an external source current $\overrightarrow{J_e}$, is useful for translating a physical problem into a FE model:

$$\vec{\nabla} \times \vec{B} = \mu\left(\vec{J} + j\omega\epsilon\vec{E} + \vec{J}_e\right) \tag{2.48}$$

Using the magnetic potential $\overrightarrow{A}$ defined as

$$\vec{B} = \vec{\nabla} \times \vec{A} \tag{2.49}$$

the following equation can be obtained from (2.48):

$$\vec{\nabla} \times \left(\mu^{-1}\vec{\nabla} \times \vec{A}\right) + (j\omega\sigma - \omega^2\epsilon) \cdot \vec{A} + (\sigma + j\omega\epsilon)\nabla V = \vec{J}_e \tag{2.50}$$

2.8.1 Axisymmetric Geometries

Coil windings forming circular turns around an axis can be considered, with a certain degree of accuracy, as axisymmetric structures. This category includes solenoids and spiral coils. An axisymmetric model only has two spatial dimensions: radius *r* and height *z*. This implies no variation of the field quantities along the third dimension, φ in cylindrical coordinates. The geometry modeled is a solid of revolution around the z-axis (see Fig. 2.10)

In an axisymmetric coil model, current only flows through the *r-z* plane. $\overrightarrow{J_e}$, $\overrightarrow{E}$ and $\overrightarrow{A}$ are orthogonal to the *r-z* plane and reduce to the scalar variables J_φ, E_φ and A_φ. No potential variation is supported along dimension φ, so the divergence of *V* is zero. Thus (2.50) simplifies to:

$$-\frac{1}{\mu}\nabla^2 A_\varphi + (j\omega\sigma - \omega^2\epsilon)A_\varphi = J_\varphi^e \tag{2.51}$$

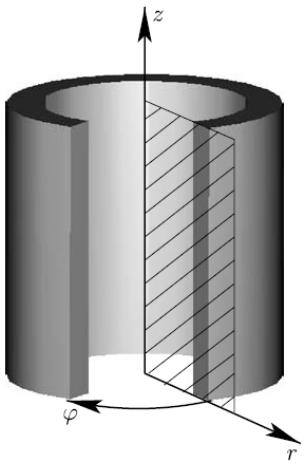

Fig. 2.10 An axisymmetric geometry modeled in the r-z plane [54].

In this work COMSOL MULTIPHYSICS has been used for simulating inductances, mutual inductances, coupling factors, and the effects of metallic objects. In addition, the accomplishment of the regulations according to the ICNRP have been assessed [55].

Although AC signals will really be applied over an inductor, a DC model may be sufficient to calculate the inductance of a coil winding. This approximation implies that current redistribution over the wire cross-section does not noticeably influence the inductance value. This is true for most practical coils, with diameter dimensions normally much larger than the diameter of the wire. In this case, (2.51) becomes:

$$-\frac{1}{\mu}\nabla^2 A_\varphi = J_\varphi^e \tag{2.52}$$

2.8.2 Calculation of the Inductance of a Solenoid

A single rectangle can represent the winding cross-section of a solenoid as can be seen in Fig. 2.11. Actually consisting out of multiple turns, an homogeneous current distribution can be assumed over this cross-section. Hence, a constant current density J_φ is applied over it. Using the vector potential definition and Stokes's theorem [54], the magnetic flux enclosed by the circular contour at (r, z) is:

$$\Phi(r,z) = 2\pi r A_\varphi(r,z) \tag{2.53}$$

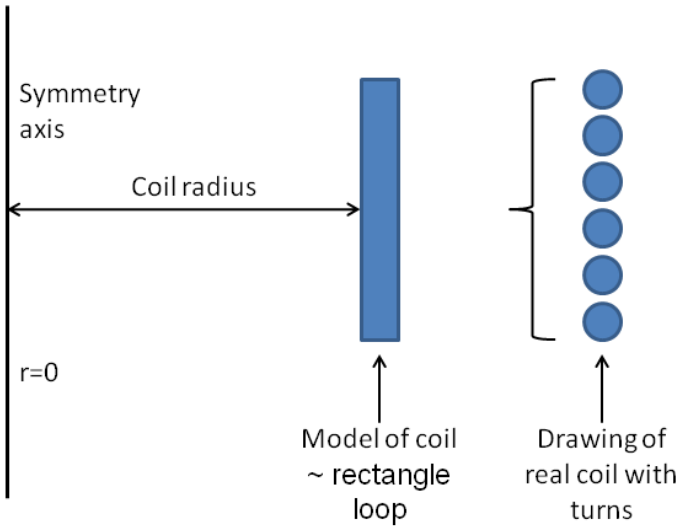

Fig. 2.11 Details of the equivalent coil model in axial symmetry simulating real turns of a coil.

The magnetic potential A_φ is not constant over the winding cross-section and thus the calculated flux Φ depends on the particular contour followed. To resolve this ambiguity, it has to be considered that in reality the winding cross-section consists out of multiple turns. The inhomogeneity of the vector potential A_φ corresponds to a difference in *emf* over the different turns. The average *emf* is obtained by taking the average magnetic flux:

$$\bar{\Phi} = \frac{1}{S}\iint_S 2\pi r A_\varphi dr dz \tag{2.54}$$

where S is the area of the winding cross-section.

Then, we calculate the self-inductance of the solenoid as

$$L = \frac{N^2\bar{\Phi}}{I_\varphi} \tag{2.55}$$

where

$$I_\varphi = \iint_S J_\varphi^e dr dz \tag{2.56}$$

is the average current N is the number of turns. The N^2 factor takes into account the voltages of the N turns and the fact that the current density J_φ^e is N times that of a single turn. From COMSOL, we obtain (2.54) and (2.56).

2.8.3 Calculation of the mutual inductance between two solenoids.

Fig. 2.12 shows the model of two coupled coils separated by a distance (d). The mutual inductance is calculated by applying a current in one of the coils (e.g. coil 1) that generates a magnetic field through the surface of the other coil (e.g. coil 2). Thus, the mutual inductance between coil 1 and 2 of Fig. 2.12 is calculated by

$$M_{12} = \frac{N_1 N_2 \bar{\Phi}_2}{\iint_{S1} J_\varphi^e dr dz} \tag{2.57}$$

where N_1 and N_2 are respectively the number of turns of the coils 1 and 2, $\bar{\Phi}_2$ is the average magnetic flux over the surface of the coil 2 and S_1 is the surface of coil 1. Then, the coupling factor between coil 1 and 2 can be obtained as

$$k = \frac{M_{12}}{L_1} \tag{2.58}$$

Where L_1 is calculated from (2.55).

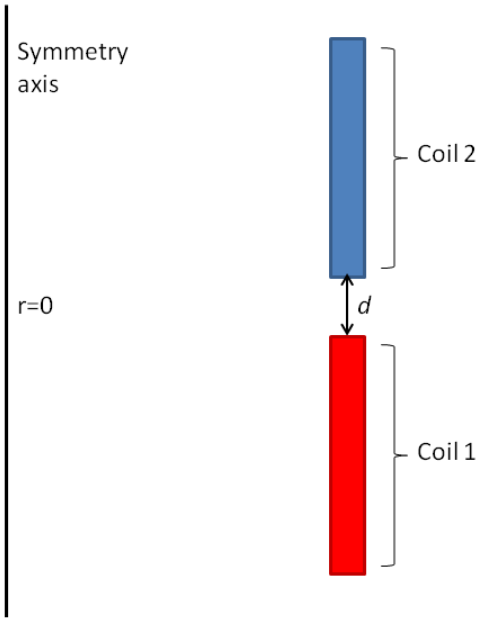

Fig. 2.12 Model of two coupled coils using axial symmetry.

2.9 Exposure Limits and Regulations

Applications with magnetically coupled systems should comply with the ICNIRP guidelines. These regulations have been established to limit human exposure to time-varying

Electromagnetic fields (EMF) with the aim of preventing adverse health effects. The safety norm prescribed by the European Union (EU) legislation, the directive [56], is an exact copy of the ICNIRP 1998 guidelines [55]. ICNRP has issued new guidelines for EMF with frequencies between 1 Hz and 100 kHz in 2010, but these have not yet lead to changes in EU legislation. In a 2009 statement, ICNRP reconfirmed the validity of its guidelines for EMF for frequencies between 100 kHz and 300 GHz. All these norms contain basic restrictions for the current density induced in the body by EMF and reference levels for the strength of EMF outside the body.

The displayed values in Table 2.1 and Table 2.2 are for general public exposure, the most restricted case to apply. Table 2.1 shows the basic restrictions on current density and specific absorption rate (SAR) for frequencies up to 10 GHz. The maximum values for the current density are given up to 10 MHz, whereas the SAR is provided from 100 kHz to 10 GHz. The frequency range between 100 kHz and 10 MHz acts as a transition zone between current density and SAR, so limiting values on both apply. As can be seen, higher frequencies impose a more severe limitation on current density.

Table 2.1 Basic restrictions for general public exposure to time varying electric and magnetic fields for frequencies up to 10 GHz [57].

Frequency range	Magnetic flux density (mT)	Current density (mA/m^2) (rms)	Whole body average SAR (W/kg)	Localised SAR (head and trunk) (W/kg)	Localised SAR (limbs) (W/kg)	Power density, S (W/m^2)
0 Hz	40	—	—	—	—	—
>0-1 Hz	—	8	—	—	—	—
1-4 Hz	—	8/f	—	—	—	—
4-1 000 Hz	—	2	—	—	—	—
1 000 Hz-100 kHz	—	f/500	—	—	—	—
100 kHz-10 MHz	—	f/500	0,08	2	4	—
10 MHz-10 GHz	—	—	0,08	2	4	—
10-300 GHz	—	—	—	—	—	10

As the variables used in Table 2.1 are difficult to measure, the limiting values for the external electric and magnetic fields are obtained from the basic restrictions in Table 2.1. As can be seen, for frequencies higher than 150 kHz, the recommended limit for magnetic field decreases with an increase of frequency. Low magnetic fields allow a lower power transmission in IPT systems. So, in order to allow higher magnetic fields and to simplify the design of the implemented circuits, a maximum working frequency of 150 kHz will be fixed in this work. The direct application of the field values obtained in Table 2.2 may in some cases result in conservative exposure limits compared to that shown in Table 2.1. But in other cases it may

result in a violation of basic restrictions. Hence, the reference levels become only as indicative. The restriction on SAR and current density showed in Table 2.1 are the fundamental ones [54].

Table 2.2 Reference levels for general public exposure to tyme-varying electric and magnetic fields [57].

Frequency range	E-field strength (V/m)	H-field strength (A/m)	B-field (μT)	Equivalent plane wave power density S_{eq} (W/m²)
0-1 Hz	—	$3,2 \times 10^4$	4×10^4	—
1-8 Hz	10 000	$3,2 \times 10^4/f^2$	$4 \times 10^4/f^2$	—
8-25 Hz	10 000	4 000/f	5 000/f	—
0,025-0,8 kHz	250/f	4/f	5/f	—
0,8-3 kHz	250/f	5	6,25	—
3-150 kHz	87	5	6,25	—
0,15-1 MHz	87	0,73/f	0,92/f	—
1-10 MHz	$87/f^{1/2}$	0,73/f	0,92/f	—
10-400 MHz	28	0,073	0,092	2
400-2 000 MHz	$1,375\ f^{1/2}$	$0,0037\ f^{1/2}$	$0,0046\ f^{1/2}$	f/200
2-300 GHz	61	0,16	0,20	10

Chapter 3 Monitoring Switch-Type Sensors via Inductive Coupling

Inductive links can be applied to contactless sense a physical or chemical quantity in harsh or inaccessible environments, where no wiring between the sensor and the processing unit is practicable [16]-[19],[58]-[63]. In these applications, the sensor unit is passive, in the sense that it does not require either a power supply or the use of active electronic components or circuits for signal conditioning. This is advantageous, for example, in high-temperature environments, where the use of such active components would not be appropriate. When the sensor is capacitive, it is disposed together with a coil forming an LC resonant circuit, whose resonant frequency changes according to the sensed parameter [16]-[19], [58]-[60]. In the same way, for inductive sensors, a fixed capacitor is added [61]. Different techniques for the readout of LC circuits were reviewed in [62], where a new technique based on the measurement of the resistance of the readout coil was also proposed. This technique was further developed in [63].

The same contactless sensing principle has also been used to monitor switch-type (or threshold) sensors, i.e. sensors that can be roughly modeled as switches in response to the sensed parameter. So, two states can be assumed for this type of sensors: closed and open. The switch-type sensor is placed in series with a capacitor. Whenever the sensed parameter exceeds a given threshold, the sensor changes its state, thus modifying the equivalent capacitance and resonant frequency. In particular, in [20] and [21], a steel wire was used in order to monitor reinforcement corrosion in structures. The resonant network, which includes the sensor, was embedded within the concrete, near the reinforcement to be monitored. Whenever the reinforcement in the concrete is under corrosion, the steel wire is also corroded and breaks, thus changing the resonant frequency. A readout unit fixed on the surface of the concrete structure detected the change.

In this thesis, we tackle the application of the contactless sensing principle via inductive links on vehicles applications. Switch-type sensors can be found, for example, for seat occupancy and belt detection. In particular, occupancy sensors are embedded within the seats and wired to an (ECU) of the vehicle. However, wiring removable vehicle seats, which are present in some vehicle models, to the ECU is unpractical. To solve this problem, inductive links have been proposed in a patent [22] for detecting the state of switch-type sensors in removable vehicle seats and are currently used in some vehicle models for belt detectors attached to the removable seats.

In the remaining of this chapter, different readout techniques are analyzed. Twofold contributions are provided: First, we present a theoretical analysis for the monitoring of generic switch-type sensors via inductive coupling. The analytical expressions consider an arbitrary

number of switch-type sensors placed at the resonant network and a non-zero resistance of the sensors when they are in their closed state. Secondly, we investigate the use of inductive links for occupancy and belt detection in removable vehicle seats. Experimental results agree with the provided analytical expressions.

3.1 Wireless readout of Passive LC Sensors

3.1.1 Basic Architecture

Fig. 3.1 illustrates a general circuit model of an *LC* resonant network (right-hand side) coupled to a readout circuit (left-hand side). L_1 and L_2 are the coupled coils, M is the mutual inductance, R_1 models the losses of L_1 plus the connecting wires, and C_T and R_T model respectively the equivalent series capacitance and resistance of the resonant network. This is a simplification and a start point of the analysis that pretends to facilitate the analysis in the rest of the section.

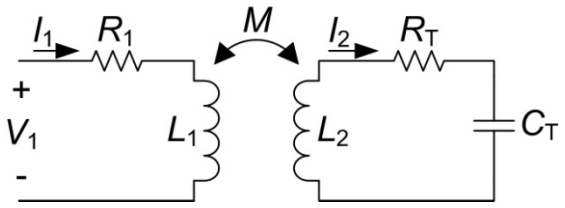

Fig. 3.1 Circuit model of an LC resonant network (right-hand side) coupled to a readout circuit (left-hand side).

The impedance seen from the readout coil is given, using complex notation, by [62]

$$Z_{\text{in}} = \frac{V_1}{I_1} = R_1 + j\omega L_1 \left(1 + \frac{k^2 \left(\frac{\omega}{\omega_r}\right)^2}{1 + j\frac{1}{Q_T}\frac{\omega}{\omega_r} - \left(\frac{\omega}{\omega_r}\right)^2} \right) \tag{3.1}$$

where k

$$k = \frac{M}{\sqrt{L_1 L_2}} \tag{3.2}$$

is the coupling factor between the coils,

$$\omega_r = \frac{1}{\sqrt{L_2 C_T}} \tag{3.3}$$

is the resonant frequency, and

$$Q_{\mathrm{T}} = \frac{1}{R_T}\sqrt{\frac{L_2}{C_{\mathrm{T}}}} \tag{3.4}$$

is the quality factor of the LC resonant network. From (3.1), the real part of Z_{in} is given by

$$\mathrm{Re}\{Z_{\mathrm{in}}\} = R_1 + \omega L_1 k^2 Q_{\mathrm{T}} \left(\frac{\frac{\omega}{\omega_{\mathrm{r}}}}{1 + {Q_{\mathrm{T}}}^2 \left(\frac{\omega}{\omega_{\mathrm{r}}} - \frac{\omega_{\mathrm{r}}}{\omega} \right)^2} \right) \tag{3.5}$$

and the imaginary part of Z_1 is given by

$$\mathrm{Im}\{Z_{\mathrm{in}}\} = \omega L_1 \left(1 + k^2 Q_{\mathrm{T}}^2 \frac{1 - \left(\frac{\omega}{\omega_{\mathrm{r}}} \right)^2}{1 + {Q_{\mathrm{T}}}^2 \left(\frac{\omega}{\omega_{\mathrm{r}}} - \frac{\omega_{\mathrm{r}}}{\omega} \right)^2} \right) \tag{3.6}$$

From (3.5) and (3.6), we obtain the modulus $|Z_{\mathrm{in}}|$ and phase $<Z_{\mathrm{in}}$ of the input impedance

$$|Z_{\mathrm{in}}| = \sqrt{\mathrm{Re}^2\{Z_1\} + \mathrm{Im}^2\{Z_1\}} \tag{3.7}$$

$$< Z_{\mathrm{in}} = \arctan \frac{\mathrm{Im}\{Z_1\}}{\mathrm{Re}\{Z_1\}} \tag{3.8}$$

3.1.2 Readout Techniques

Different readout circuit systems are analyzed, for example, in [17] and [62]. Most of them are based on the change detection of one or several resonant frequencies of a parameter related with the input impedance of the readout coil. That change is caused by a variation of the sensed quantity. As the measured resonant frequency or frequencies at the readout coil are related to ω_r, the sensed quantity can be estimated. In this section, we review different readout techniques proposed in the literature and select one of them to be applied in the proposed application of this thesis.

Impedance phase dip or phase-min method has been proposed in several publications [16], [18], [58] and [60]. It is based on the measurement of the phase impedance of the readout coil and the subsequent detection of the minimum value. From (3.8), assuming $Q_{\mathrm{T}} >> 1$ and neglecting R_1, a minimum phase impedance is found at

$$\omega_{\varphi,min} = \sqrt{\frac{k^2 - 2 + \sqrt{k^4 - 16k^2 + 16}}{2 - 2k^2}}\,\omega_r \tag{3.9}$$

which for low values of k can be simplified to

$$\omega_{\varphi,min} \approx \left(1 + \frac{1}{4}k^2\right)\omega_r \tag{3.10}$$

As can be seen, a weak point of this method is its dependency with the coupling factor k, and thus with the distance between the coils. Further, for increasing values of k, the phase dip becomes broader (see Fig. 3.2 as an example), which difficults the accurate detection of the phase minimum. At fixed distances, a single calibration can be performed. Whenever the distance between the coils has to change, a calibration at different distances should be performed.

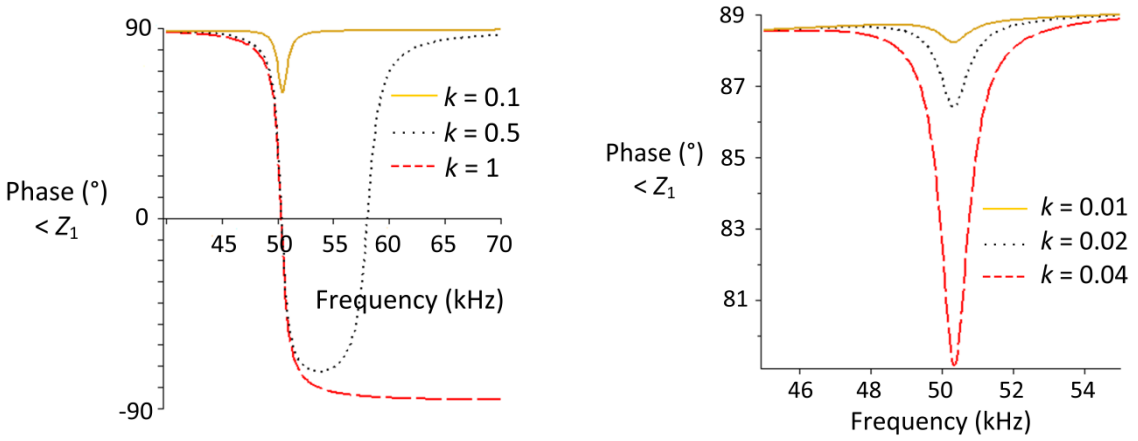

Fig. 3.2 Calculated impedance phase using (3.9) at different values of k with L_2=L_1=1mH, C_T=10nF, R_1=R_T=6Ω.

Another technique is that known as dip meter [61], [62], [64]. As mentioned in [62], a dip meter is an LC oscillator whose inductance is the readout coil. The frequency of the oscillator is swept over a band, and when the frequency matches that of the resonant circuit to be measured a dip in the primary coil current is observed. This is due to the increase of the reflected impedance into the readout coil. However, as reported in [62], for values of k higher than a critical value, the reflected impedance decreases which leads again to a dependency with the distance.

Other techniques measure the impedance modulus. In [17] a circuit based on a peak detector is used. The system monitors the resulting resonant frequency automatically. However, as can be seen in Fig. 3.3 for a particular case and as mentioned in [18], several resonant frequencies can appear and all them show a dependency with the distance between the coils.

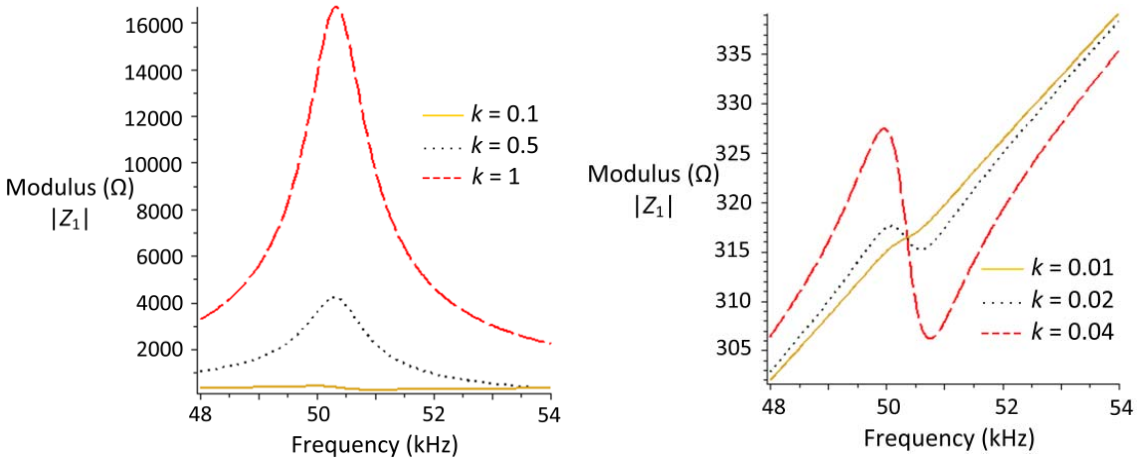

Fig. 3.3 Calculated modulus of the impedance using (3.7) for L_1=L_2=1mH, C_T=10nF and R_1=R_T=6Ω.

In order to get rid of the distance effect, the three-resonances method was proposed in [18], which is based on the measurement of the modulus of the readout impedance. This is a decisive advantage in applications where the distance or the alignment of the reader coil relative to the sensor is variable. However, the method requires the estimation of three resonant frequencies and some computations, which raises the complexity.

In [62] a novel technique, based on the measurement of $\mathrm{Re}\{Z_{in}\}$ was proposed, which was further developed in [63]. The real part of the impedance in (3.5) can be defined as

$$R_{\mathrm{in}} = \mathrm{Re}\{Z_{\mathrm{in}}\} \tag{3.11}$$

which resembles the response of a band-pass filter and presents a maximum at

$$\omega_{\mathrm{max}} = \omega_{\mathrm{r}} \frac{1}{\sqrt{1 - \frac{1}{2Q_{\mathrm{T}}^2}}} \tag{3.12}$$

The frequency selectivity of R_{in} around ω_{max} improves with an increase of Q_T [62]. Whenever $Q_T >> 1$, thus $\omega_{max} \approx \omega_r$ and

$$R_{\mathrm{in,max}} \equiv R_{\mathrm{in}}|_{\omega=\omega_{\mathrm{r}}} = R_1 + \omega_{\mathrm{r}} L_1 k^2 Q_{\mathrm{T}} \tag{3.13}$$

which can be rearranged as

$$R_{\mathrm{in,max}} = R_1(1 + k^2 Q_{\mathrm{R}} Q_{\mathrm{T}}) \tag{3.14}$$

where

$$Q_{\mathrm{R}} = \frac{\omega L_1}{R_1} \tag{3.15}$$

is the quality factor of the readout circuit. Whenever R_1 is mainly due to the coil losses, Q_{R} will match the coil quality factor. From (3.14), $k^2 Q_{\mathrm{R}} Q_{\mathrm{T}} \gg 1$ has to be accomplished in order to have a relative high value of $R_{\mathrm{in,max}}$. Therefore, by searching $R_{\mathrm{in,max}}$ we can obtain ω_{r}. Then, from (3.3) and known L_2, the value of C_{T} can be inferred.

For this thesis work, we propose the use of the measurement of R_{in}. Next sections present, first, an extension of the selected readout technique for N switch-type sensors and then, its application to occupancy and belt detection in removable vehicle seats.

3.2 Equivalent Circuit for N switch-type sensors

Fig. 3.4 illustrates a circuit model of a resonant network coupled to a readout circuit, which includes an arbitrary number (N) of switch-type sensors. Each sensor S_i, with i = [1..N], is modeled as a switch. A capacitor C_{i} is added in series with each sensor S_i. R_{L2} models the inductor losses and a capacitor C_0 is added in parallel with the sensor branches. This capacitor makes the circuit resonate even in the case all the switch-type sensors are open. As we will just show, the circuit of Fig. 3.4 will be reduced to the circuit of Fig. 3.1, being C_{T} and R_{T} dependent on the state of the switch-type sensors.

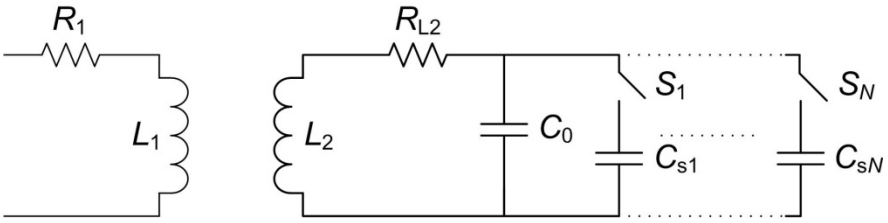

Fig. 3.4 Circuit model of the resonant network with *N* switch-type sensors.

For each sensor we assume two states: closed and open. In the closed state we will model the sensor as a resistance R_{si} (in general of low value) and in the open state as an open circuit. As a result, Fig. 3.5 shows the resulting equivalent circuit of the resonant network in the case all the sensors are closed. In a general case, only the sensor branches which contain closed sensors must be included.

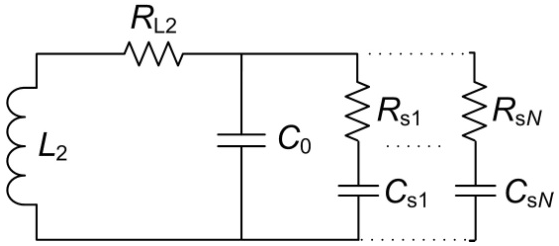

Fig. 3.5 Circuit model of the resonant network in the case all the sensors are closed.

The quality factor of each branch that contains a closed sensor will be

$$Q_{si} = \frac{1}{\omega_r C_{si} R_{si}} \tag{3.16}$$

Using a series to parallel transformation at the resonant frequency (ω_r) for each closed-sensor branch, the circuit of Fig. 3.5 results in the circuit of Fig. 3.6,

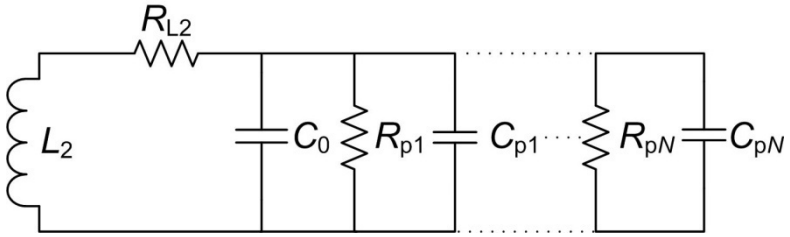

Fig. 3.6 Circuit model of the resonant network for $\omega=\omega_r$ using a series to parallel transformation for the closed-sensor branches.

where

$$C_{pi} \approx C_{si} \tag{3.17}$$

$$R_{pi} \approx R_{si} Q_{si}^2 \tag{3.18}$$

and we have assumed that $Q_{si}^2 \gg 1$. By substituting (3.16) in (3.18) we obtain

$$R_{pi} \approx \frac{1}{\omega_r^2 C_{si}^2 R_{si}} \tag{3.19}$$

The circuit of Fig. 3.6 can be further simplified to the circuit of Fig. 3.7, where

$$C_p = C_0 + \sum_i b_i C_{pi} \tag{3.20}$$

$$\frac{1}{R_p} = \sum_i \frac{b_i}{R_{pi}} \tag{3.21}$$

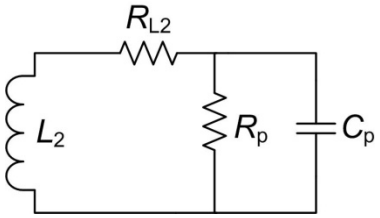

Fig. 3.7 Simplified circuit model of the circuit of Fig. 3.6.

In (3.20) and (3.21), the binary variable b_i accounts for the contribution of each sensor S_i to C_p and R_p. Whenever the sensor S_i is open, b_i takes the value 0, thus denoting a null contribution. Otherwise, whenever the sensor S_i is closed, $b_i = 1$. By substituting (3.17) in (3.20) and (3.19) in (3.21) we respectively obtain

$$C_p \approx C_0 + \sum_i b_i C_{si} \tag{3.22}$$

and

$$\frac{1}{R_p} \approx \omega_r^2 \sum_i b_i C_{si}^2 R_{si} \tag{3.23}$$

The quality factor of the C_p-R_p branch in Fig. 3.7 is given by

$$Q_p = \omega_r C_p R_p \tag{3.24}$$

Using a parallel to series transformation we arrive to the circuit of Fig. 3.8

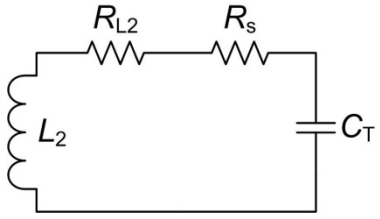

Fig. 3.8 Transformation of the circuit of Fig. 3.7 using a parallel to series conversion.

where

$$C_T \approx C_p \tag{3.25}$$

$$R_s \approx \frac{R_p}{Q_p^2} \tag{3.26}$$

and we have assumed that $Q_p^2 \gg 1$. Substituting (3.24) and (3.25) in (3.26) yields

$$R_{\mathrm{s}} \approx \frac{\sum_i b_i C_{si}^2 R_{si}}{C_{\mathrm{T}}^2} \tag{3.27}$$

Finally, just adding up the two serial resistances we obtain the resonant network of Fig. 3.1, where

$$R_{\mathrm{T}} = R_{\mathrm{L2}} + R_{\mathrm{s}} \tag{3.28}$$

Attending to the binary response of the sensors, 2^N different values of C_{T} and thus of ω_{r} result. Thus, capacitors have to be chosen appropriately in order to distinguish the resulting resonant frequencies and infer the state of the sensors. As mentioned in section 3.1, a higher value of Q_{T} leads, from (3.5) to a frequency response of R_{in} with a higher selectivity, thus facilitating an accurate detection of the different resonant frequencies. By substituting (3.27) in (3.28) and the resulting expression in (3.4) we get

$$\frac{1}{Q_{\mathrm{T}}} \approx \left(R_{\mathrm{L2}} + \frac{\sum_i b_i C_{si}^2 R_{si}}{C_{\mathrm{T}}^2} \right) \sqrt{\frac{C_{\mathrm{T}}}{L_2}} \tag{3.29}$$

Then, by defining

$$Q_{\mathrm{L2}} = \frac{1}{R_{\mathrm{L2}}} \sqrt{\frac{L_2}{C_{\mathrm{T}}}} \tag{3.30}$$

as the quality factor of the secondary coil and

$$Q_{\mathrm{T}i} = \frac{1}{R_{si}} \left(\frac{C_{\mathrm{T}}}{C_{si}} \right)^2 \sqrt{\frac{L_2}{C_{\mathrm{T}}}} \tag{3.31}$$

as the equivalent quality factor of each closed-sensor branch, all at the resonant frequency ω_{r}, and substituting them in (3.29), we arrive to

$$\frac{1}{Q_{\mathrm{T}}} \approx \frac{1}{Q_{\mathrm{L2}}} + \sum_i \frac{b_i}{Q_{\mathrm{T}i}} \tag{3.32}$$

Therefore, in order to achieve a high value of Q_{T}, we require high quality factors for the coil and for the sensor branches. From (3.31), sensors that present relatively high values of resistance (R_{si}) when closed will be prone to present low quality factors. Nonetheless, we can moderately raise them by using the capacitors (C_{si}) with the lowest values, among those selected, with those sensors.

For the sake of simplicity, in the previous analysis we have considered ideal open circuits for sensors in the open state. Actually, open-switch sensors will present parasitic capacitances that will add up to C_T. Whenever the value of the selected capacitors is much higher than that of the parasitic capacitances, the net effect on the resonant frequency will be negligible. The same can be said for the parasitic capacitance of the coil L_2.

3.3 Circuit Model with the Seat Detectors

Fig. 1.1, shows the occupancy and belt detectors. The commercial occupancy sensor presents a large electrical resistance variation from a vacant to occupied seat. For diagnostic purposes, the manufacturer includes a resistor (470 Ω) in parallel with the sensor in order to differentiate the response of a vacant seat (high resistance) from a fault, for example when any of the wires that connect the sensor with the ECU is broken. In this work, this parallel resistor was removed. We then characterized the occupancy sensor for low frequencies (< 1 MHz). When the seat is occupied the sensor can be modeled as a resistor of value *ca*. 15 Ω. On the other hand, when the seat is vacant the sensor can be modeled as a capacitor of value *ca*. 160 pF. Occupancy is detected for weights higher than 40 kg.

We also characterized the belt detector for frequencies below 1 MHz. When the belt is unbuckled, the detector can be modeled as a resistor of value 0.1 Ω. On the other hand, when the belt is buckled up, the detector can be modeled as a capacitor of *ca*. 47 pF.

Fig. 3.9 shows the resulting circuit model with the seat detectors, where S_1 and S_2 correspond respectively to the occupancy sensor and belt buckle switch.

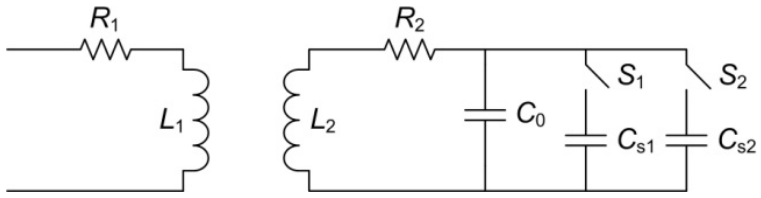

Fig. 3.9 Circuit model of an inductive link with a seat occupancy sensor and a belt buckle switch.

Attending to the possible states of both sensors, four different cases result:

Case 1) vacant seat, buckled up:

$$C_T = C_0, \qquad R_T = R_{L2}$$

Case 2) occupied seat, buckled up:

$$C_T = C_0 + C_{s1}, \qquad R_T = R_{L2} + R_{s1}\left(\frac{C_{s1}}{C_T}\right)^2$$

Case 3) vacant seat, unbuckled:

$$C_{\mathrm{T}} = C_0 + C_{\mathrm{s2}}, \qquad R_{\mathrm{T}} = R_{\mathrm{L2}} + R_{\mathrm{s2}}\left(\frac{C_{\mathrm{s2}}}{C_{\mathrm{T}}}\right)^2$$

Case 4) occupied seat, unbuckled:

$$C_{\mathrm{T}} = C_0 + C_{\mathrm{s1}} + C_{\mathrm{s2}}, \qquad R_{\mathrm{T}} = R_{\mathrm{L2}} + R_{\mathrm{s1}}\left(\frac{C_{\mathrm{s1}}}{C_{\mathrm{T}}}\right)^2 + R_{\mathrm{s2}}\left(\frac{C_{\mathrm{s2}}}{C_{\mathrm{T}}}\right)^2$$

The SBR system must warn in case 4.

3.4 Coils

A rather low frequency of operation (i.e. < 1 MHz) was sought for two reasons: 1) to ease an upcoming design of the electronic circuitry for the measurement of the real part of the impedance, and 2) to avoid inductive effects of the occupancy sensor. In addition, the intended application is space-constrained, which requires the use of small-size coils.

As we have previously mentioned, a high value of Q_{T} improves the frequency selectivity around the resonant frequency, which facilitates its location. Further, from (3.13), relative high values of k and Q_{R} are helpful to increase $R_{\mathrm{in,max}}$. As we will discuss in section 3.5, this also contributes to determine accurately the resonant frequency. As a result, coils with magnetic- instead air-core are appropriate as they provide high quality and coupling factors at rather low frequencies and for small-size dimensions.

We selected 1 mH commercial coils from Fastron (PIST model) which present a dc resistance of 1.5 Ω. Fig. 3.10 shows the dimensions of the coils (values are in millimeters). Below we provide information about relevant parameters such as the coil quality factor over frequency, and the coupling factor between coils.

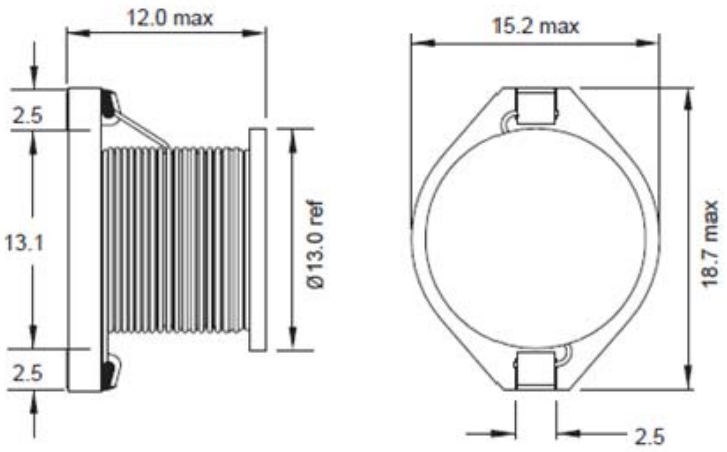

Fig. 3.10 Dimensions of the selected 1 mH coils (in millimeters). Source: http://www.fastrongroup.com/.

The quality factor of one of the commercial coils was measured for a range of frequencies, which required the measurement of both the coil resistance and inductance. We used a series-resonant network to measure the resistance at the resulting resonant frequency by using an HP4294A impedance analyzer. Appropriate values of capacitors were used in order to tune different resonant frequencies. On the other hand, the inductance value was measured with a handheld LCR meter at a single frequency as its value did not appreciably change. The resulting value was of 1.096 mH. Then, the coil quality factors were calculated. Fig. 3.11 shows the results for a frequency range between 3 kHz and 700 kHz. Fig. 3.12 provides additional results for a narrower frequency range, from 15 kHz to 50 kHz. As can be seen, the quality factor increased at low frequencies up to a maximum (*ca*. 45) at *ca*. 35 kHz and then decreased for higher values of frequency. The decrease at the higher frequencies is due to the higher rate of increase of the equivalent coil resistance with respect to the coil inductance. Coil resistance increase is due to the joint combination of skin and proximity effects and the losses of the ferrite. So, in order to achieve a high quality factor, a resonant frequency in the order of tens of kilohertz seems appropriate.

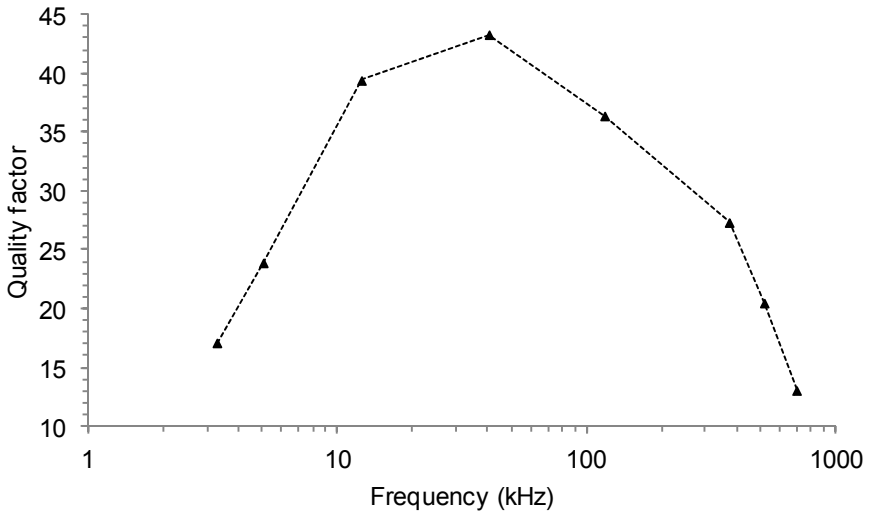

Fig. 3.11 Measured quality factors of a 1mH Fastron coil for a frequency range from 3 kHz to 700 kHz.

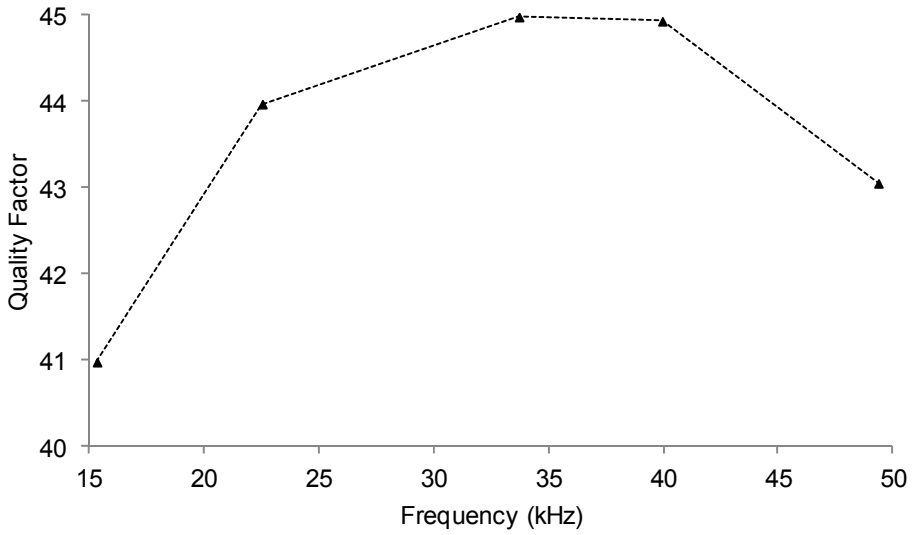

Fig. 3.12 Measured quality factors of a 1mH Fastron coil for a frequency range from 15 kHz to 50 kHz.

In order to estimate the coupling factor (k) between the coils over their separation distance (d), we used the simulation program COMSOL. Fig. 3.13 shows an axisymetric model of the coils, where d is marked. Sizes of the coils were in accordance with those presented in Fig. 3.10. The contour areas R1 to R6 were defined as ferrite whereas C1 and C2 (wire coil) were defined as copper. A relative permeability (μ_r) of 2000 was used for the ferrite.

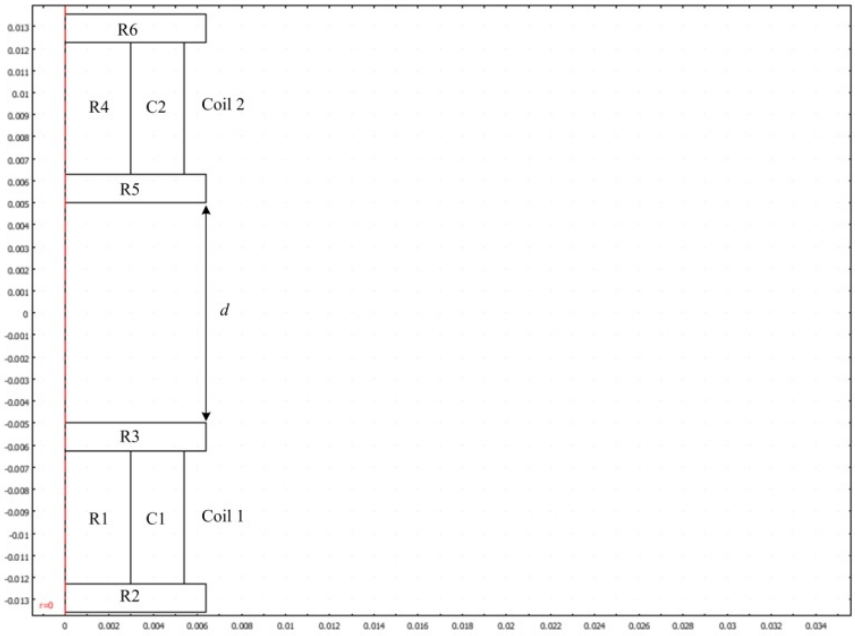

Fig. 3.13 Modeling of the primary and secondary coils using COMSOL.

The self and mutual inductance of the coils (L and M respectively) were calculated and k was obtained from (2.58). Fig. 3.14 shows graphically the evolution of k for different distances, from 0 cm to 3 cm in steps of 0.5 cm. The graph also includes the case of an equivalent air-core coil (ferrite core was substituted by air in the simulation). The value of k was about 3 to 4 times larger for ferrite- than for air-core coils. The inductance value was also larger for the ferrite-core coil, about ten times, which leads to a higher quality factor whenever the core losses are not significant. These results confirm the suitability of using ferrite- instead air-core coils in order to increase the value of $R_{\text{in,max}}$, see (3.13).

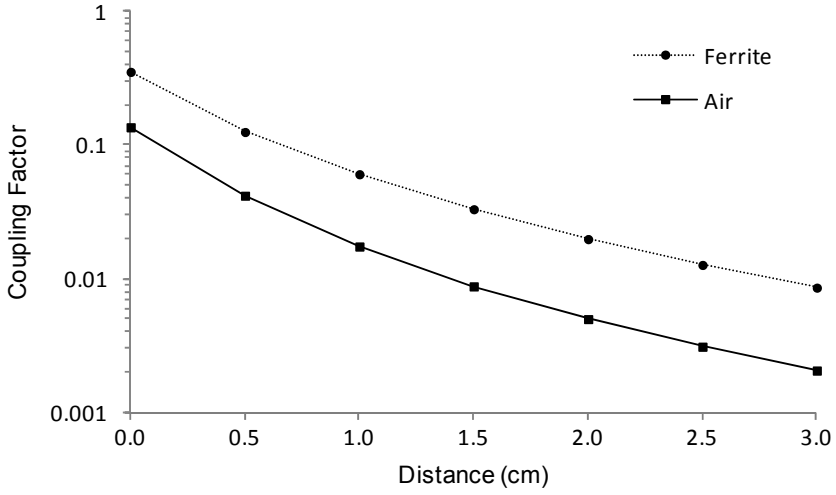

Fig. 3.14 Evolution of *k* over *d* for ferrite- and air-core coils.

A side effect of using magnetic-core coils is the increase of the self-inductance of the coils due to the presence of the ferrite of the other coil. This effect was corroborated experimentally,

as shown in Fig. 3.15, when approaching a second open-circuit coil. As a result, the resonant frequency will slightly decrease at low values of *d*.

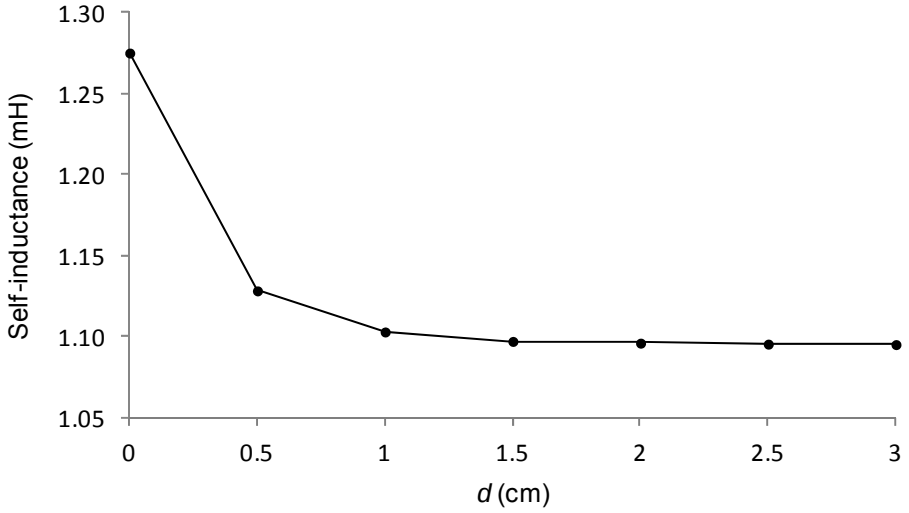

Fig. 3.15 Measured self-inductance of the commerical coil when approaching a second open-circuit coil to a distance *d*.

3.5 Performance

Fig. 3.16 shows the mechanical setup fabricated to fix the distance between the coils, which were implemented in separate PCB boards. Distance was adjusted manually. The support and the fixing screws were made of nylon. The picture also shows the occupancy sensor and the belt buckle switch as well as a vehicle seat where the occupancy sensor is inserted. The setup emulates the configuration shown in Fig. 1.2. In reference to Fig. 3.9, we used the 1 mH commercial coils, $C_2 = C_{s1} = 10$ nF and $C_{s2} = 22$ nF. Thus, the resonant frequencies will lie between 20 kHz and 50 kHz, which, from Fig. 3.11 and Fig. 3.12, is appropriate in order to achieve high quality factors for the coils. The lowest capacitor value between C_{s1} and C_{s2}, i.e. C_{s1}, was used for the occupancy sensor as it presented a higher resistance ($R_{s1} \approx 15\ \Omega$) than that of the belt buckle switch ($R_{s2} \approx 0.1\ \Omega$).

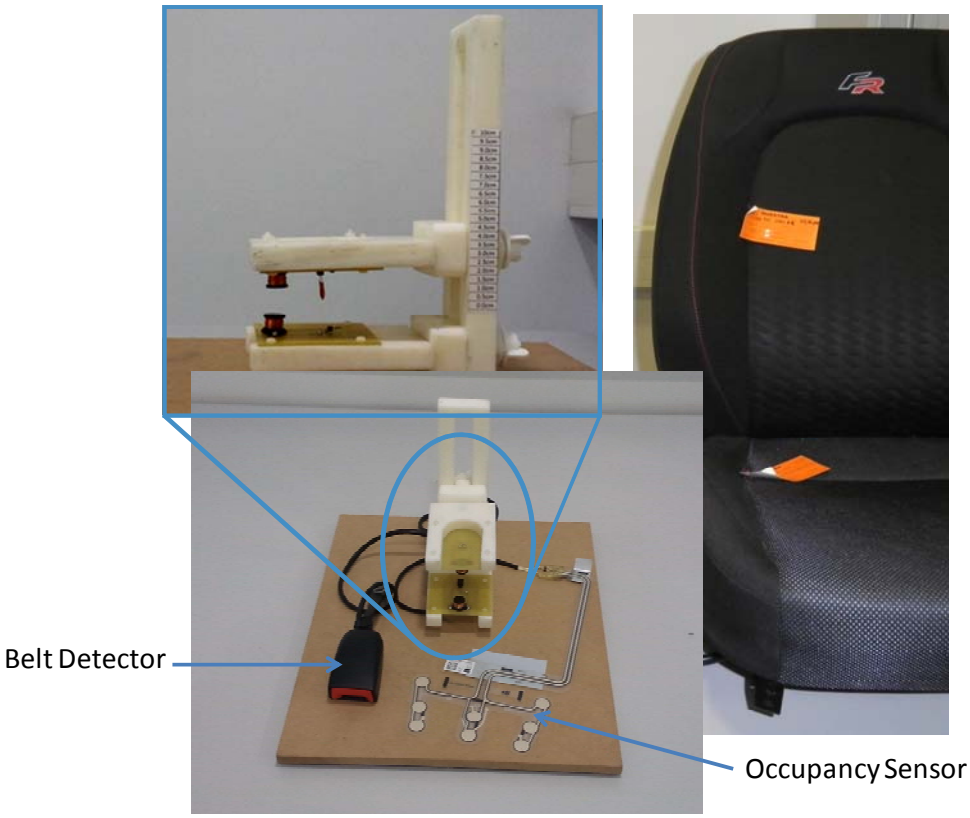

Fig. 3.16 Mechanical setup used to fix the distance of the coils. The occupancy sensor and the belt buckle switch are also shown as well as a vehicle seat where the occupancy sensor is inserted.

The readout coil was connected to an impedance analyzer (HP4294A) in order to measure the real and imaginary parts of the impedance, i.e. Z_{in} in (3.1). The programmed frequency range was from 20 kHz to 50 kHz. The represented data in the remaining figures, Fig. 3.17 to Fig. 3.20, show the captured values of the real part of the impedance, i.e. (3.11). Unless specified, the data for each of the cases correspond to a single capture, without averaging, and using the least accurate measurement bandwidth (BW = 1).

Fig. 3.17 shows the captured values of R_{in} for each of the four cases of the seat detectors at d = 0.5 cm. The four data captures corresponding to the four possible cases are superposed. As can be seen, the respective resonant frequencies can be clearly distinguished, which allows to determine unambiguously the state of both seat detectors. Cases 1 to 4 evolve respectively from the higher to the lower resonant frequency.

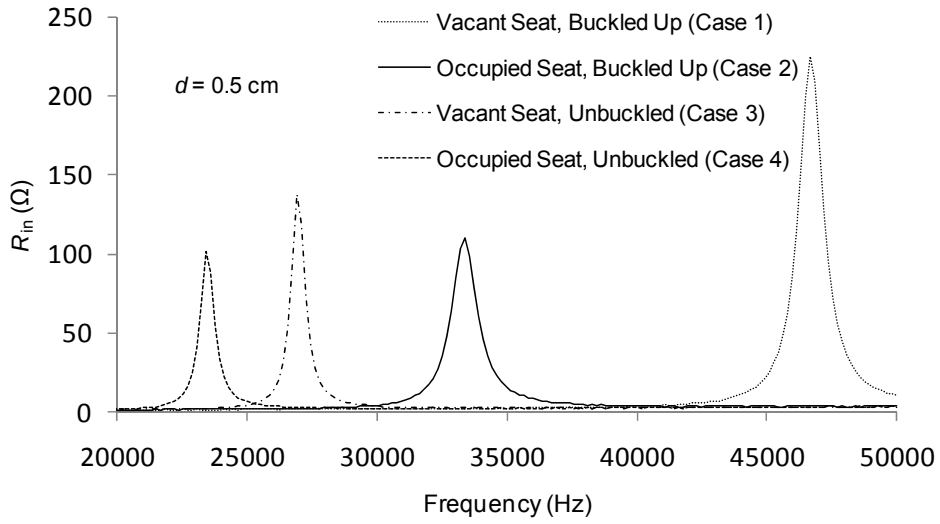

Fig. 3.17 R_{in} for the four different cases of the seat detectors at d=0.5 cm.

In order to further validate the theoretical analysis of section 3.1, we estimated the value of Q_T in two ways. First, following the approach described in [62], the value of Q_T was estimated graphically from Fig. 3.17 for each of the cases as

$$Q_T = \frac{\omega_r}{\Delta\omega_{HM}} \tag{3.33}$$

where $\Delta\omega_{HM}$ is the difference of frequencies for which R_{in} is equal to $(R_{in,max} - R_1)/2$. Then, Q_T was calculated from (3.32), where the values of Q_{L2} were inferred from Fig. 3.12 and the values of Q_{Ti} were calculated using (3.31). For the calculus of (3.31), we used the experimental values of R_{si} and the nominal values for the rest of the parameters. Table 3.1 shows the resulting values, where $Q_{T,graph}$ and $Q_{T,calc}$ correspond respectively to the estimated values from (3.33) and (3.32). In addition, the values of Q_{L2}, Q_{T1}, and Q_{T2} are provided. As can be seen, $Q_{T,graph}$ and $Q_{T,calc}$ are in good agreement. So, for the sake of simplicity, we will use hereafter the term Q_T.

Table 3.1 Estimated values of Q_T

	$Q_{T,\,graph}$	$Q_{T,\,calc}$	Q_{L2}	Q_{T1}	Q_{T2}
Case 1	46.6	44.7	44.7	—	—
Case 2	28.9	26.6	44.9	59.6	—
Case 3	42.9	43.8	44.3	—	3740
Case 4	36.1	35.2	44.0	181	5624

As for the particular cases, the value of Q_T in case 1 is solely contributed by Q_{L2} as both detectors are in the open state. Case 2 presents a much more reduced Q_T due to the contribution

of Q_{T1}, which models the effect of the occupancy sensor in the closed state. Case 3 again shows a higher quality factor, as the contribution of Q_{T2}, due to the closure of the buckle switch, is negligible. Finally case 4, sees again a reduction of Q_T mainly due to Q_{T1}. However Q_{T1} is now higher than in case 2 due to the increased value of C_T, see (3.31). Thus, the resulting Q_T is higher in case 4 than in case 2. As can also be observed, Q_{T1} and Q_{T2} and thus their square values are much higher than the unity in all the cases, which is an assumption that was taken in section 3.1. The value of $R_{in,max}$ across the different resonant frequencies also behaves as previewed by (3.13). A higher ω_r leads to a higher $R_{in,max}$. For case 2, the lower value of $R_{in,max}$ with respect to case 3 is due to the lower value of Q_T. As a final remark, interchanging capacitors C_{s1} and C_{s2} would be detrimental for Q_T in cases 2 and 4, as the value of Q_{T1} would decrease to 24.9 and 37.5, respectively. On the other hand, the increase in Q_{T2} for cases 3 and 4 would be barely noticeable in Q_T.

Fig. 3.18 shows the measured values of R_{in} for case 4 (occupied seat and unbuckled belt) at four different values of d (0.5 cm, 1 cm, 1.5 cm, and 2 cm). The SBR system must warn the driver in this case. As can be seen, $R_{in,max}$ decreases for increasing distances. From Fig. 3.14, an increase of distance leads to a decrease of k and thus, from (3.14), to a decrease of $R_{in,max}$. Inferred values of k (not shown here) from (3.14), using the experimental values of Fig. 3.18 for $R_{in,max}$, were in good agreement with the simulated results presented in Fig. 3.14 for the ferrite-core coil. On the other hand, the resonant frequency slightly decreased for shorter distances. This effect, as previously stated, was due to the increase of the self-inductance of the coils at short distances (see Fig. 3.15).

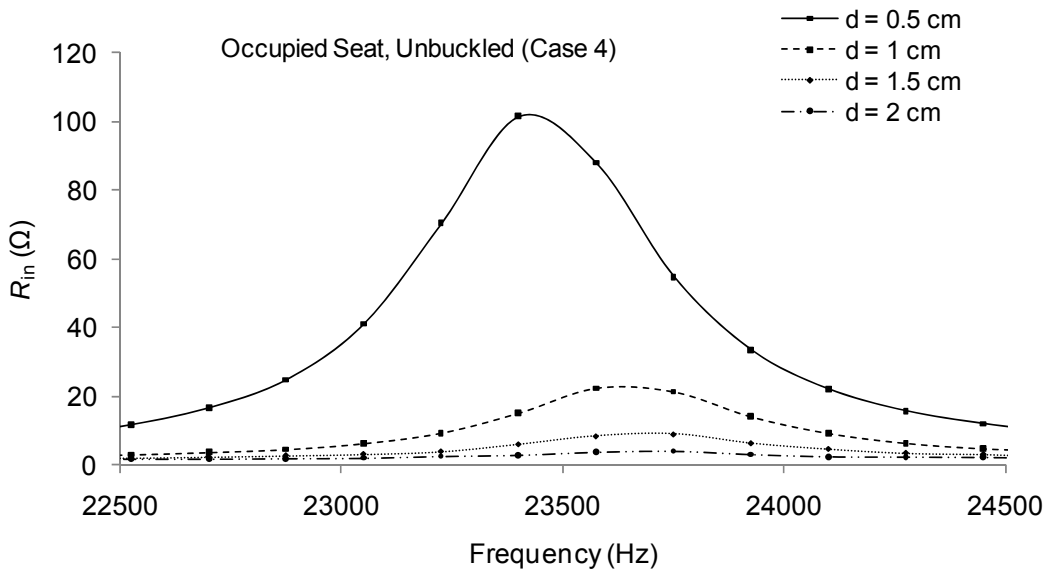

Fig. 3.18 R_{in} for case 4 at different distances between the coils. The SBR system must warn the driver in this case.

Fig. 3.19 shows the captured values of R_{in} for d = 3cm and the four cases. Again, captured data are superposed. Now, the measurement bandwidth of the impedance analyzer was selected for maximum accuracy (BW = 5). The increased accuracy comes at the cost of a larger measuring time of the impedance analyzer. As can be seen, the base value of R_{in}, R_1 in (3.5), increases with an increasing frequency. This increase of the coil resistance for increasing frequencies was already justified in section 3.4. Still, the respective resonant frequencies can be clearly distinguished. However, for larger distances, i.e. lower values of $R_{in,max}$, the increase of R_1 with increasing frequencies, can mask the resistance peak and, thus, the location of the resonant frequency. So, to achieve large distances at which the resonant frequencies can still be detected, large relative values of $R_{in,max}$ are helpful. Thus, from (3.14), as mentioned at the beginning of section 3.4, high values of Q_R, Q_T, and k are sought. This design criterion was followed in this work.

Fig. 3.20 shows again the captured values of R_{in} for d = 3 cm but using the least accurate measurement bandwidth (BW = 1) of the impedance analyzer. As in the previous cases, only one single data capture is shown but in this case the variability of the data is significant. So, the uncertainty of the measuring instrument has a large impact at larger distances, i.e. for low relative values of $R_{in,max}$. Thus, the instrument uncertainty can also limit the accurate location of the resonant frequency and thus limit the maximum detection distance, as will be shown below.

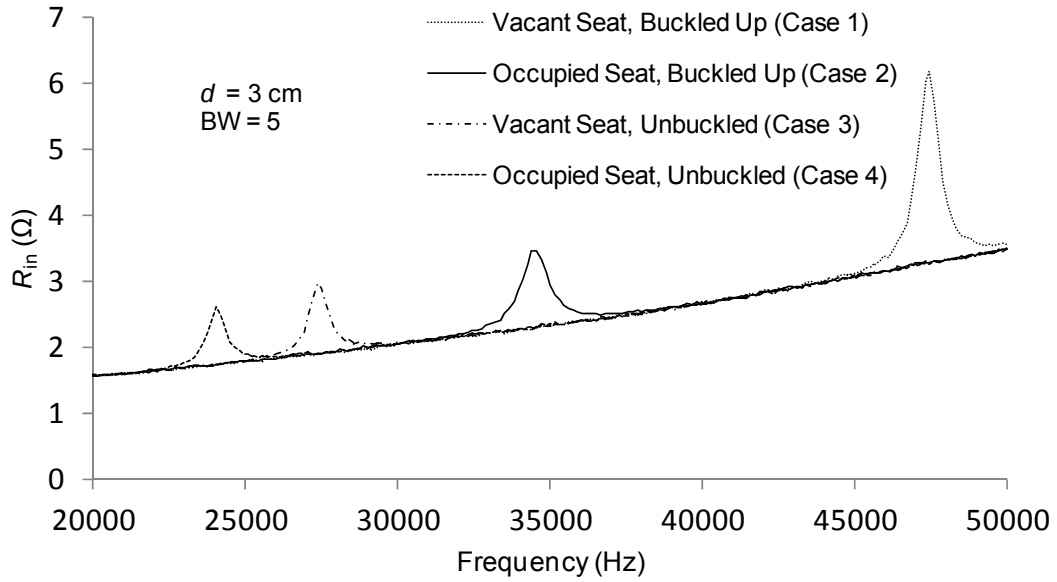

Fig. 3.19 R_{in} for the four different cases of the seat detectors at d=3 cm with BW=5.

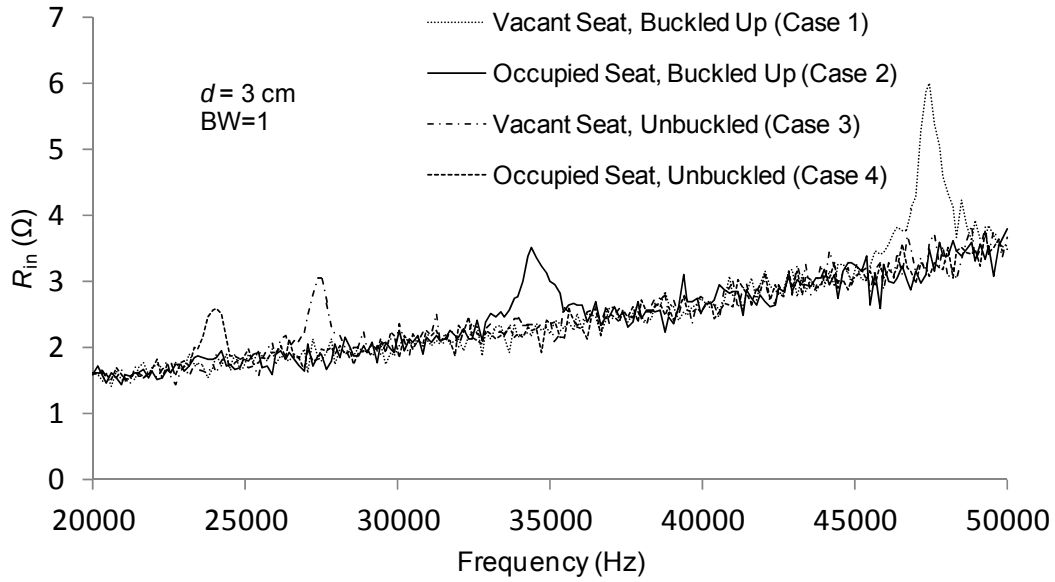

Fig. 3.20 R_{in} for the four different cases of the seat detectors at d=3 cm with BW=1.

The uncertainty on the measurement of R_{in} can be expressed as

$$\Delta R_{\text{in}} = \Delta R_{\text{in}}(\%) \cdot R_{\text{in}} \tag{3.34}$$

where $\Delta R_{in}(\%)$ is the uncertainty[1] in percentage provided by the manufacturer of the impedance analyzer [65] as

$$\Delta R_{\text{in}}(\%) = E \cdot Q_{\text{in}} \tag{3.35}$$

where E is a parameter to be calculated and Q_{in} is

$$Q_{\text{in}} = \frac{\omega L_1}{R_{\text{in}}} \tag{3.36}$$

By substituting (3.36) in (3.35) and the result in (3.34), we obtain

$$\Delta R_{\text{in}} = E\omega L_1 \tag{3.37}$$

In order to properly detect $R_{in,max}$, we must accomplish

$$R_{\text{in,max}} - R_1 > \Delta R_{\text{in}}|_{\omega=\omega_{\text{r}}} = E\omega_{\text{r}} L_1 \tag{3.38}$$

Then, by substituting (3.13) into (3.38) and further processing we get

[1] The term "accuracy" is used by the manufacturer. Here we use the term "uncertainty".

$$k > \sqrt{\frac{E}{Q_T}} \tag{3.39}$$

which denotes the minimum required value of k (k_{min}) in order to detect ω_r. Lower values of E and higher values of Q_T decrease the required value of k_{min}, which increases the maximum achievable distance. As can be seen, the quality factor of the reader coil, Q_R, does not limits the value of k_{min}.

Table 3.2 shows the values of E, k_{min} and d_{max} for case 2, which is the worst case in terms of Q_T (see Table 3.1), and thus on the achievable distance. In our case, the values of E were calculated from the operation manual of the impedance analyzer [65] (see Appendix A). Two values were used corresponding respectively to BW = 5 (highest accuracy) and BW = 1 (lowest accuracy). The considered value for Q_T was 26.6, the minimum one in Table 3.1. Then, k_{min} was obtained from (3.39). The corresponding values of d_{max} were inferred from Fig. 3.14. The resulting maximum distances are of 3.7 cm (for BW = 5) and of 2 cm (for BW = 1). The predicted distances are lower than those that can actually be achieved with BW = 1. As an example, Fig. 3.20 shows that at 3 cm a correct detection is still possible. This issue is explained because the observed uncertainty in the measurements is better than that provided in the specifications of the impedance analyzer. Surely, the manufacturer specifies a higher bound for the uncertainty.

Table 3.2 Values of E, k_{min} and d_{max} for case 2.

	E	k_{min}	d_{max}
BW=1	0.88 %	0.018	2 cm
BW=5	0.08 %	0.005	3.7 cm

Chapter 4 Resonant Inductive Power Transmission for Autonomous Sensors

Inductive power transmission (IPT) allows transferring energy wirelessly by using a coupled pair of coils. This can be advantageous in applications where the use of a physical connection between the electronic system to be powered and its power source is disadvantageous or unfeasible. Both high- and low-power applications have been reported. High-power transfer includes battery recharging of electrical vehicles [33] and a broad range of industrial applications [34]-[40], whereas low-power transfer includes RFID systems [66], biomedical implants [54], or portable consumer electronic products [41], [67]. In this last area, there is an increasing interest of industry and, as a result, new products have appeared in the form of power surfaces (e.g. Powermat) and a new consortium of companies (Wireless Power Consortium) has been created in order to generate interoperable products.

Transmission power distance is, in general, shorter than the diameter of the powering coils. However, Kurs et al. showed a power transfer of 60 W over distances in excess of 2 m by using coils with a diameter of 60 cm [68]. Coil-to-coil efficiency was of 40 %. Their analysis is rather based on physical theory and more engineering focused approaches using circuit lumped circuits have appeared since then [69], [70]. The same principle has also been explored for powering multiple receivers from a single transmitter coil [71] and biomedical implants [72]. In most of these works, four coils are used, two for the transmitter side and other two for the receiver side. In order to counteract the loose coupling between the transmitter and receiver, series or parallel resonant coupling is implemented. Although the topic has received great interest and propaganda, it does not seem very different from previous existing approaches in which two loosely coupled coils were tuned in resonance [73], [74].

Vehicles can also benefit from IPT, in particular to power autonomous sensors installed in rotating parts such as wheels or in removable parts such as seats. As for the wheels, tire-pressure monitoring systems (TPMS) are already mandatory in USA and will be in the EU for vehicle types of category M1 or N1 [4] granted as from 1 November 2012 or first registered as from 1 November 2014 [5]. Currently, TPMS are powered by primary batteries. However, as the desired target for the lifetime of batteries is about 10 years, the use of batteries is challenging. In addition, the final disposal of millions of batteries will create environmental impacts and hazards. As an alternative, an Australian company is offering a battery-less IPT-based TPMS [75].

As for the removable seats, some vans and minivans incorporate them in order to flexibly arrange their internal space. Some commercial models incorporate at most a seat belt detector for the removable seats. In order to avoid wiring the seats, a passive detection is performed via

an inductive link. In Chapter 3, we have proposed seat occupancy and belt detection in vehicle removable seats via passive inductive coupling. However, more intelligent systems will be required. As for 2012, an NHTSA regulation (USA) requires the use of intelligent airbags that minimize the risk to infants and children. Intelligent airbags must be deployed depending on whether the passenger is an adult, an infant car seat is present, or the seat is empty. These airbags should avoid the problems encountered with previous airbag systems [76]. The sensors used for these intelligent airbags may require power to operate. One option for removable seats, apart from using primary batteries, is the transmission of power via inductive links from the chassis floor to the seat.

This chapter explores the feasibility of using IPT for autonomous sensors and in particular for belt and occupancy detection in removable vehicle seats. A pair of coils would be aligned and placed respectively in the chassis floor and at the bottom of the removable seat, as shown in Fig. 1.2. The final aim is to maximize the power efficiency and the powering distance range between the coupled pair of coils in order to relax the mechanical constraints. The power demand of the autonomous sensor is considered of 100 mW, which is the typical power consumption of radio-frequency (RF) transceivers used in them. As a means to transfer power at "mid-range" distances (higher than the radius of the coils), two loosely coupled coils tuned in resonance have been considered. The selected application is considered to be space-constrained, so that small-size coils have to be used. Even though a particular application is selected, the analysis and conclusions drawn are rather general and can be useful for low-power applications that require autonomous sensors to be inductively powered. Autonomous sensors require of a DC voltage supply and, consequently, of a voltage regulator. A comprehensive analysis of the impact on the system efficiency of different voltage regulators is also provided and the best regulator type is determined. Both analytical derivations and experimental results are provided.

4.1 Analysis of IPT Systems

IPT allows transmitting energy between a pair of coupled coils in order to power a load. To counteract the loose coupling between the coils ($k << 1$) compensation capacitors are used. Capacitors can be placed in series or parallel with the coils, leading respectively to series or parallel resonant tanks.

Fig. 4.1 shows the equivalent circuit of a pair of magnetically coupled resonators. The left-hand and right-hand sides of the circuit correspond to the transmitting (primary) and receiving (secondary) networks, respectively. Both series and parallel resonant tanks are considered for the primary and secondary networks, thus resulting in four possible topologies, referred hereinafter as SS, SP, PS, and PP. The letter S or P stands for series or parallel compensation; the first and second letters stand for the primary and secondary networks, respectively.

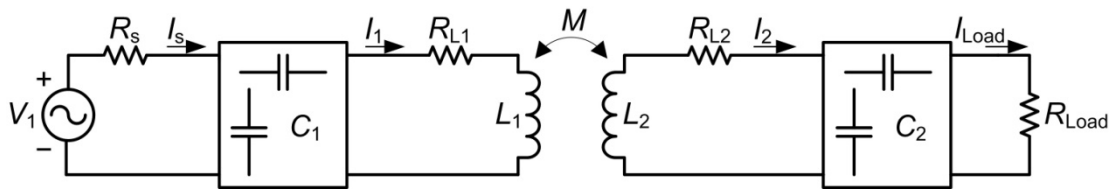

Fig. 4.1 Equivalent circuit of a pair of magnetically coupled resonators.

In this work, we assume a fixed voltage and frequency for the power source of the primary network. V_1 is a sinusoidal signal that models the voltage output of the power source that drives the primary network; I_1 and I_2 stand for the currents of the primary and secondary networks; L_1 and L_2 model the coils; C_1 and C_2 are the compensation capacitors to work at resonance; R_s and I_s model respectively the output resistance and current of the power source; R_{L1} and R_{L2} model the losses of the coils; R_{Load} and I_{Load} respectively model the load and the current through it; and finally M models the mutual inductance between the coils. Losses of the coils account for that due to the resistance of the winding wire, including the skin and proximity effects, and core losses. Hereinafter, the parameters of voltage and current are assumed to be root-mean-square values by default.

The circuit of Fig. 4.1 can be transformed, taking into account (2.43), into the circuit of Fig. 4.2.

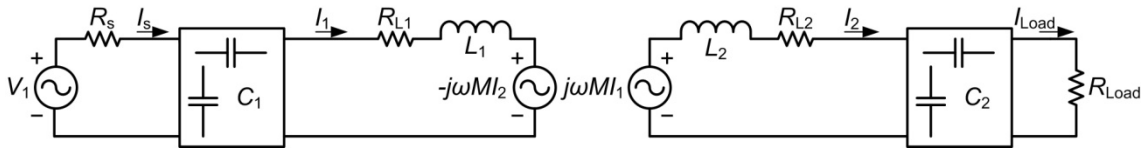

Fig. 4.2 Equivalent primary and secondary networks taking into account (2.43).

From the analysis of the secondary network we obtain

$$I_2 = \frac{j\omega M I_1}{Z_2} \tag{4.1}$$

where

$$\begin{cases} Z_2 = R_{\text{Load}} + R_{\text{L2}} + j\omega L_2 + \dfrac{1}{j\omega C_2} & \text{For a series resonant tank} \\ Z_2 = R_{\text{L2}} + j\omega L_2 + \dfrac{1}{j\omega C_2 + \dfrac{1}{R_{\text{Load}}}} & \text{For a parallel resonant tank} \end{cases} \tag{4.2}$$

Thus, by substituting (4.1) into the reflected voltage of the primary network, $-j\omega MI_2$, we arrive to the equivalent circuit of Fig. 4.3.

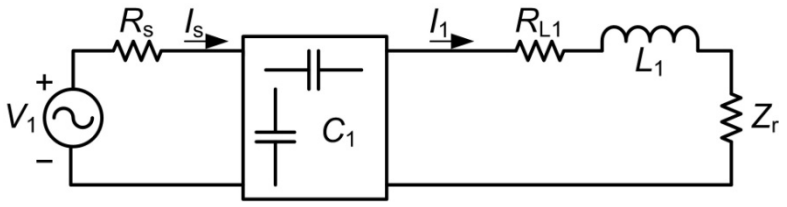

Fig. 4.3 Primary network with the reflected impedance.

where

$$Z_{\mathrm{r}} = \frac{(\omega M)^2}{Z_2} \tag{4.3}$$

is the reflected impedance from the secondary to the primary network.

Thus,

$$V_1 = Z_{\mathrm{t}} I_{\mathrm{s}} \tag{4.4}$$

where

$$\begin{cases} Z_{\mathrm{t}} = R_{\mathrm{s}} + R_{\mathrm{L1}} + j\omega L_1 + \dfrac{1}{j\omega C_1} + Z_{\mathrm{r}} & \text{For a series resonant tank} \\ Z_{\mathrm{t}} = R_{\mathrm{s}} + \dfrac{1}{j\omega C_1 + \dfrac{1}{R_{\mathrm{L1}} + j\omega L_1 + Z_{\mathrm{r}}}} & \text{For a parallel resonant tank} \end{cases} \tag{4.5}$$

is the impedance seen by the power source. The power transmitted to the secondary network is

$$P_{\mathrm{T}} = I_1^2 \mathrm{Re}\{Z_{\mathrm{r}}\} \tag{4.6}$$

where the operator Re{ } stands for the real part of the involved parameter, whereas the received power at R_{Load} is given by

$$P_{\mathrm{Load}} = P_{\mathrm{T}} \frac{R_{\mathrm{Load}}}{R_{\mathrm{L2}} + R_{\mathrm{Load}}} \tag{4.7}$$

The compensation capacitors are used to maximize P_{T} and P_{Load}. An approach followed in the literature [77]-[79] is, first, to fix the working frequency of the power source to

$$\omega_{\mathrm{r}} = \frac{1}{\sqrt{L_2 C_2}} \tag{4.8}$$

i.e. in function of the reactive components of the secondary network. The real and imaginary parts of Z_{r} are shown in Table 4.1 for the series and parallel resonant tanks of the secondary

network. For the sake of simplicity, R_{L2} has been neglected in the analysis. As can be seen, for the series-compensated network no reactance is reflected and the reflected resistance depends inversely on the load resistance (R_{Load}). Contrariwise, the parallel-compensated network reflects a capacitive reactance and the reflected resistance depends directly on R_{Load}. The reflected reactance depends on the coupling factor k.

Table 4.1 Reflected impedance of the series- and parallel-compensated networks.

Compensation	Series	Parallel
Reflected resistance	$k^2 \frac{L_1}{C_2 R_{\mathrm{Load}}}$	$k^2 \frac{L_1}{L_2} R_{\mathrm{Load}}$
Reflected reactance	0	$-\omega k L_1$

Secondly, C_1 is selected in order to null the reactance in the primary network at ω_r, i.e.

$$\mathrm{Im}\{Z_t\}|_{\omega_r} = 0 \tag{4.9}$$

and thus to maximize P_T. The operator Im{ } stands for the imaginary part of the involved parameter. The resulting values of C_1 for the different topologies are shown in Table 4.2, where the parameter C_{10} is a normalized capacitance of C_1 which results from

$$\omega_r = \frac{1}{\sqrt{L_1 C_{10}}} \rightarrow C_0 = \frac{1}{\omega_r^2 L_1} \tag{4.10}$$

and substituting (4.8) in (4.10)

$$C_{10} = \frac{C_2 L_2}{L_1} \tag{4.11}$$

In the analysis, the coil resistances (R_{L1}, R_{L2}) and the output resistance of the power source (R_s) are neglected. These results were previously presented in [78] and [79]. However, their expressions contain an error consisting on a missing square in R_{Load} for the topologies PS and PP.

Table 4.2 Resulting values of C_1 for the four topologies in order to null the reactance in the primary network.

Topology	Primary Capacitance (C_1)
SS	C_{10}
SP	$\frac{C_{10}}{1-k^2}$
PS	$\frac{C_{10}}{1+k^2\frac{L_2}{C_2 R_{\text{Load}}^2}}$
PP	$\frac{C_{10}(1-k^2)}{1-k^2+k^4\frac{C_2}{L_2}R_{\text{Load}}^2}$

As can be seen, the selected topology has a remarkable influence on the selected value of C_1. For the SS topology we can directly use C_{10}. For the SP topology we find a dependence on the coupling factor k, which arises from the reflected reactance of the secondary parallel network, as Table 4.1 shows. Thus, C_1 must be tuned at each specific distance between the coils. Even though a fixed distance between the coils can be selected in our case for a specific vehicle model, mechanical tolerances could force to an individual tuning process once the system is installed inside each vehicle, which can be inconvenient. Topologies that use the parallel compensation in the primary network, i.e. PS and PP topologies, show a dependence on k but also on R_{Load}. Their dependency on R_{Load} arises from the dependency on R_{Load} of the reflected resistance. As will be seen later, R_{Load} models an autonomous sensor in our case and its value depends on its power consumption but also on the voltage regulator used to provide a fixed DC voltage. So, because of expected variations in R_{Load}, the use of those topologies can be problematic in order to achieve the condition stated in (4.9). Topology SS shows no dependence on k and R_{Load}, which eases the tuning process.

Another approach that will be further explored in section 4.3 for the SP topology is to select an appropriate value of C_2 in order to achieve

$$Im(Z_{\text{r}}) = 0 \tag{4.12}$$

at the resonant frequency

$$\omega_r = \frac{1}{\sqrt{L_1 C_1}} \tag{4.13}$$

In sections 4.2 and 4.3 we will analyze in more detail the SS and SP topologies taking into account the previous neglected resistances R_{L1}, R_{L2}, and R_s. Topologies PS and PP will not be further considered in this work.

4.2 SS Topology

Fig. 4.4 shows the equivalent circuit for the SS topology.

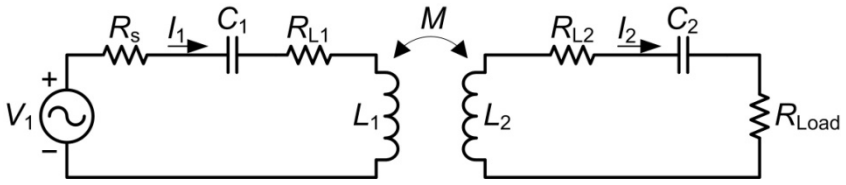

Fig. 4.4 Equivalent circuit for the SS topology.

From the analysis of the circuit of Fig. 4.4, we obtain

$$\begin{aligned} V_1 &= Z_1 I_1 - j\omega M I_1 \\ j\omega M I_1 &= Z_2 I_2 \end{aligned} \tag{4.14}$$

where

$$Z_1 = R_s + R_{L1} + j\omega L_1 + \frac{1}{j\omega C_1} \tag{4.15}$$

and Z_2 was defined in eq (4.2) for the series network.

Based on the discussion of section 4.1, the primary and secondary networks are tuned at the same resonance frequency and the power source is tuned at resonance, i.e. $\omega = \omega_r$, where

$$\omega_r = \frac{1}{\sqrt{L_1 C_1}} = \frac{1}{\sqrt{L_2 C_2}} \tag{4.16}$$

Thus, (4.14) can be simplified to

$$\begin{aligned} V_1 &= R_1 I_1 - j\omega M I_2 \\ j\omega M I_1 &= R_2 I_2 \end{aligned} \tag{4.17}$$

where $R_1 = R_s + R_{L1}$ and $R_2 = R_{L2} + R_{Load}$.

On the other hand, eq. (4.7) can be expressed as

$$P_{\text{Load}} = \left(\frac{V_{1,\text{rms}}}{R_1 + R_\text{r}}\right)^2 R_\text{r} \frac{R_{\text{Load}}}{R_2} \tag{4.18}$$

where

$$R_r = \frac{(\omega_\text{r} M)^2}{R_2} \tag{4.19}$$

is the reflected resistance onto the primary network. As can be seen, R_r depends on M and thus on distance. On the other hand, we define the primary (η_1), secondary (η_2), and load (η_{Load}) efficiencies as

$$\eta_1 = \frac{P_\text{r}}{P_\text{g}} = \frac{R_\text{r}}{R_\text{r} + R_1} \tag{4.20}$$

$$\eta_2 = \frac{P_{\text{Load}}}{P_\text{r}} = \frac{R_{\text{Load}}}{R_2} \tag{4.21}$$

$$\eta_{\text{Load}} = \frac{P_{\text{Load}}}{P_\text{g}} = \eta_1 \eta_2 \tag{4.22}$$

where P_g is the generated power of the power source. Thus, by using (4.20) and (4.21) in (4.18), we can rewrite P_{Load} as

$$P_{\text{Load}} = \frac{{V_1}^2}{R_1} \eta_1 (1 - \eta_1) \eta_2 \tag{4.23}$$

In the remaining part of this section we will assess the evolution of both P_{Load} and η_T first in function of k and then of R_{Load}.

4.2.1 Effects of the distance

Loosely coupling IPT systems achieve short powering distances. The introduction of compensation capacitors aims to increase the powering distance range and the power efficiency. Here, we will assess how P_{Load} and η_{Load} evolve in function of k, and thus of distance, assuming a fixed R_{Load}.

Fig. 4.5 shows parameterized graphs of both P_{Load} and η_1 with respect to k, where k can range from 0 to 1. Graphs are processed from the previous presented equations.

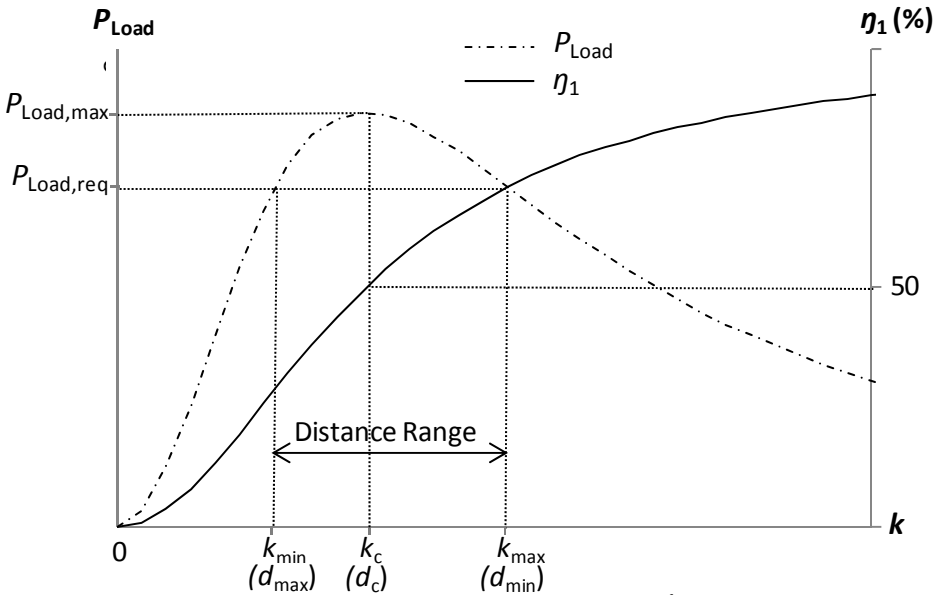

Fig. 4.5 Evolution of P_{Load} and η_1 with respect to k.

As can be seen, P_{Load} presents a maximum ($P_{Load,max}$) at k_c, which is referred in the literature either as *critical coupling* [69], [74] or *optimal coupling* [80] and is found by solving $\partial P_{Load}/\partial k = 0$, resulting in

$$k_c = \frac{1}{\sqrt{Q_1 Q_2}} \tag{4.24}$$

where

$$Q_i = \frac{\omega_r L_i}{R_i}, \qquad i = 1,2 \tag{4.25}$$

are the quality factors of the primary (Q_1) and secondary (Q_2) networks. We define d_c, shown in Fig. 4.5, as the *critical distance* at which (4.24) holds. At $k = k_c$ ($d = d_c$), $\eta_1 = 0.5$ and $R_r = R_1$. At shorter distances, $R_r > R_1$, and at larger distances $R_r < R_1$. In both cases, P_L gradually decreases.

As for the efficiencies, η_1 monotonically decreases for increasing distances (decreasing values of k) whereas η_2 (not shown in Fig. 4.5) remains constant.

The maximum value of P_{Load} is given by

$$P_{Load,max} = \frac{{V_1}^2}{4R_1}\eta_2 \tag{4.26}$$

and using (4.26) in (4.23) we can rewrite P_{Load} as

$$P_{\text{Load}} = 4P_{Load,max}\eta_1(1-\eta_1) \tag{4.27}$$

$P_{\text{Load,req}}$, shown in Fig. 4.5 as a straight line, represents the amount of power required by the load in order to properly work. As can be seen in Fig. 4.5, $P_{\text{Load,req}}$, can be achieved for a restricted range of coupling factors, [k_{min}, k_{max}], and thus of distances, [d_{min}, d_{max}]. This distance range can be enlarged by increasing $P_{\text{Load,max}}$ either by increasing V_1 or decreasing R_1. However, this leads to a more stringent design for the driver transistors, compensation capacitor, and coil of the primary network (see section 4.5), and to a lower primary efficiency (η_1) at the resulting higher d_{max}.

As for the coils, magnetic- instead air-core coils can be used in order to increase d_{max} (Fig. 4.5). Given that the application is space constrained we selected small-size ferrite-core coils from Fastron (PIST model). Fig. 3.10 shows the dimensions of these coils.

Fig. 3.14 shows simulated results of k vs d (from 0 cm to 3 cm in steps of 0.5 cm) both for the selected Fastron coils and for an air-core coil of the same dimensions. As can be seen, for a given value of k, ferrite-core coils lead to a larger distance. Thus, from Fig. 4.5, the same value of k_{min} will lead to a higher d_{max} with ferrite-core than with air-core coils. On the other hand, for a given distance, ferrite-core coils lead to a higher value of k and thus, from Fig. 4.5, to a larger value of η_1 and thus of η_{Load}.

A complementary alternative to increase either d_{max} or η_1 is to increase d_c, which can be achieved by decreasing the value of k_c. From (4.24), k_c can be decreased by increasing Q_1 and Q_2. The parameter Q_1 can be expressed as

$$Q_1 = \frac{Q_s Q_{L1}}{Q_s + Q_{L1}} \tag{4.28}$$

where

$$Q_s = \frac{\omega_r L_1}{R_s} \tag{4.29}$$

and

$$Q_{L1} = \frac{\omega_r L_1}{R_{L1}} \tag{4.30}$$

being Q_{L1} the quality factor of L_1. Thus, from (4.28), to achieve a high value of Q_1, both Q_s and Q_{L1} need to be high. For a given R_s, Q_s can be increased both by increasing ω_r and the coil value. We limited the working frequency to 150 kHz in order to better comply with the ICNIRP

guidelines [55]. As for the coil value, the use of a ferrite-core provides benefits as it leads to a higher value. In particular, for the selected coils (Fig. 3.10), the COMSOL simulations provided a ten-fold increase of the ferrite- over the air-core coil. On the other hand, for a given geometry and core material, a higher coil value can be achieved by increasing the number of the winding turns and thus of the coil resistance (R_{L1}), which in turn implies a higher value of R_1. From (4.26), a larger R_1 will reduce the value of $P_{Load,max}$.

A similar argument can be drawn for Q_2. The parameter Q_2 can be expressed as

$$Q_2 = \frac{Q_{L2} Q_{Load}}{Q_{L2} + Q_{Load}} \tag{4.31}$$

where

$$Q_{Load} = \frac{\omega_r L_2}{R_{Load}} \tag{4.32}$$

and

$$Q_{L2} = \frac{\omega_r L_2}{R_{L2}} \tag{4.33}$$

being Q_{L2} the quality factor of L_2. Thus, from (4.31), to achieve a high value of Q_2, both Q_{Load} and Q_{L2} need to be high. As for the series resonant tank, in order to achieve a high value of Q_{L2} we need, from (4.32), a high value of L_2. However, the increase of the coil resistance (R_{L2}) will lead, from (4.20), to a decrease of η_2 and then, from (4.26), of $P_{Load,max}$.

Overall, the increase of d_c achieved by increasing Q_1 and Q_2, does not necessarily leads to an increase of d_{max} due to the simultaneous decrease of $P_{Load,max}$. On the other hand, the increase of η_1 due to the increase of d_c can be neutralized by a simultaneous decrease of η_2 due to the increase of R_{L2}. Thus, a case by case study will be necessary in order to select appropriate values for ω_r and the coils. We present this study and the related experimental results in Appendix B, where the SP topology has also been assessed.

4.2.2 Effects of R_{Load}

The value of R_{Load} changes with the power consumption of the load and also with the kind of voltage regulator used, as will be seen later. So, the evolution of P_{Load} and η_T in function of R_{Load} will be assessed in this section, assuming a fixed distance (d). A maximum of P_{Load} can be found by solving $\partial P_{Load}/\partial R_{Load} = 0$, obtaining

$$P_{\mathrm{Load,max}} = \frac{V_1^2}{4R_1}\frac{(\omega M)^2}{R_1 R_{\mathrm{L2}} + (\omega M)^2} = \frac{V_1^2}{4R_1}\frac{k^2 Q_1 Q_{\mathrm{L2}}}{1 + k^2 Q_1 Q_{\mathrm{L2}}} \tag{4.34}$$

being the optimum load

$$R_{\mathrm{Load,optP}} = R_{\mathrm{L2}} + \frac{(\omega M)^2}{R_1} = R_{\mathrm{L2}}(1 + k^2 Q_1 Q_{\mathrm{L2}}) \tag{4.35}$$

The same result of (4.35) can be easily inferred from the equivalent circuit of the secondary network shown in Fig. 4.6, which can be inferred by further processing (4.17) as

$$\frac{j\omega M}{R_1}\mathrm{V}_1 = \left(\frac{(\omega M)^2}{R_1} + R_{\mathrm{L2}} + R_{\mathrm{Load}}\right) I_2 \tag{4.36}$$

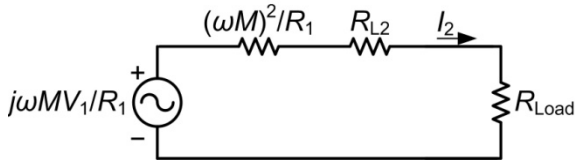

Fig. 4.6 Equivalent circuit of the secondary network.

On the other hand, a maximum value of η_{Load} is found by solving $\partial\eta_{\mathrm{T}}/\partial R_{\mathrm{Load}} = 0$, obtaining

$$\eta_{\mathrm{Load,max}} = \frac{k^2 Q_1 Q_{\mathrm{L2}}}{\left(1 + \sqrt{1 + k^2 Q_1 Q_{\mathrm{L2}}}\right)^2} \tag{4.37}$$

being the corresponding optimal load

$$R_{\mathrm{Load,opt\eta}} = R_{\mathrm{L2}}\sqrt{1 + k^2 Q_1 Q_{\mathrm{L2}}} \tag{4.38}$$

The relationship between (4.35) and (4.38) is

$$\frac{R_{\mathrm{Load,optP}}}{R_{\mathrm{Load,opt\eta}}} = \sqrt{1 + k^2 Q_1 Q_{\mathrm{L2}}} \tag{4.39}$$

So, $R_{\mathrm{Load,optP}}$ will always be higher than $R_{\mathrm{Load,opt\eta}}$. Fig. 4.7 shows a parameterized graph of the evolution of P_{Load} and η_{Load} with respect to R_{Load}. As for η_{Load}, η_1 and η_2 are shown. For high values of R_{Load}, η_2, from (4.21), will tend to the unity. On the other hand, the maximum value of η_1, which is attained at $R_{\mathrm{Load}} = 0$, will decrease for increasing distances.

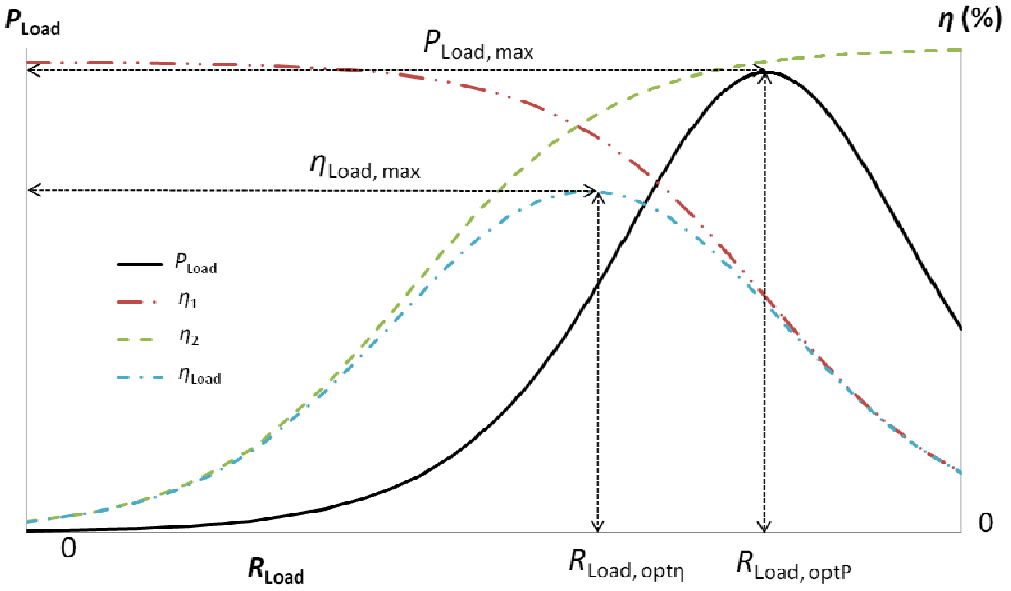

Fig. 4.7 P_{Load} vs R_{Load}.

In this case, ferrite-core coils are also preferred against air-core coils as they lead to higher coupling and quality factors. Thus, from (4.34) and (4.37) higher values of P_{Load} and η_T can be achieved.

4.3 SP Topology

Fig. 4.8 shows the equivalent circuit of a SP topology.

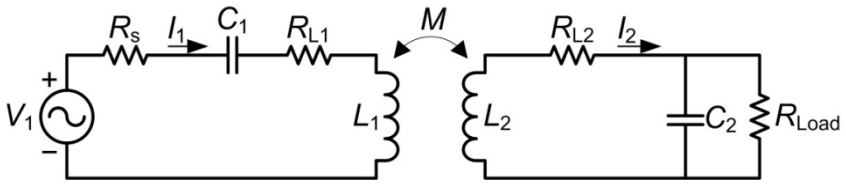

Fig. 4.8 Equivalent circuit for a SP topology.

Assuming we comply with (4.8) and considering now in the analysis R_{L2}, the reflected reactance depends both on k and R_{Load}, being the resulting C_1

$$C_1 = \frac{C_{10}}{1 - k^2 \dfrac{L_2^2}{R_{L2}^2 L_2 C_2 + (R_{Load} R_{L2} C_2 + L_2)^2}} \tag{4.40}$$

and

$$Q_{Load} = \omega_r C_2 R_{Load} = \frac{R_{Load}}{\omega_r L_2} \tag{4.41}$$

As briefly mentioned at the end of section 4.1, another approach for the SP topology is to accomplish (4.12) and (4.13). After some processing, the resulting value of C_2 is given by

$$C_2 = \frac{L_1 C_1}{2L_2}\left(1 \pm \sqrt{1 - \frac{4L_2^2}{L_1 C_1 R_{\text{Load}}^2}}\right) \tag{4.42}$$

which depends on R_{Load}. Obviously, in order to obtain real values, the term inside the square root must be greater than zero. Thus, the selected inductance of the secondary network must accomplish

$$L_2 \leq \frac{R_{\text{Load,p}}}{2\omega_{\text{r}}} \tag{4.43}$$

Q_{Load} is now given by

$$Q_{\text{Load}} = \omega_{\text{r}} C_2 R_{\text{Load}} = \frac{R_{\text{Load}}}{2\omega_{\text{r}} L_2}\left(1 \pm \sqrt{1 - \frac{4L_2^2}{L_1 C_1 R_{\text{Load}}^2}}\right) \tag{4.44}$$

The highest value of Q_{Load} out of the two possible ones is of interest, which corresponds to the highest value of C_2 in (4.42).

In applications where R_{Load} is relatively high, (4.40) and (4.42) reduce their dependency on R_{Load}. Further, with low values of ω_{r} and L_2, high values of Q_{Load} can be achieved. High values of R_{Load} lead to low values of Q_{Load} for the SS topology, as can be inferred from (4.32). So, SS and SP topologies are complementary. In this work, the SS topology has been mainly considered as it eases the tuning process and the considered values for R_{Load} are relatively low, as will be shown later. Even so, in Appendix B, the evolution of P_{Load} versus k has been assessed for the SP topology by using (4.42) for C_2.

4.4 Coils

As mentioned before, commercial ferrite-core coils were selected. As for the coil values, we selected the first value of each decade provided by the manufacturer and covered the full available range, i.e. 10 µH, 100 µH, 1 mH, and 10 mH. In this section we present the results of their coil resistances and quality factors. First, their resistance was measured at several frequencies. In order to obtain the resistance values, we used a series-resonant network and measured the resistance at the resonant frequency by using an HP4294A impedance analyzer. Appropriate values of capacitors were used in order to tune different resonant frequencies within the range from 1 kHz to 150 kHz (this upper limit is justified in section 4.5). Fig. 4.9

shows the results. As can be seen, resistance values increased with frequency, which is due to the joint combination of skin and proximity effects and the losses of the ferrite [53]. Then, the quality factors were inferred by using the measured resistances and the nominal values of the inductances. Fig. 4.10 shows the results. Resulting quality factors increased steeply at low frequencies. A maximum was achieved around 40 kHz for 100 µH and 1 mH. For the other two coils, 10 µH and 10 mH, the maximum value was achieved at the highest tested frequency, approximately 120 kHz. On the other hand, the achieved maximum value at a given frequency increased with an increase of the coil value.

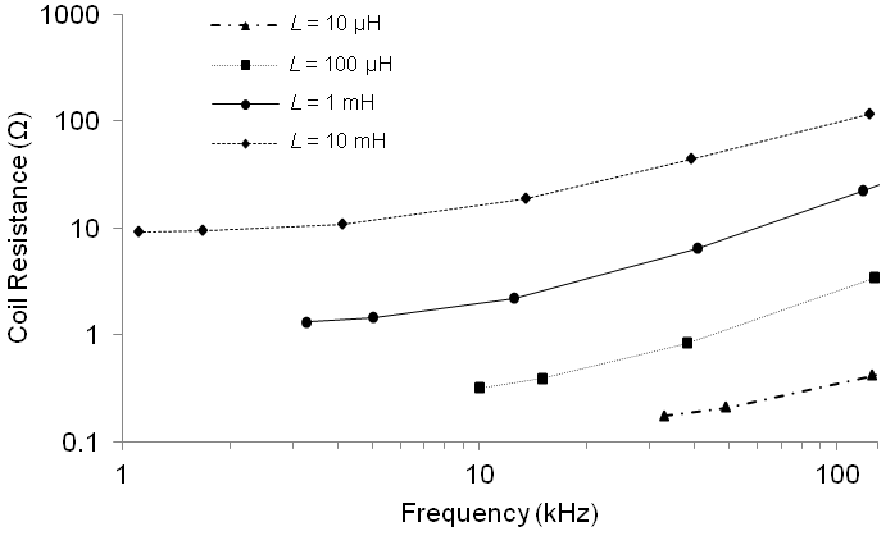

Fig. 4.9 Resistance values of the Fastron commercial coils.

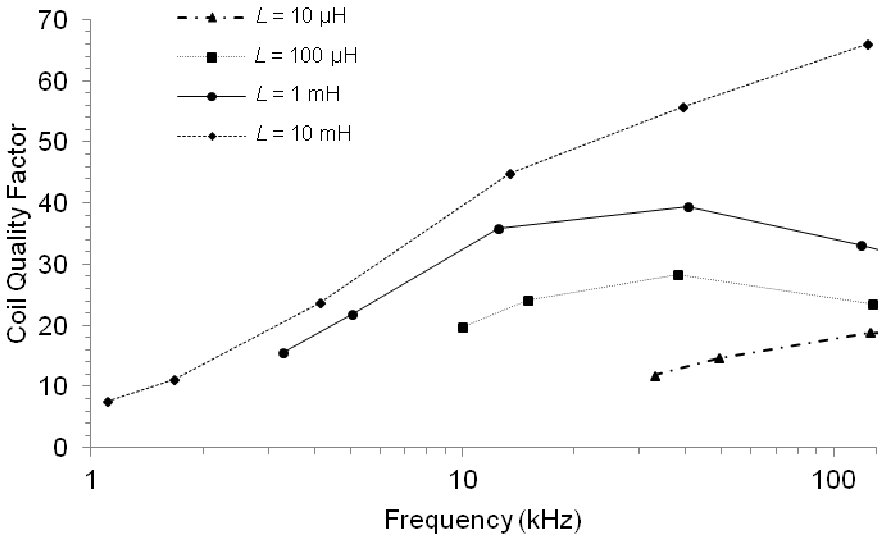

Fig. 4.10 Values of the resulting quality factors for the Fastron commercial coils.

As for the primary coil L_1, the highest two coil values, 1 mH and 10 mH, were selected as from Fig. 4.10 they provide the highest quality factors (Q_{L1}) and a high value of Q_s. As for the

secondary coil L_2, the same coils were again selected for the series resonant tank (Fig. 4.4) as they provide both high values of Q_{L2} and Q_{Load}. For the parallel resonant tank (Fig. 4.8), though, the lowest two values, 10 μH and 100 μH, would be selected in order to get reasonable values of Q_{Load}. However, this leads, as can be seen from Fig. 4.10, to relative low values of Q_{L2}. Thus, in order to achieve higher values of Q_{L2}, the SS topology is also more advantageous than the SP topology. Appendix B shows some related results.

4.5 Primary Network

A rather low frequency of operation (< 150 kHz) was selected for two reasons: 1) to better comply with the reference levels for general public exposure to time-varying electric and magnetic fields [55], and 2) to reduce the circuit complexity and power losses of the power amplifier.

Based on these premises, Fig. 4.11 shows the circuit schematic of the implemented primary network. It is mainly composed of a class D power amplifier based on a low-cost commercial self-oscillating half-bridge driver (IR2153) and two external N-channel MOSFETs (BSH103, Philips Semiconductor), M1 and M2. The driver, powered at 12 V DC (V_{cc}, battery voltage in vehicles), alternatively activates the two MOSFETs, thus injecting a square wave signal into the resonant network. The operating frequency, fixed by the R_bC_b network, can be finely tuned, using a multi-turn potentiometer for R_b, to the resonant frequency of the series resonant tank L_1C_1.

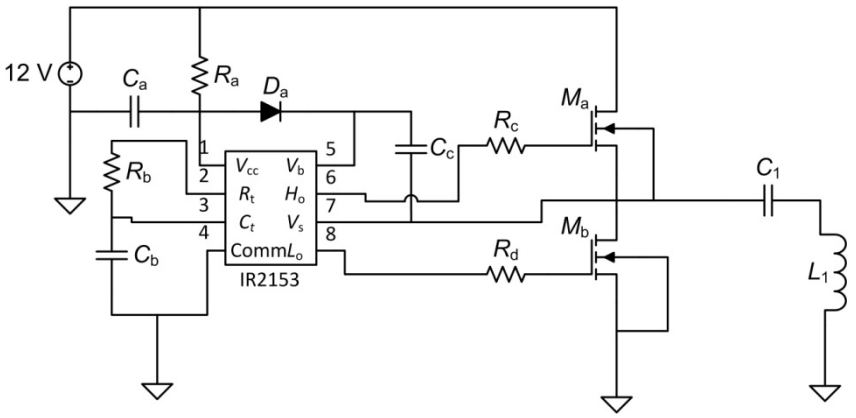

Fig. 4.11 Schematic circuit of the primary network.

For moderate to high quality factors, only the first voltage harmonic (V_1 in Fig. 4.4) will generate a (sinusoidal) current through the network, being its theoretical amplitude of 7.64 V ($2V_{cc}/\pi$) and its rms value (V_1) of 5.4 V.

The MOSFET manufacturer publishes an ON resistance (R_{ON}) of 0.4 Ω (@ V_{GS} = 2.5 V). The overall resistance of the primary network is $R_1 + R_r$, where $R_1 = R_s+R_{L1}$. R_s is given by R_{on}

whereas the value of R_{L1} depends on the selected coil and resonance frequency. Section 4.4 described the selected coils and associated coil resistances at different frequencies.

4.6 Receiving Network

Autonomous sensors require a fixed DC voltage supply. So, a rectifier and some kind of voltage regulation are required in the secondary network. For high-power (7-30 W) biomedical implants, power dissipation at the implanted device should be minimized in order to avoid heating the tissue. As such, closed-loop regulation methods are adopted where either the input voltage or the operating frequency of the power converter of the external primary network is controlled [82]. There, an internal radiofrequency transceiver is needed to transmit the value of the DC load voltage of the secondary network to an external transceiver connected to the primary network. So, the system design is relatively complex. For lower power biomedical implants, e.g. < 500 mW, voltage regulator chips are used at the internal secondary network, thus avoiding the use of an external control loop [54], [83], [84]. Different types of voltage regulators can be used, such as linear shunt and series regulators, and switching regulators. However, their impact on the system power efficiency has not been thoroughly assessed in the literature. We will use this approach here and perform a comprehensive analysis.

Fig. 4.12 shows the block schematic of such a disposition, where only the series resonant tank considered.

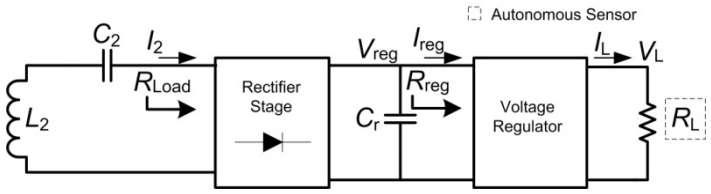

Fig. 4.12 Block diagram of the secondary network that includes the rectifier and voltage regulator.

As can be seen, V_L, I_L and R_L are respectively the voltage supply, current consumption and equivalent resistance load of the autonomous sensor, where

$$V_L = I_L R_L \tag{4.45}$$

V_{reg}, I_{reg} and R_{reg} are respectively the voltage, current and equivalent resistance at the input of the voltage regulator, where

$$V_{reg} = I_{reg} R_{reg} \tag{4.46}$$

and R_{Load} is the equivalent resistance seen from the input of the rectifier. R_{reg} depends on R_L and on the specific type of voltage regulator. R_{Load} depends on R_{reg} and the type of rectifier employed. Finally, C_r is a filter capacitor.

The circuit of Fig. 4.12 can be transformed, using the circuit of Fig. 4.6, to the equivalent circuit of Fig. 4.13 where

$$V_{\mathrm{T}} = \frac{j\omega M V_1}{R_1}$$
$$R_{\mathrm{T}} = \frac{(\omega M)^2}{R_1} + R_{\mathrm{L2}} \tag{4.47}$$

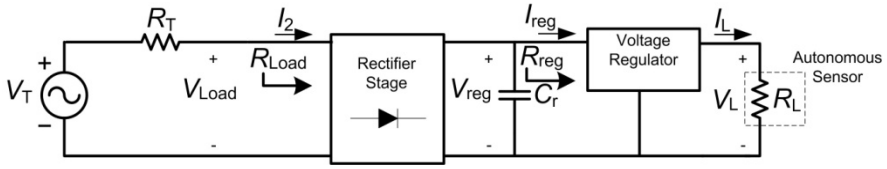

Fig. 4.13 Equivalent circuit of the secondary network that includes the rectifier and voltage regulator.

In the remainder of this section we analyze in detail the different stages.

4.6.1 Autonomous Sensor

Autonomous sensors are low-power devices mainly composed of sensors, a microcontroller and a radiofrequency (RF) transceiver. In this work, the autonomous sensor will be in charge of occupancy and belt detection in removable vehicle seats.

Fig. 4.14 shows the schematic circuit of the autonomous sensor. The sensors (or detectors) where described in section 1.1.2. An ETRX-2 device (Telegesis), which embeds a microcontroller and an RF transceiver, was used to sense the state of the sensors and transmit the information wirelessly using the embedded Zigbee stack. Other communication standards such as Bluetooth, more common in vehicles, could be used. Appropriate resistors (R_a and R_b) were placed in series with the sensors in order to form voltage dividers. Their outputs were respectively connected to the inputs (ADC1 and ADC2) of the ETRX-2 built-in analog-to-digital (ADC) converter.

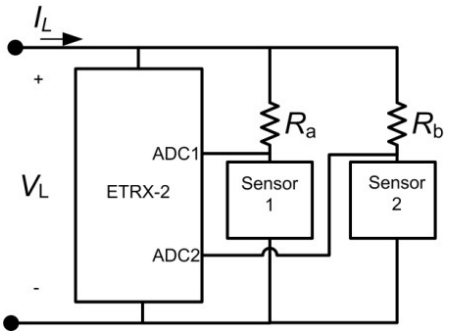

Fig. 4.14 Schematic circuit of the autonomous sensor.

The supply voltage, V_L, was set to 3 V by the output of a voltage regulator. Current consumption (I_L) was measured to be *ca*. 30 mA and was mainly fixed by that of the ETRX-2 device. So, $R_L \approx 100\ \Omega$ and $P_L \approx 90$ mW result. To determine the value of R_{Load}, in Fig. 4.3, the effects of the rectifier stage and the voltage regulators must be taken into account.

4.6.2 Rectifier Stage

For a series-resonant secondary tank, the rectifier must allow a sinusoidal input current [51]. Hence, a current-driven rectifier must be used. Two different rectifiers are considered: bridge and half-wave (Fig. 4.15).

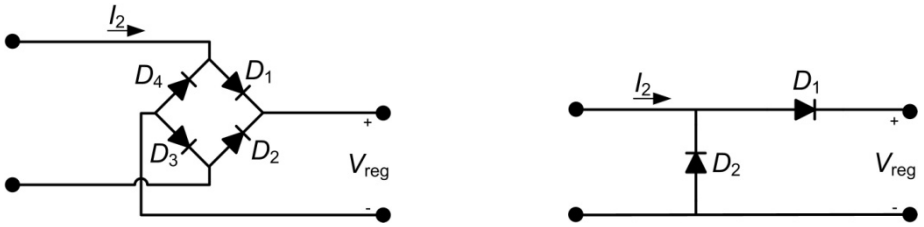

Fig. 4.15 Current-driven rectifiers: Bridge (left) and half-wave (right).

These rectifiers allow the continuous charge of the filter capacitor C_r (Fig. 4.12). In steady-state, the electrical charge injected to C_r through the rectifier must equal that provided to the ensuing stage, the voltage regulator. Thus,

$$I_2 = \frac{I_{\text{reg}}}{\sqrt{F}} \tag{4.48}$$

where I_2 is the rms value and

$$F = \begin{cases} \dfrac{8}{\pi^2} & \text{for the bridge rectifier} \\ \dfrac{2}{\pi^2} & \text{for the half-wave rectifier} \end{cases} \tag{4.49}$$

The equivalent P_{Load} can be expressed as

$$P_{\text{Load}} = I_2^2 R_{\text{Load}} \tag{4.50}$$

and also as

$$P_{\text{Load}} = P_{\text{D}} + P_{\text{reg}} \tag{4.51}$$

where in both rectifiers

$$P_{\text{D}} = 2V_{\text{D}} I_{\text{reg}} \tag{4.52}$$

is the power dissipated by the rectifier, being V_{D} the voltage drop of one diode (assumed constant), and

$$P_{\text{reg}} = I_{\text{reg}}^2 R_{\text{reg}} \tag{4.53}$$

is the power dissipated by the regulator plus that consumed by the autonomous sensor. Thus, equating (4.50) with (4.51) and operating with some of the remaining expressions from (4.46) to (4.53), we get

$$R_{\text{Load}} = F\left(1 + \frac{2V_{\text{D}}}{V_{\text{reg}}}\right) R_{\text{reg}} \tag{4.54}$$

Where the equivalency only applies to the amount of power drawn from the secondary resonant tank [51].

To find out the value of V_{reg} we start from

$$P_{\text{Load}} = V_{\text{Load}} I_2 = \left(2V_{\text{D}} + V_{\text{reg}}\right) I_{\text{reg}} \tag{4.55}$$

Then, substituting (4.48) in (4.55) we obtain

$$V_{\text{Load}} = \sqrt{F}\left(2V_{\text{D}} + V_{\text{reg}}\right) \tag{4.56}$$

From the circuit of Fig. 4.13, we obtain

$$V_{\text{Load}} = V_{\text{T}} - I_2 R_{\text{T}} \tag{4.57}$$

Thus, equating (4.56) to (4.57) and operating we get

$$V_{\text{reg}} = V_{\text{eq}} - I_{\text{reg}} R_{\text{eq}} \tag{4.58}$$

where

$$V_{\mathrm{eq}} = \frac{V_{\mathrm{T}}}{\sqrt{F}} - 2V_{\mathrm{D}}$$
$$R_{\mathrm{eq}} = \frac{R_{\mathrm{T}}}{F} \tag{4.59}$$

So, the equivalent circuit of Fig. 4.13 can be drawn as

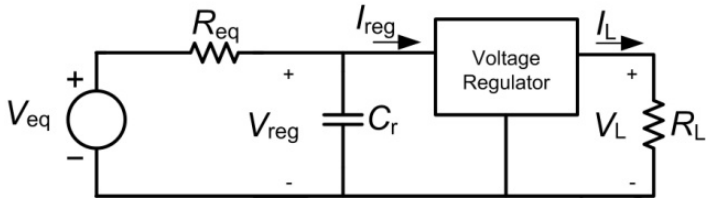

Fig. 4.16 Equivalent circuit of the secondary network.

For $V_{\mathrm{reg}} = V_{\mathrm{eq}}/2$ we get the maximum value of P_{reg}, which is

$$P_{\mathrm{reg,max}} = \frac{V_{\mathrm{eq}}^2}{4R_{\mathrm{eq}}} \tag{4.60}$$

4.6.3 Voltage Regulation

We will consider four types of voltage regulators,: linear shunt and series regulators, and the inductor-based switching buck and boost regulators. Below, we analyze the performance of these four regulators. In particular, we calculate the equivalent R_{reg} and P_{Load} for each case as well as V_{reg}. As for P_{Load}, we obtain expressions in function of R_{Load}, which combined with (4.18) will lead to the determination of the operating point (P_{Load}, R_{Load}).

4.6.3.1 Linear Shunt Regulator

The linear shunt voltage regulator is disposed just across the power supply rail (V_{L}) of the autonomous sensor (R_{L}). In this case, $V_{\mathrm{L}} = V_{\mathrm{reg}}$. Whenever V_{reg} in Fig. 4.16 is lower than the shunt voltage (V_{Z}), the shunt regulator acts as an open circuit. Thus, $R_{\mathrm{reg}} = R_{\mathrm{L}}$. Otherwise, it acts as a constant voltage load by clamping the voltage V_{reg} (=V_{L}) to V_{Z}. Thus, the circuit of Fig. 4.16 can be transformed in the equivalent circuit of Fig. 4.17.

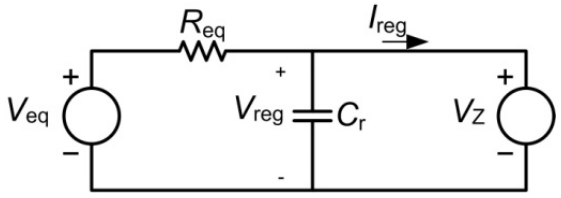

Fig. 4.17 Equivalent circuit of the secondary network with a linear shunt regulator.

As $I_{\mathrm{reg}} \geq I_{\mathrm{L}}$, from (4.58), it must be accomplished

$$V_{\mathrm{eq}} \geq V_{\mathrm{Z}} + I_{\mathrm{L}} R_{\mathrm{eq}} \tag{4.61}$$

Further, $R_{\mathrm{reg}} = R_{\mathrm{L}} \| R_{\mathrm{Z}}$, where R_{Z} is the equivalent resistance offered by the shunt regulator. Thus, as $R_{\mathrm{reg}} \leq R_{\mathrm{L}}$, from (4.54) we find the maximum value of R_{Load} as

$$R_{\mathrm{Load,max}} = F\left(1 + \frac{2V_{\mathrm{D}}}{V_{\mathrm{L}}}\right) R_{\mathrm{L}} \tag{4.62}$$

where we assume that $V_{\mathrm{L}} = V_{\mathrm{Z}}$ and V_{D} and V_{Z} are known parameters. On the other hand, from (4.50) we get

$$I_2 = \sqrt{\frac{P_{\mathrm{Load}}}{R_{\mathrm{Load}}}} \tag{4.63}$$

and substituting (4.63) in (4.48) and the resulting expression of I_{reg} in (4.55), and assuming $V_{\mathrm{reg}} = V_{\mathrm{Z}}$, we obtain

$$P_{\mathrm{Load}} = F \frac{(2V_{\mathrm{D}} + V_{\mathrm{Z}})^2}{R_{\mathrm{Load}}} \tag{4.64}$$

Fig. 4.18 shows a parameterized graph of (4.64).

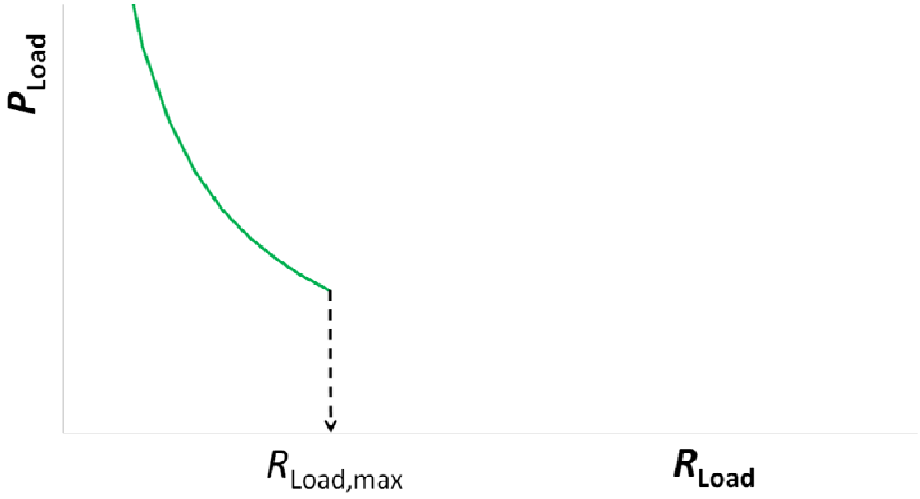

Fig. 4.18 P_{Load} vs R_{Load} for the linear shunt regulator.

4.6.3.2 Linear Series Regulator

A linear series regulator fixes a desired output voltage V_{L} requiring at the same time $V_{\mathrm{reg}} \geq V_{\mathrm{L}}$. On the other hand, involved currents are related by

$$I_{\mathrm{reg}} = I_{\mathrm{L}} + I_{\mathrm{leak}} \tag{4.65}$$

where I_{leak} is the leakage current of the series regulator and I_L is given by (4.45). Thus, assuming I_{leak} as a constant, the voltage regulator acts as a constant current load and the circuit of Fig. 4.16 can be transformed in the equivalent circuit of Fig. 4.19.

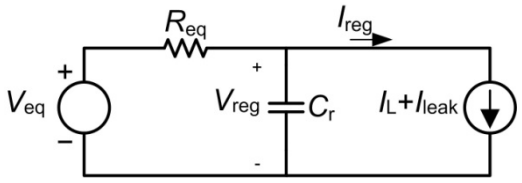

Fig. 4.19 Equivalent circuit of the secondary network with a linear series regulator.

From (4.58) and (4.65) we obtain the operating point of V_{reg} as

$$V_{\mathrm{reg}} = V_{\mathrm{eq}} - (I_{\mathrm{L}} + I_{\mathrm{leak}})R_{\mathrm{eq}} \tag{4.66}$$

and as it is required that $V_{reg} \geq V_L$, it must be accomplished that

$$V_{\mathrm{eq}} \geq V_{\mathrm{L}} + (I_{\mathrm{L}} + I_{\mathrm{leak}})R_{\mathrm{eq}} \tag{4.67}$$

On the other hand, operating from (4.45), (4.46) and (4.65) we get

$$R_{\mathrm{reg}} = \frac{V_{\mathrm{reg}}}{V_{\mathrm{L}}} \frac{1}{1 + \frac{I_{\mathrm{leak}}}{I_{\mathrm{L}}}} R_{\mathrm{L}} \tag{4.68}$$

The minimum value of R_{reg} will be found at $V_{reg} = V_L$. Then, from (4.54) we obtain the minimum value of R_{Load},

$$R_{\mathrm{Load,min}} = F\left(1 + \frac{2V_{\mathrm{D}}}{V_{\mathrm{L}}}\right) \frac{1}{1 + \frac{I_{\mathrm{leak}}}{I_{\mathrm{L}}}} R_{\mathrm{L}} \tag{4.69}$$

On the other hand, by substituting (4.65) in (4.48) and the resulting expression in (4.50), P_{Load} can be expressed as

$$P_{\mathrm{Load}} = \frac{(I_L + I_{\mathrm{leak}})^2}{F} R_{\mathrm{Load}} \tag{4.70}$$

Fig. 4.20 shows a parameterized graph of (4.70).

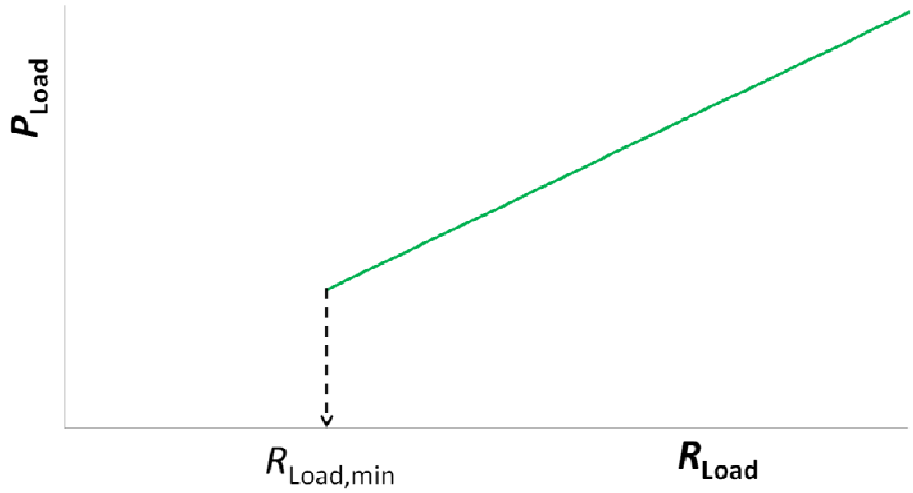

Fig. 4.20 P_{Load} vs R_{Load} for linear series regulator.

4.6.3.3 Switching Regulators

The same as the linear series regulator, a switching regulator fixes a desired output voltage V_L and requires $V_{reg} \geq V_L$ for a buck type and $V_{reg} \leq V_L$ for a boost type. On the other hand, the input and output power of the switching regulators are related by

$$P_L = \eta P_{reg} \tag{4.71}$$

where η is the efficiency of the regulator. Efficiencies higher than 90 % are easily achieved with commercial devices. Assuming η as a constant, a switching regulator behaves as a constant power load and the circuit of Fig. 4.16 can be transformed in the equivalent circuit of Fig. 4.21.

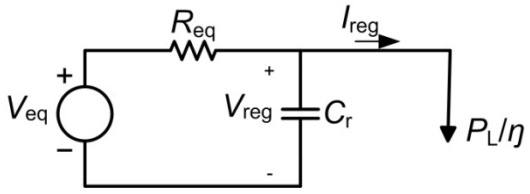

Fig. 4.21 Equivalent circuit of the secondary network with a switching regulator.

From (4.58) and (4.71) we obtain

$$V_{reg} = V_{eq} - \frac{P_L}{\eta V_{reg}} R_{eq} \tag{4.72}$$

Operating from (4.72), two solutions of V_{reg} are attained, which are

$$V_{reg} = \frac{V_{eq}}{2} \pm \frac{\sqrt{V_{eq}^2 - 4\frac{P_L}{\eta} R_{eq}}}{2} \tag{4.73}$$

In order to have real values, we must accomplish

$$P_{\mathrm{reg,max}} \geq \frac{P_{\mathrm{L}}}{\eta} \tag{4.74}$$

where $P_{\mathrm{reg,max}}$ was defined in (4.60).

On the other hand, operating from (4.45), (4.46) and (4.71) we get

$$R_{\mathrm{reg}} = \left(\frac{V_{\mathrm{reg}}}{V_{\mathrm{L}}}\right)^2 \eta R_{\mathrm{L}} \tag{4.75}$$

Now, the minimum a maximum values of R_{reg} will be achieved at $V_{\mathrm{reg}} = V_{\mathrm{L}}$ for the buck and boost converter types, respectively. Then, from (4.54) we obtain the respective values of R_{Load} as

$$R_{\mathrm{Load,min/max}} = F\left(1 + \frac{2V_{\mathrm{D}}}{V_{\mathrm{L}}}\right)\eta R_{\mathrm{L}} \tag{4.76}$$

On the other hand, by using (4.52) and (4.71) in (4.51), P_{Load} can be expressed as

$$P_{\mathrm{Load}} = \frac{P_{\mathrm{L}}}{\eta} + 2V_{\mathrm{D}} I_{\mathrm{reg}} \tag{4.77}$$

and substituting (4.48) in (4.63) and the result in (4.77) we get

$$P_{\mathrm{Load}} = \frac{P_{\mathrm{L}}}{\eta} + 2V_{\mathrm{D}}\sqrt{F\frac{P_{\mathrm{Load}}}{R_{\mathrm{Load}}}} \tag{4.78}$$

Further processing we obtain

$$P_{\mathrm{Load}} = \frac{P_{\mathrm{L}}}{\eta} + \frac{2V_{\mathrm{D}}\left(V_{\mathrm{D}}F \pm \sqrt{(V_{\mathrm{D}}F)^2 + R_{\mathrm{Load}}\frac{P_{\mathrm{L}}}{\eta}F}\right)}{R_{\mathrm{Load}}} \tag{4.79}$$

where only the solution with the highest value out of the two possible ones is valid. The other solution provides a value smaller than P_{L}/η, and thus of P_{reg}. Fig. 4.22 shows a parameterized graph of (4.79) for the solution with the highest value of P_{Load}.

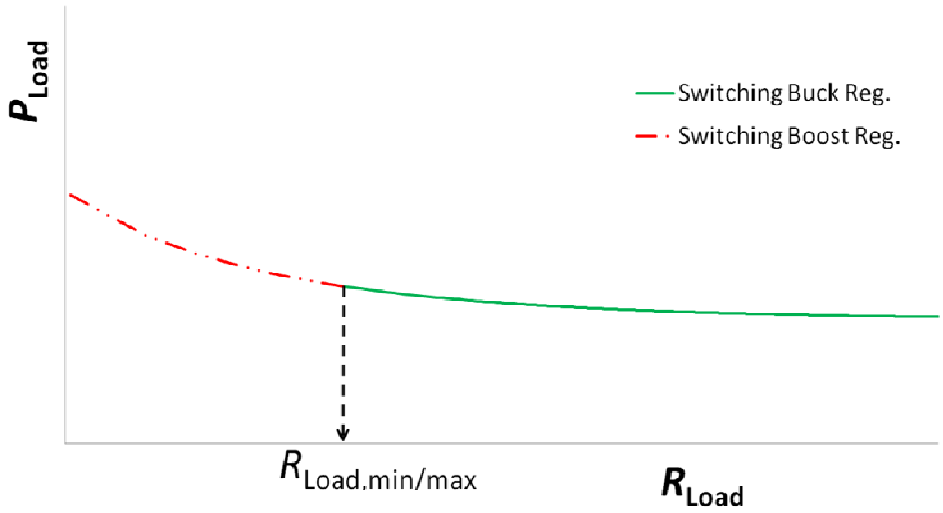

Fig. 4.22 P_{Load} vs R_{Load} for the switching regulators.

4.6.4 Operating Points and Stability

Operating points of (P_{Load}, R_{Load}) for each one of the reported regulators can be found by using (4.64), (4.70), and (4.79) in (4.18). Another option is to find the respective values of V_{reg} as has been reported in 4.6.3 and then operate to obtain the rest of parameters of interest. Fig. 4.23 shows a generic graph of P_{Load} versus R_{Load} for (4.18) and for the four types of voltage regulators. As can be seen, one operating point exists for each one of them. Later, in section 4.7, we will compute the operating points for several distances and combinations of coils

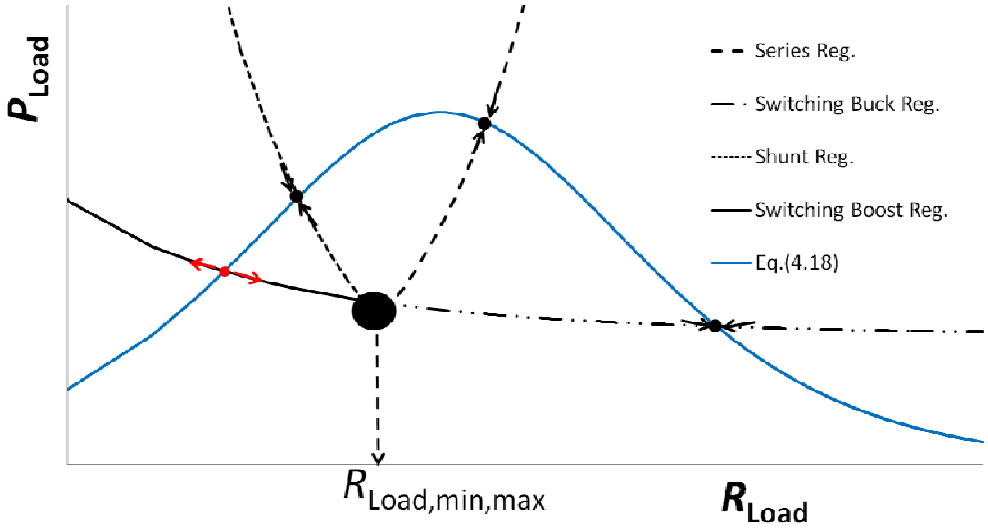

Fig. 4.23 Operating points of the voltage regulators.

A stability analysis can be performed considering the dynamics of the system. To do so, the filter capacitor C_r placed at the input of the voltage regulator is considered in the analysis. From Fig. 4.17 and Fig. 4.19, it is evident that linear regulators are stable. However, this is not the case for switching regulators. From the circuit of Fig. 4.21, we obtain

$$\frac{V_{\mathrm{eq}}-V_{\mathrm{reg}}}{R_{\mathrm{eq}}}=\frac{P_{\mathrm{L}}}{\eta V_{\mathrm{reg}}}+C_{\mathrm{r}}\frac{dV_{\mathrm{reg}}}{dt} \tag{4.80}$$

which can be rearranged as

$$C_{\mathrm{r}}\frac{dV_{\mathrm{reg}}}{dt}+\frac{V_{\mathrm{reg}}}{R_{\mathrm{eq}}}+\frac{P_{\mathrm{L}}R_{\mathrm{eq}}}{\eta V_{\mathrm{reg}}}-\frac{V_{\mathrm{eq}}}{R_{\mathrm{eq}}}=0 \tag{4.81}$$

Then, we use a first-order Taylor expansion

$$\frac{1}{V_{\mathrm{reg}}}\approx\frac{1}{V_{\mathrm{reg0}}}-\frac{1}{V_{\mathrm{reg0}}^2}\left(V_{\mathrm{reg}}-V_{\mathrm{reg0}}\right) \tag{4.82}$$

around a particular value V_{reg0} and substitute it in (4.81). Thus, we obtain the following differential equation

$$C_{\mathrm{r}}\frac{dV_{\mathrm{reg}}}{dt}+V_{\mathrm{reg}}\left(\frac{1}{R_{\mathrm{eq}}}-\frac{P_{\mathrm{L}}}{\eta V_{\mathrm{reg0}}^2}\right)+\frac{2P_{\mathrm{L}}}{\eta V_{\mathrm{reg0}}}-\frac{V_{\mathrm{eq}}}{R_{\mathrm{eq}}}=0 \tag{4.83}$$

A positive value of the term that multiplies to V_{reg} leads to a stable solution whereas a negative value leads to an unstable solution. Substituting the expression of (4.72) for $V_{\mathrm{reg}} = V_{\mathrm{reg0}}$ in that term, we obtain

$$\frac{1}{R_{\mathrm{eq}}}-\frac{P_{\mathrm{L}}}{\eta V_{\mathrm{reg0}}^2}=\frac{2V_{\mathrm{reg0}}-V_{\mathrm{eq}}}{V_{\mathrm{reg0}}R_{\mathrm{eq}}} \tag{4.84}$$

which is positive for $V_{\mathrm{reg0}} \geq V_{\mathrm{eq}}/2$ and negative for $V_{\mathrm{reg0}} \leq V_{\mathrm{eq}}/2$. Thus, whenever (4.74) holds, the solution with the highest value of (4.73) leads to a stable solution whereas the lowest value leads to an unstable solution. A higher value of V_{reg} means a higher value of R_{reg} and thus of R_{Load}. Thus, for switching converters, the operating point out of the two resulting ones, with the highest value of R_{Load} will be stable whereas the point with the lowest value of R_{Load} will be unstable. In the example of Fig. 4.23, the arrows pointing towards and outwards the operating point respectively indicate an stable and unstable operating point. As can be seen, in this example the buck converter has a stable operating point whereas the boost converter does not.

4.6.5 Efficiencies

The rectifier and voltage regulation stages introduce losses and thus reduce the overall efficiency. The efficiency of the rectifier stage is given by

$$\eta_{\mathrm{R}} = \frac{P_{\mathrm{reg}}}{P_{\mathrm{Load}}} \tag{4.85}$$

which, further processing, can be expressed as

$$\eta_{\mathrm{R}} = \frac{1}{1 + \frac{2V_{\mathrm{D}}}{V_{\mathrm{reg}}}} \tag{4.86}$$

For the shunt regulators $V_{reg} = V_Z$ and thus (4.86) is a constant. The efficiency of the voltage regulation stage is given by

$$\eta_{\mathrm{reg}} = \frac{P_{\mathrm{L}}}{P_{\mathrm{reg}}} \tag{4.87}$$

Thus, the overall efficiency from the power source to the autonomous sensor can be expressed as

$$\eta_{\mathrm{T}} = \eta_{\mathrm{Load}}\eta_{\mathrm{R}}\eta_{\mathrm{reg}} \tag{4.88}$$

which can also be written as

$$\eta_{\mathrm{T}} = \frac{P_{\mathrm{L}}}{P_{\mathrm{g}}} \tag{4.89}$$

where P_g refers to the generated power by the power source and is given by

$$P_{\mathrm{g}} = \frac{V_1^2}{R_1 + R_{\mathrm{r}}} \tag{4.90}$$

Thus, substituting (4.90) in (4.89), we get

$$\eta_{\mathrm{T}} = \frac{P_{\mathrm{L}}}{V_1^2}(R_1 + R_r) \tag{4.91}$$

For a given configuration of coils, R_{L1} and R_{L2} are fixed. Thus, R_1 is fixed. Then as P_L and V_1 are fixed, a higher value of R_r will lead, from (4.91), to a higher value of η_T. Shorter distances between the coupled coils lead to higher values of k and thus, from (4.19), to higher values of R_r. At a given distance, lower values of R_{Load} will lead, again from (4.19) to higher values of R_r. Thus, in Fig. 4.23, and considering only the stable operating points, the shunt regulator will provide the maximum overall efficiency whereas the buck switching regulator will provide the minimum overall efficiency. This result appears at first as counterintuitive since switching

regulators have, in general, higher efficiencies (η_{reg}). However, in the example of Fig. 4.23, the working point of the buck regulator leads to a high value of R_{Load} which in turn translates to a low value of R_r and thus to a lower η_T. Contrariwise, higher values of R_{Load} lead to higher efficiencies of η_2 and η_R, which combined with the high efficiency (η_{reg}) of switching regulators, leads to lower power dissipation at the secondary network. That can be beneficial in some applications such as biomedical implants, where heat dissipation into the body should be minimized [51].

4.6.6 Batteries

An alternative to increase the overall efficiency is to use rechargeable (or secondary) batteries after the rectifier stage. The filter capacitor C_r can still be left in order to support the battery for power pulse demands from the autonomous sensor. Batteries act in a similar way to linear shunt regulators as they clamp V_{reg} to the battery voltage V_B. As just commented, shunt regulators provide the highest efficiency. In addition, the excess of energy is not wasted through the regulator but accumulated into the battery. Obviously, protecting devices for avoiding the overcharge and overdischarge of the battery should be added. An ensuing voltage regulator can still be placed after the battery. Special attention must be paid, though, to some regulations that affect batteries such as [85].

A simple battery electrical model is shown in Fig. 4.24, where V_B models the open-circuit voltage and R_B is the series equivalent resistance.

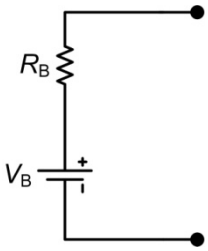

Fig. 4.24 Electrical model of a battery.

Fig. 4.25 shows a generic graph of P_{Load} versus R_{Load} when using a battery. P_{Load} for the battery case can be obtained from (4.64) with the change of V_Z by V_B. As a first approximation, we assume a neglectable battery resistance (R_B) and avoid the use of voltage regulators. As can be seen, with the use of the battery we save the power dissipated in the regulator, which now is gathered into the battery. Now, the overall efficiency is given by

$$\eta_T = \eta_{Load}\eta_R \tag{4.92}$$

In this case, as $V_{reg} = V_B$, (4.87) can be expressed as

$$\eta_{\mathrm{R}} = \frac{1}{1 + \frac{2V_{\mathrm{D}}}{V_{\mathrm{B}}}} \tag{4.93}$$

which the same as with the shunt regulator is a constant term whenever V_{D} and V_{B} are assumed constants. Thus, the value of R_{Load} that provides the maximum value of η_{T} will match with that of η_{Load}, i.e. that given by (4.38) and represented in Fig. 4.7.

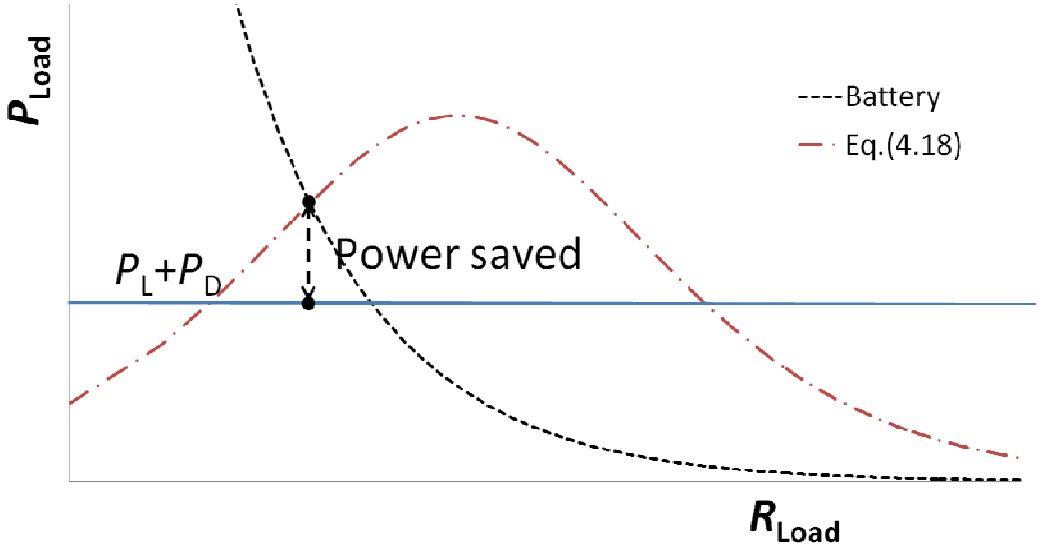

Fig. 4.25 P_{Load} vs R_{Load} for the battery. The power wasted with the regulators is now saved into the battery.

As the power received at the battery can be higher than P_{L}, the transfer of power can be discontinuous. The same autonomous sensor can report when the battery is fully charged in order to stop the transmission of power. In the same way, power transmission can be reactivated whenever the battery is almost depleted.

Whenever a voltage regulator is added between the battery and the autonomous sensor, efficiency η_{Reg} has to be considered. Now, switching regulators do not cause stability problems as the dynamics is dictated by the battery. Thus, by choosing a switching regulator, η_{Reg} can be rather high. On the other hand, for battery voltages close to (and higher than) V_{L}, linear regulators can be a good option.

4.7 Graphs and Analytical Computations

In order to obtain graphs of P_{Load} versus R_{Load}, we carried out computations of (4.18) for d = 0.5 cm to d = 3 cm and of (4.64), (4.70) and (4.79) . We used different combinations of coils and two resonant frequencies: 40 kHz and 120 kHz. The parameter values used for the computations are shown in Table 4.3, some of which have been previously reported. The values of k were taken from the simulations of the ferrite-core coils presented in Fig. 3.14; resistance

values of the coils were taken from Fig. 4.9; R_1 was found as the addition of R_s and R_{L1}, where a value of 1 Ω was considered for R_s. The values of V_D, I_{leak} and η were based on the manufacturer datasheets of the components used for the experimental setup (section 4.8), and the values of V_Z and V_L were assumed as 3 V.

Table 4.3 Values of the parameters used for computations.

Parameters		Case 1	Case 2	Case 3	Case 4	Case 5
f_r		40 kHz			120 kHz	
V_1		5.4 V				
k @ d=0.5, 1, 1.5, 2, 2.5, 3 cm		0.125, 0.061, 0.033, 0.019, 0.012, 0.009				
Coil inductance	L_1	1 mH		10 mH	1 mH	
	L_2	1 mH	10 mH	1 mH		10 mH
Coil resistance	R_{L1}	6.45 Ω		44 Ω	22 Ω	
	R_{L2}	6.45 Ω	44 Ω	6.45 Ω	22 Ω	117 Ω
R_1		7.45 Ω		45 Ω	23 Ω	
V_D, V_Z, V_L		0.4 V, 3 V, 3 V				
I_{leak} (lineal series)		500 μA				
η (switching buck)		0.90				

The five cases in Table 4.3 were computed for both the current-driven bridge and half-wave rectifiers. The following figures, from Fig. 4.26 to Fig. 4.30, show the five cases with the bridge rectifier. In them, (4.18) is represented for different distances as well as (4.64), (4.70), and (4.79). The curves corresponding to (4.64), (4.70), and (4.79) are represented from the corresponding limiting values of R_{Load}, which were found from (4.62), (4.69) and (4.76), respectively. The respective values of R_{Load} are 102.7 Ω, 100.9 Ω and 92.4 Ω. And the respective power values of P_{Load} are 113.9 mW, 115 mW and 126.5 mW.

Fig. 4.26 shows the results for case 1 in Table 4.3. Only the stable operating points are marked with symbols. Linear shunt and series regulators as well as the buck regulator provide three operating points at the distances from d = 0.5 cm to d = 1.5 cm. As can be seen, the shunt regulator provides the lowest values of R_{Load} at all that distances and thus the highest values of η_T, whereas the buck regulator provides the highest values of R_{Load} and thus the lowest values of η_T. The same happens in the rest of cases, as will be seen. On the other hand, the switching boost regulator only provides one stable operating point at d = 2 cm.

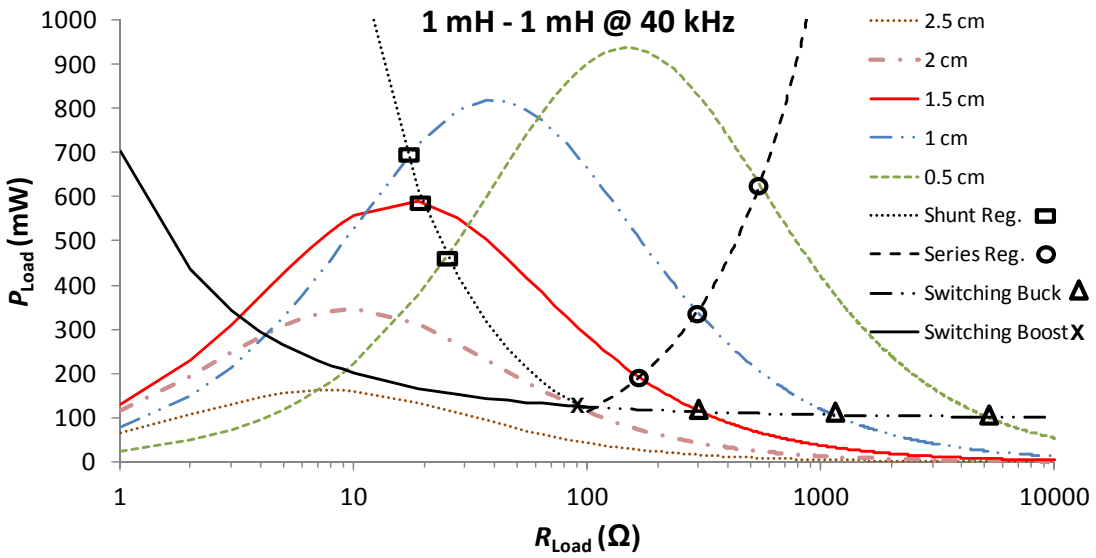

Fig. 4.26 P_{Load} vs R_{Load} for the four types of regulators at different distances (case 1, bridge rectifier).

Fig. 4.27 shows case 2 in Table 4.3. With respect to case 1, L_2 increases from 1 mH to 10 mH. This leads to a higher value of Q_{L2} (see Fig. 4.10) and, from (4.34), to a higher value of $P_{Load,max.}$, specially at the largest distances. R_{L2} also increases (see Fig. 4.9 and Table 4.3) and so does, from (4.35), $R_{Load,optP}$. Overall, more operating points are achieved for the linear and switching buck regulators, from d = 0.5 cm to d = 2.5 cm. The switching boost regulator only provides a stable operating point at d = 3 cm.

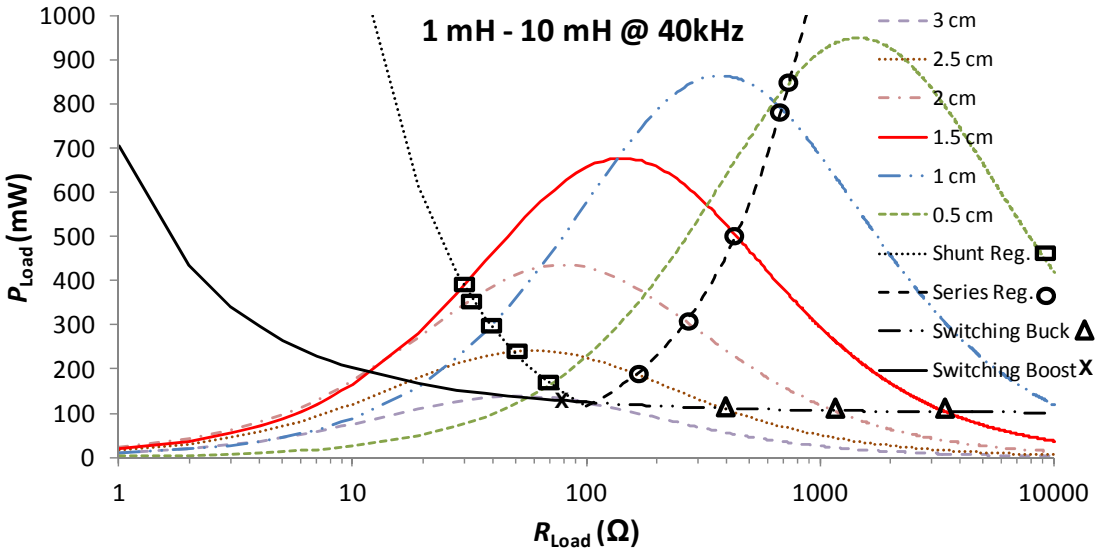

Fig. 4.27 P_{Load} vs R_{Load} for the four types of regulators at different distances (case 2, bridge rectifier).

Fig. 4.28 shows case 3 in Table 4.3. With respect to case 1, L_1 increases from 1 mH to 10 mH. This leads to an increase of Q_{L1} but to a large increase of R_{L1} and thus of R_1. Overall, from

(4.34), a large decrease of $P_{\text{Load,max}}$ is observed. From (4.35), $R_{\text{Load,optP}}$ slightly increases because of the increase of Q_{L1}. Now, only two operating points are provided by the linear and buck regulators at d = 0.5 cm and d = 1 cm. No operating point is found for the boost regulator.

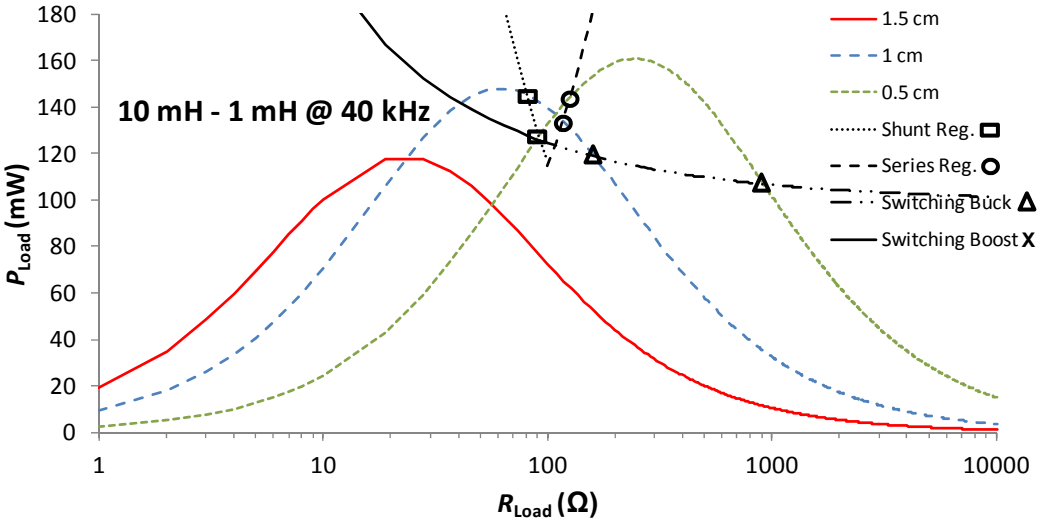

Fig. 4.28 P_{Load} vs R_{Load} for the four types of regulators at different distances (case 3, bridge rectifier).

Fig. 4.29 shows case 4 in Table 4.3. With respect to case 1, the resonance frequency is increased from 40 kHz to 120 kHz. An increase of frequency leads to an increase of the coil resistances and to a decrease of the quality factors. From (4.34), this means a decrease of $P_{\text{Load,max}}$. The increase of R_{L2} leads, from (4.35), to an increase of $R_{\text{Load,optP}}$. The same as case 1, three operating points are provided by the linear and buck regulators, from d = 0.5 cm to d = 1.5 cm. The switching boost regulator presents no stable working point.

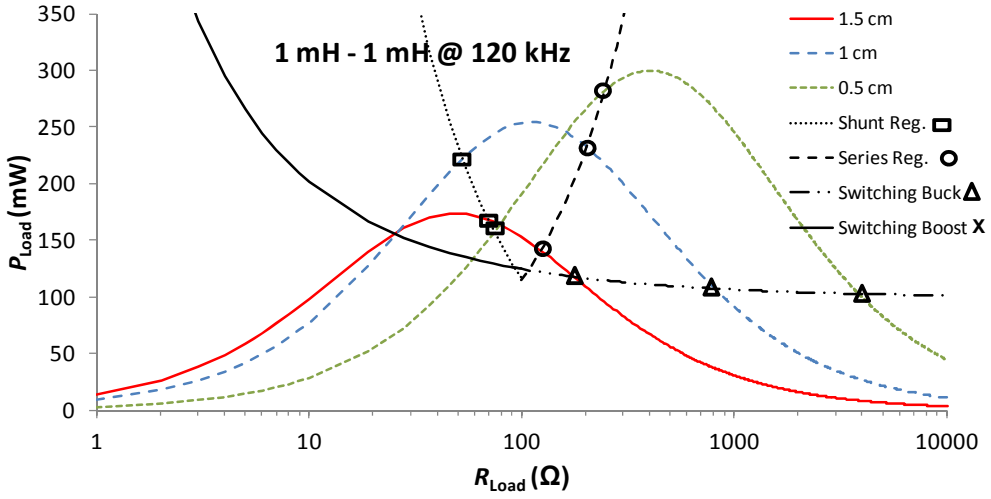

Fig. 4.29 P_{Load} vs R_{Load} for the four types of regulators at different distances (case 4, bridge rectifier).

Fig. 4.30 shows case 5 in Table 4.3. With respect to case 4, L_2 increases from 1 mH to 10 mH. This leads to a large increase of Q_{L2} and, from (4.34), to a higher value of $P_{\text{Load,max}}$,

specially at the largest distances. R_{L2} also increases and so does, from (4.35), $R_{Load,optP}$. With respect to case 2, the resonance frequency is increased from 40 kHz to 120 kHz, which leads to an increase of the coil resistances. As for the coil quality factors, Q_{L1} decreases whereas Q_{L2} increases. Overall, $P_{Load,max}$ decreases. In this case, four operating points are found for the switching buck regulator, from d = 0.5 cm to d = 2 cm, whereas only two are found for the linear regulators, d = 1.5 cm and d = 2 cm. None is obtained for the switching boost regulator.

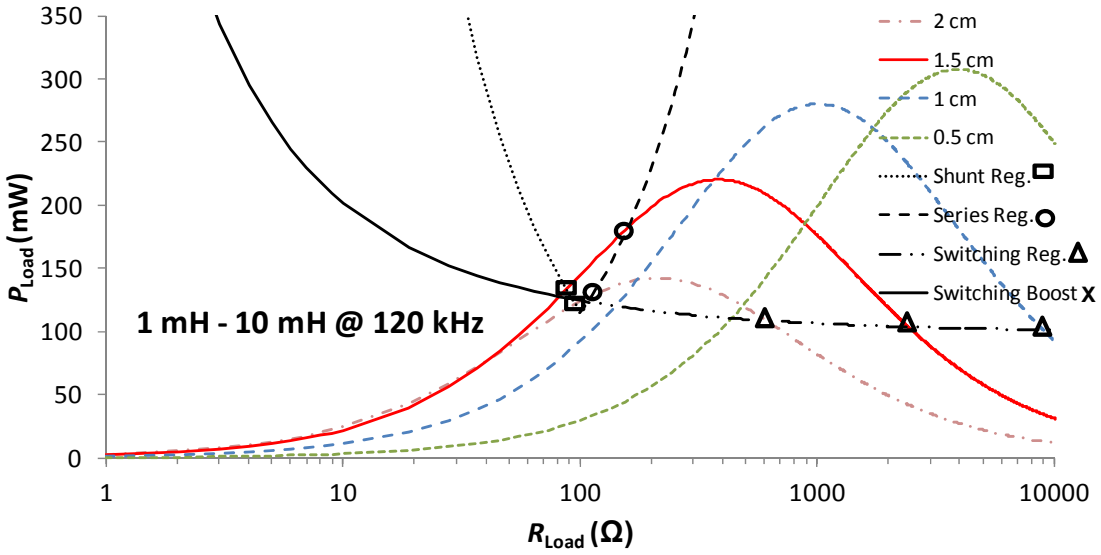

Fig. 4.30 P_{Load} vs R_{Load} for the four types of regulators at different distances (case 5, bridge rectifier).

Appendix C shows the graphs for the five cases in Table 4.3 for the half-wave rectifier. Similar arguments to that described before for the bridge rectifier can be derived.

In order to obtain analytically the operating points (P_{Load}, R_{Load}) we combined (4.64), (4.70) and (4.79) with (4.18) and solve the resulting expression with the program MAPLE. Once calculated R_{Load}, R_r can be obtained from (4.19) and thus η_T from (4.91), where P_L = 90 mW and R_1 is given by Table 4.3.

As an illustrative example, Table 4.4 shows the calculated values of R_{Load} for case 2 (bridge rectifier) and for all the regulator types. Then, R_r, P_g and η_T were inferred from (4.19), (4.90) and (4.91). As can be seen and as previously shown graphically, the shunt regulator provides the minimum values of R_{Load} for all the distances, resulting in the maximum values of η_T, among the regulators. Contrariwise, the switching buck regulator provides the highest values of R_{Load} and thus the minimum values of η_T. On the other hand, power efficiencies decrease at increasing distances. At the shortest represented distance, i.e. 0.5 cm, large differences in η_T are found and range from 30.7 % for the shunt regulator to merely a 2.3 % for the buck converter. This means

that *ca*. 0.3 W have to be sourced (P_g) when using a shunt regulator whereas a buck converter would require *ca*. 3.8 W. At the largest distances, the values of R_r become very small compared to R_1 for all the regulators. Thus, η_T also becomes very small and P_g needs to be very high. The power is mainly wasted at the transmitting network, which creates a power stress in the components. Current and voltages across L_1 and C_1 are also very high. For d = 3 cm, only the boost regulator works but with an efficiency of just 2.3 %. The results when using a battery are also shown. A battery voltage of 3 V, i.e. equal to V_Z of the linear shunt regulator, was assumed. Then, results for R_{Load}, R_r and P_g are the same. However, significantly higher efficiencies are achieved, as stated in section 4.6.6, due to the absence of power losses at the regulator (η_{reg} = 1). The difference in efficiency between the shunt regulator and the battery is directly related to the power gathered by the battery.

Table 4.4 Computed values of R_{Load} and related parameters for case 2 at different distances (Fig. 4.27).

d (cm)	Regulator	R_{Load} (Ω)	R_r (Ω)	P_g (W)	η_T (%)
0.5	Shunt	70.3	92	0.29	31
	Series	738	13	1.4	6.5
	S. Buck	51.8 k	0.21	3.8	2.3
	Battery	70.3	92	0.29	45
1	Shunt	39.3	29	0.8	11
	Series	687	3.4	2.7	3.3
	S. Buck	119 k	0.21	3.8	2.3
	Battery	39.3	29	0.78	30
1.5	Shunt	30.1	9.9	1.7	5.3
	Series	437	1.5	3.2	2.8
	S. Buck	342	0.22	3.8	2.3
	Battery	30.1	9.9	1.7	18
2	Shunt	33.4	3.1	2.8	3.2
	Series	256	0.80	3.5	2.5
	S. Buck	1.02 k	0.23	3.8	2.3
	Battery	33.4	3.1	2.8	10
2.5	Shunt	52.9	0.99	3.5	2.6
	Series	153	0.48	3.7	2.4
	S. Buck	320	0.26	3.8	2.3
	Battery	52.9	0.99	3.5	5.5
3	S. Boost	94.1	0.14	3.8	2.3

In a practical implementation of the IPT system, a zener diode is placed across the input of the linear series and switching regulators in order to protect them from overvoltages. Fig. 4.31 illustrates the resulting behavior in the operating points for case 2 and for a protection zener diode of 10 V. As can be seen, a new curve of P_{Load} corresponding to the protection zener diode is added. This curve is generated from (4.64) with $V_z = 10$ V. In fact, the protection diode acts as a shunt regulator. With reference to Fig. 4.27, the operating points that lie at the right side of the curve corresponding to the protection diode are not possible as the associated voltage V_{reg} is higher than 10 V. In those cases, the intersection of the curve of the protection diode with those corresponding to (4.18) fix the new operating points. In particular, for case 2, new operating points result for the linear series regulator from $d = 0.5$ cm to $d = 1.5$ cm and for the buck regulator from $d = 0.5$ cm to $d = 2$ cm. The new operating points of R_{Load} in Fig. 4.31 are lower with respect to that obtained in Fig. 4.27. Thus, for these operating points higher values of η_T will result.

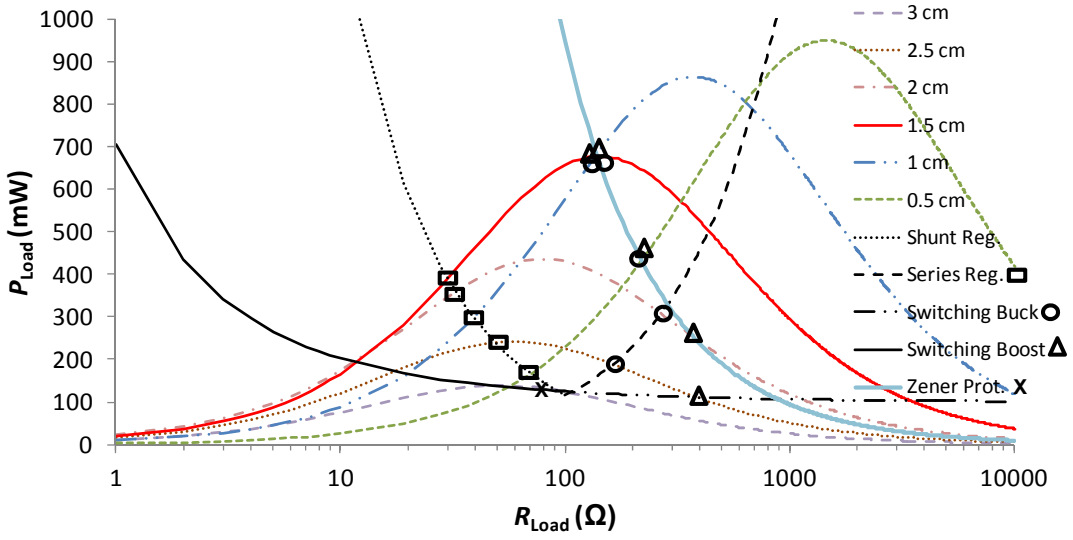

Fig. 4.31 P_{Load} vs R_{Load} for the four types of regulators at different distances (case 2) of Fig. 4.27 with a zener diode as a voltage regulator protector.

Table 4.5 shows the new operating points in Fig. 4.31 with respect to Fig. 4.27. The reduction in the value of R_{Load} implies an increase of R_r and η_T and a decrease of P_g compared to the corresponding values obtained in Table 4.4.

Table 4.5 New Computed values of R_{Load} and associated parameters for case 2 with a zener protection diode of 10 V.

d (cm)	Regulator	R_{Load} (Ω)	R_r (Ω)	P_g (W)	η_T (%)
0.5	Series	219.2	40.0	0.61	0.16
	S. Buck				
1	Series	138.7	13.4	1.4	0.064
	S. Buck				
1.5	Series	139.7	3.99	2.5	0.035
	S. Buck				
2	S.Buck	487.7	0.452	3.6	0.024

Table 4.6 provides the values of η_T for the shunt regulator (left) and for the battery (right) for the five cases proposed in Table 4.3 and for the bridge rectifier. As previously shown, shunt regulators offer the highest overall efficiencies among the different types of regulators. In addition, the use of a rechargeable battery, whenever can be used, offers an improvement on the overall efficiency. As can be seen, case 2 can operate at all the distances and offers a relative high value of η_T at short distances. Case 3 provides the highest value of η_T at d = 0.5 cm but only two operating points, d = 0.5 cm and d = 1 cm, are possible. Case 5 provides relative high efficiencies at long distances but operation at short distances is not possible.

Table 4.6 Computed values of η_T for the shunt regulator (left) and the battery (right) at different distances (bridge rectifier).

d (cm)	Case 1	Case 2	Case 3	Case 4	Case 5
0.5	13 / 52	31 / 45	46 / 51	35 / 48	X
1	5.5 / 33	11 / 30	22 / 27	16 / 30	X
1.5	3.1 / 16	5.3 / 18	X	9.1 / 13	16 / 19
2	X	3.2 / 10	X	X	9.9 / 10
2.5	X	2.6 / 4.9	X	X	X

Table 4.7 shows the computed values of η_T for the half-wave rectifier. At short distances, except for case 1, is not possible to operate. Case 5 offers no operating points. Efficiencies of case 3 at d = 1 cm and 1.5 cm are remarkable.

Table 4.7 Computed values of η_T for the shunt regulator (left) and the battery (right) at different distances (half-wave rectifier).

d (cm)	Case 1	Case 2	Case 3	Case 4	Case 5
0.5	20 / 45	X	X	X	X
1	7.8 / 29	14 / 20	38 / 40	21 / 26	X
1.5	3.4 / 14	6.2 / 12	25 / 25	12 / 15	X
2	2.7 / 7.9	3.6 / 6.7	X	X	X
2.5	2.4 / 2.4	2.8 / 3.9	X	X	X

4.8 Experimental Results

We performed two main experiments: a) the verification of the operating points for case 2 when using the bridge rectifier and b) the calculation of the overall efficiencies when using a shunt regulator or a battery for the cases 3 and 5 (in addition to case 2), which provide the highest efficiencies according to Table 4.6 and Table 4.7.

The mechanical setup presented in Fig. 3.16 was used to fix the distance between the primary and the secondary networks. The circuit of Fig. 4.11 was used for the primary network whereas the circuit of Fig. 4.12 was used for the secondary network. For the rectifiers we used the BAT47 model for the shottky diodes. As for the regulators, we used the following commercial devices in order to achieve a supply voltage (V_L) of 3 V: TL431 (shunt regulator), LP2980 (series regulator), LTC1877 (switching buck regulator) and MAX1795 (switching boost regulator). A protection zener diode of 10 V was placed across the linear series and switching regulators. The supply voltage of 3 V is suitable for most autonomous sensors that include a generic microcontroller and a low-cost transceiver that operates in the free-ISM band. Power consumption in autonomous sensors is dominated by that of the transceiver, with the exception of those that use power hungry sensors. So, a load R_L of 100 Ω was used to emulate a current consumption of 30 mA, which is a typical value for transceivers sending or receiving data.

The procedure to work at the resonance frequency was the following: first, the frequency of the power source was adjusted to the resonant frequency of the primary resonant tank by measuring the voltage drop (measured with a floating oscilloscope) of a resistance inserted between the resonant tank and the MOSFETs of the primary network. In this case, the secondary network was not present and the resonant frequency matched with the maximum in the voltage drop. Then, the secondary network was placed at a distance higher than the computed as d_c in Fig. 4.5 (see Appendix B) and was tuned by adjusting a capacitor trimmer (100 pF), placed in parallel with C_2, in order to achieve a maximum voltage drop in R_{Load}.

As for the verification of the operating points for case 2 when using the bridge rectifier, we used the commercial coils from Fastron with the values 1mH for L_1 and 10 mH for L_2. In order to operate around 40 kHz, we selected capacitors of nominal values C_1 = 15 nF and C_2 = 1.5 nF. Experimental values of R_r were inferred from the measurement of the current through the primary resonant tank. A Hall effect current probe (TEKTRONIX TCPA 300) connected to an oscilloscope was used. Table 4.8 shows the results obtained for R_r. The rest of parameters were computed from R_r. Distances higher than 1.5 cm were not tested as P_g increases too much and lead to an excessive power stress in the components of the primary network. Resulting efficiencies mainly agree with the corresponding computed values of Table 4.4 for the shunt regulator and of Table 4.5 for the series and buck regulators.

Table 4.8 Experimental values of R_r and associated parameters for the three types of regulators at different distances.

d (cm)	Regulator	R_{Load} (Ω)	R_r (Ω)	P_g (W)	η_T (%)
0.5	Shunt	82	84	0.3	28
	Series	233	38	0.6	14
	S. Buck	235	38	0.6	14
1	Shunt	56	25	0.9	9.9
	Series	160	12	1.5	6.0
	S. Buck	158	12	1.5	6.1
1.5	Shunt	46	8.1	1.9	4.8
	Series	153	3.7	2.6	3.5
	S. Buck	159	3.6	2.6	3.4

As for the calculation of the overall efficiencies, we performed tests with the shunt regulator for cases 2, 3 and 5. We used capacitors of nominal values C_1 = 1.5 nF and C_2 = 15 nF for case 3, and C_1 = 1.66 nF and C_2 = 164 pF for case 5. In case 5 we used combination of capacitors. Table 4.9 and Table 4.10 show the results obtained with the bridge and half-wave rectifiers, respectively. The shunt regulator was also used to emulate a battery of 3 V. In this case, apart from estimating the value of R_r from the measurement of current in the primary resonant tank, we also measured the current entering the shunt regulator and the load (I_{reg}) in order to estimate η_T. The results mainly agree with the respective computed values of Table 4.6 and Table 4.7. When using a bridge rectifier, case 3 offers the highest efficiencies at d = 0.5 cm and 1 cm whereas case 5 is the best alternative for d = 1.5 cm and 2 cm. As for the half-wave rectifier, case 3 offers higher efficiencies than those of the bridge rectifier for d = 1 cm and 1.5 cm.

Table 4.9 Experimental values of η_T for the shunt regulator (left) and the battery (right) at different distances and for cases 2, 3, and 5. (Bridge rectifier).

d (cm) / η_T	Case 2	Case 3	Case 5
0.5	28 / 45	51 / 59	X
1	10 / 27	22 / 31	X
1.5	3.7 / 16	X	21 / 21
2	X	X	10 / 10

Table 4.10 Experimental values of η_T for the shunt regulator (left) and the battery (right) at different distances and for cases 2, 3, and 5. (Half-wave rectifier).

d (cm) / η_T	Case 2	Case 3	Case 5
0.5	X	X	X
1	14 / 20	41 / 44	X
1.5	3.5 / 8.8	27 / 32	X
2	X	X	X

Finally, R_L was substituted by the autonomous sensor presented in section 4.6.1. Fig. 4.32 shows the experimental setup with the autonomous sensor (top board) that includes the occupancy and belt detectors. Another ETRX-2 device was connected to the USB port of a PC in order to receive and process the transmitted data. As shown in Appendix B, the autonomous sensor transmitted correctly the data up to a distance of 2.5 cm.

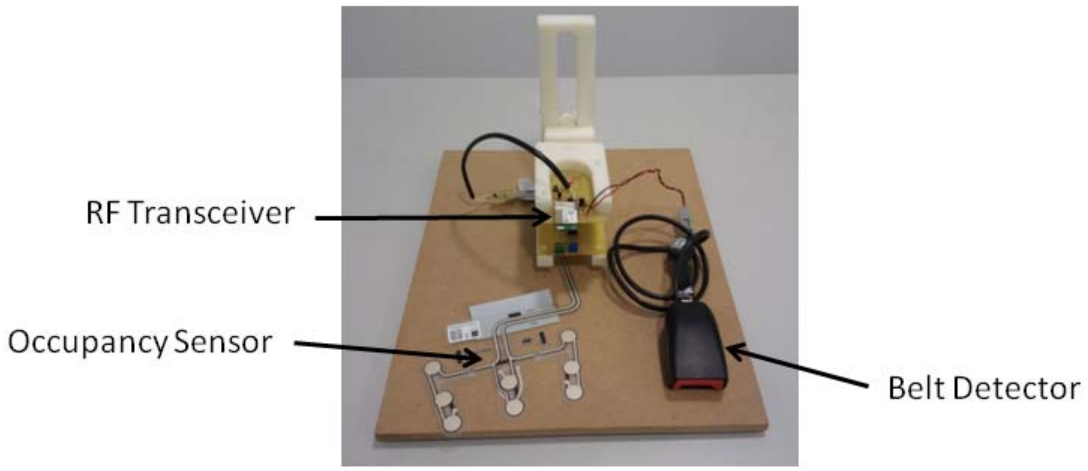

Fig. 4.32 Experimental setup with the autonomous sensor (top board) that includes the occupancy and belt detectors.

Chapter 5 Evaluation of Different Coil Types and Effect of Metallic Structures

In Chapter 3 and Chapter 4 we used commercial ferrite-core coils for the computations and experimental results. Here, we extend those results by using other coils types, both with ferrite- and air-cores. In addition, the effect of metallic structures will be assessed. The presence of metallic or other conductive objects and structures near the coils can induce eddy currents and thus power losses. Thus, metallic objects must be conveniently kept away, whenever the application allows it, such that the magnetic field does not penetrate the metal. When this solution is not allowed, other alternatives should be used. In [86], a low-frequency (50 Hz) system was proposed for power and data transmission through metal walls present in tanks or pipes. Other works get rid of eddy currents by inserting highly permeable materials between the coils and the metallic objects [87]. Magnetic-core coils can thus be suitable in order to avoid eddy currents.

5.1 Effects of Metallic Structures

Metallic materials such as steel are commonly used in the construction of the chassis and body panels of vehicles. As a result, eddy currents can appear in the vicinity of the coils. This effect can be modeled by an additional coupled electric circuit, as shown in Fig. 5.1. As can be seen, the equivalent three-port network is an extension of the two-port network shown in Fig. 2.9 with the resistances of the coils added. The added network is a closed loop containing an inductance L_3 and a resistance R_{L3}.

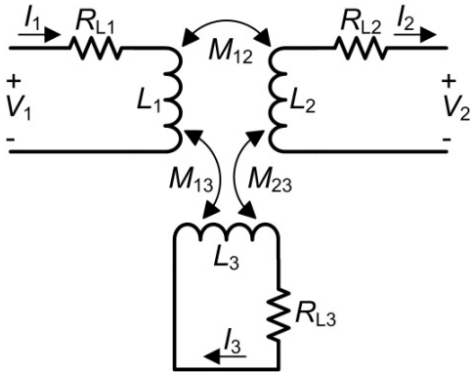

Fig. 5.1 Three-port network used to model the presence of metallic objects in the vicinity of the coils.

Current I_3 in Fig. 5.1 is a function of I_1 and I_2. Thus, the system can be reduced to an equivalent two-port circuit, as shown in Fig. 5.2, with equivalent values of resistance, self-inductance, and mutual inductance given by the following expressions [54].

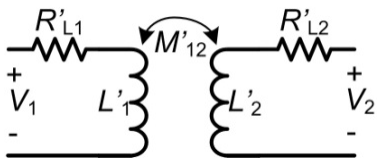

Fig. 5.2 Equivalent two port network of the circuit of Fig. 5.1.

$$R'_{\mathrm{L1,2}} = R_{\mathrm{L1,2}} + \frac{\omega^2 M_{13,23}^2 R_3}{R_3^2 + \omega^2 L_3^2}$$

$$L'_{1,2} = L_{1,2} - \frac{\omega^2 M_{13,23}^2 L_3}{R_3^2 + \omega^2 L_3^2} \tag{5.1}$$

$$M'_{1,2} = M_{1,2} - \frac{M_{13} M_{23}}{R_3^2 + \omega^2 L_3^2}(j\omega R_3 + \omega^2 L_3)$$

With respect to the original two-port network, the values of the new resistances increase whereas the values of the new self-inductances decrease. The resulting mutual inductance is now a complex quantity.

5.2 Selection of Coils

In chapters 3 and 4, commercial ferrite-core coils from Fastron were used. In this chapter, two other types of coils were additionally tested: 1) coils using an ETD-39 core and 2) air-core coils. Fig. 5.3 shows the three types of coils. From left to right we find the commercial Fastron coil, the air-core coil, and the ETD-core coil. Fastron coil uses a rod-type ferrite core. The ETD- and air-core coils were manually wound using a wire with a cross-section diameter of 0.2 mm. In the ETD-core coil wire was wound around the center post. Table 5.1 provides some parameters of the three coils. As can be seen, a similar coil value to that of the Fastron coil (1 mH) was sought for the remaining two coil types. As a result, we had to use a much larger diameter for the air-core type coil with a resulting DC resistance higher than that of the other types. Further, the use of a larger coil is detrimental for the intended application as more space is needed both at the bottom of the seat and within the chassis floor of the vehicle (see Fig. 1.2).

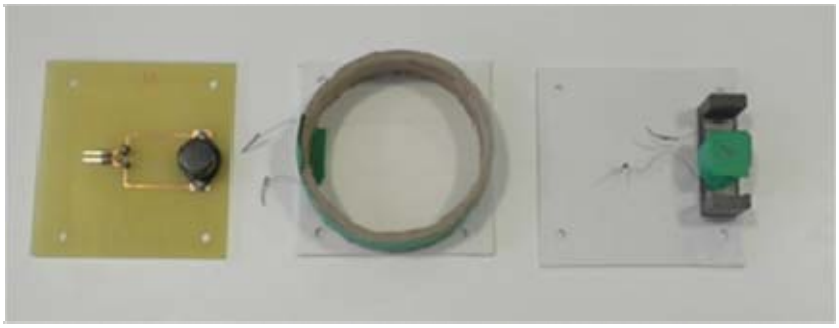

Fig. 5.3 Three different coil types. From left to right: Fastron commercial coil, air-core coil, ETD ferrite-core coil.

Table 5.1 Parameters of the coils.

Coil type	Inner diameter (cm)	Number of turns	Inductance @1 kHz (mH)	Self-resonance (kHz)	DC resistance (Ω)
Fastron	0.6	-	1.03	1180	1.1
ETD	1.2[2]	132	0.91	1474	2.5
Air	6.5	106	1.16	325	12.2

Using the same procedure described in sections 3.4 and 4.4, coil resistances were measured. Fig. 5.4 shows the resistances of the three coils. As can be seen, resistance values increase for increasing frequencies. This increase is due to the skin and proximity effects and, for the magnetic-core coils, also to the core losses. The relative increase of the Fastron coil at high frequencies is more pronounced that for the other two coils.

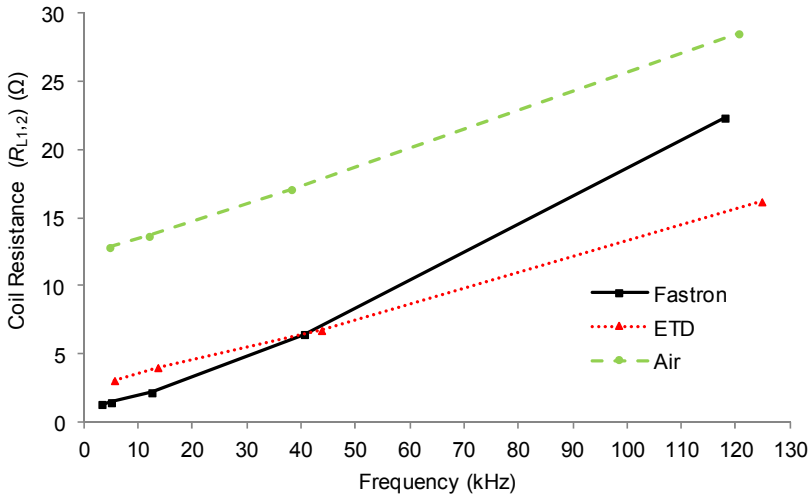

Fig. 5.4 Measured resistances of the coils

[2] Inner radius refers here to the centerpost diameter.

Then, quality factors for the different coils were estimated. Fig. 5.5 shows the resulting values for the tested frequencies. As can be seen, ferrite-core coils offer the highest quality factors. At the highest tested frequency, around 120 kHz, the quality factor of the Fastron coil decreased and approached to that of the air-core coil.

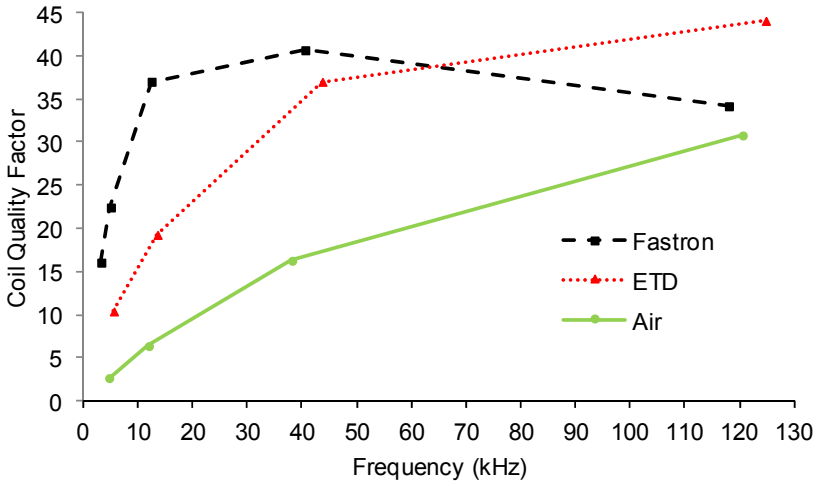

Fig. 5.5 Estimated quality factors of the coils.

A major influence of the metallic structures is expected on the air-core coils whereas minor effects are expected for the magnetic-core coils, in special for the ETD-core type. In order to numerically assess these effects, the COMSOL software introduced in section 2.8 was employed.

Fig. 5.6 shows the axisymmetric models for the three types of coils presented here, where distance between coils (d) is marked. Sizes of the coils (coils 1 and 2) were in accordance with those presented in Table 5.1. The coil cores were defined as ferrite (α-Fe) or air (blank) whereas the coil winding wire was defined as cupper (Cu). A relative permeability (μ_r) of 2000 was used for the ferrite. A metallic plate (0.8 mm thick, 15 cm long) was placed below coil 1. The selected material was iron with a conductivity of $1.12 \cdot 10^7$ S/m and $\mu_r = 4000$.

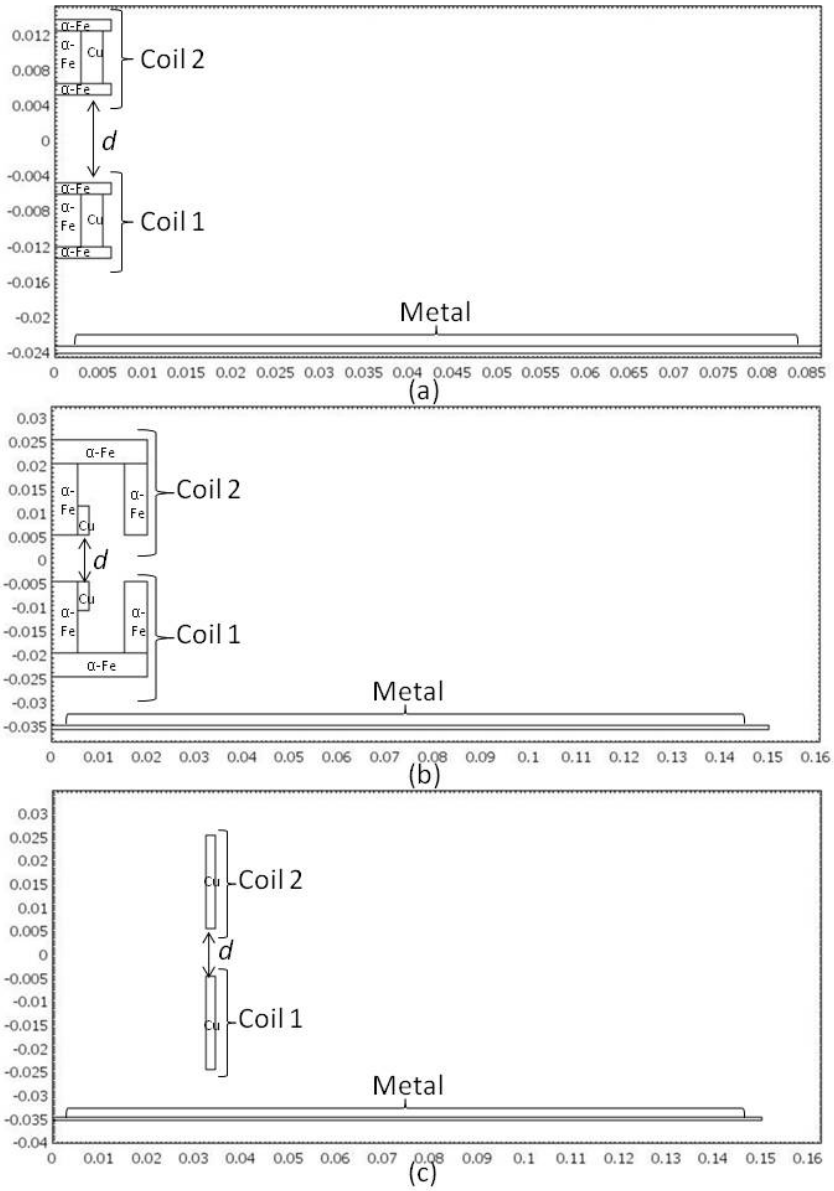

Fig. 5.6 Cross-sectional plot of a pair of coils magnetically coupled in the vicinity of a metal plate using axial axysimmetry with COMSOL Multiphysics. (a) Pair of Fastron coils. (b) Pair of ETD-core coils. (c) Pair of air-core coils.

Fig. 5.7 shows the modulus of the magnetic field (B) resulting from a generated current (0.725 A) in coil 1 for the case of the air-core coils without (a) and with (b) the metallic plate placed at a distance of 1 cm below coil 1. As can be seen, the distribution of the field is greatly affected by the presence of the metallic plate. This will lead to an increase of the resistances values and to a decrease of the coil values in the circuit model of Fig. 5.2. Simulations were performed at a frequency of 120 kHz.

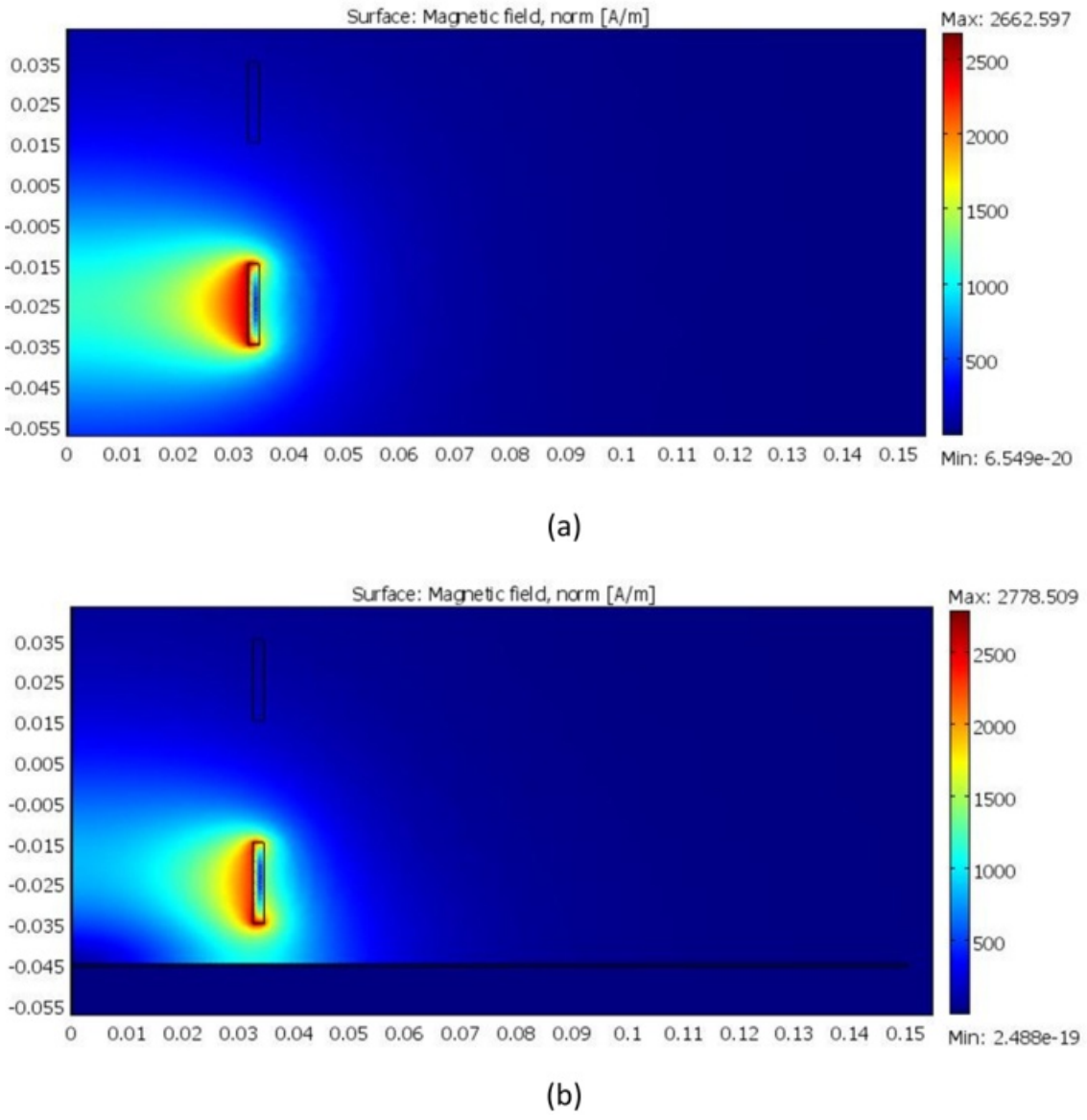

Fig. 5.7 Simulation of the magnetic field normalized resulting from a generated current in coil 1 of 0.725 A for the case of air-core coils without (a) and with (b) the metallic plate placed at 1 cm below coil 1.

The distribution of the magnetic field was unaffected by the presence of the metallic plate when using ferrite-cores, as the magnetic flux is more constrained to the magnetic cores.

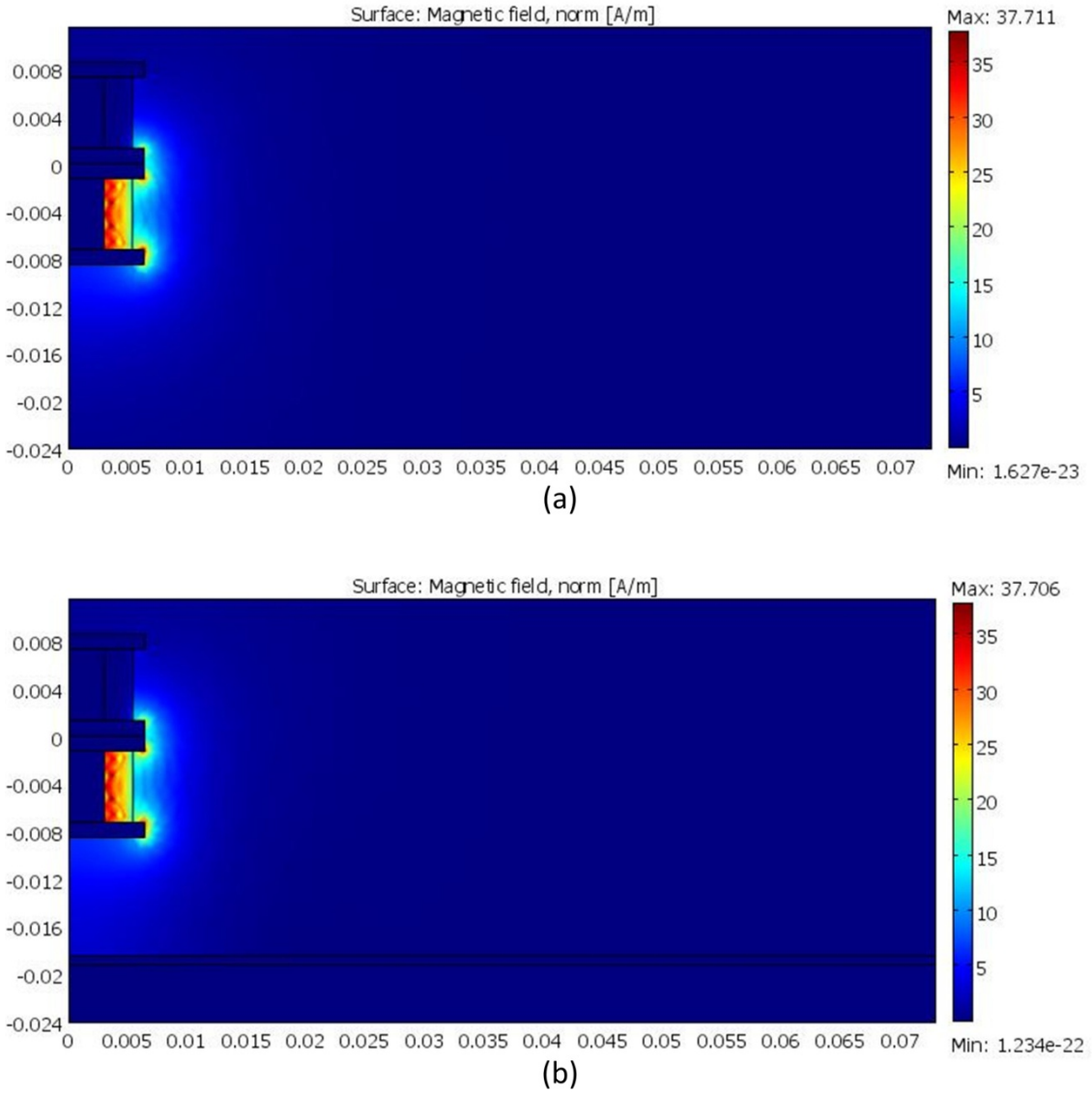

Fig. 5.8 Simulation of the magnetic field normalized resulting from a generated current in coil 1 of 0.725 A for the case of Fastron coils without (a) and with (b) the metallic plate placed at 1 cm below coil 1.

Fig. 5.9 shows simulated values of the self-inductance of the different coil types under the influence of the metallic plate placed at several distances below coil 1 and without the presence of coil 2 in Fig. 5.6. As can be seen, the air-core coil suffers a large decrease at short plate distances. On the other hand, the ETD-core coil is again unaffected by the metallic plate.

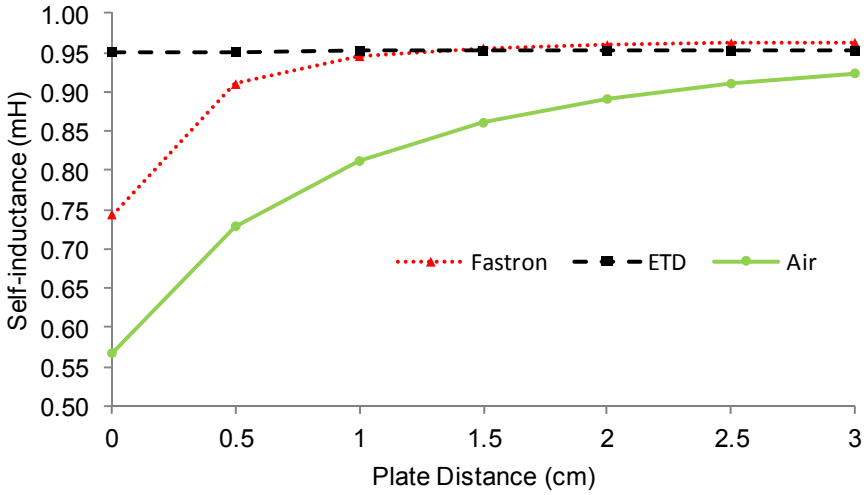

Fig. 5.9 Simulated self-inductance of the different coil types under the influence of a metallic plate placed at several distances.

Contrariwise, the effect of the coupled coil on the self-inductance is higher for ferrite-core coils. The same as Fig. 3.15, we measured with a handheld LCR meter the self-inductance of a coil when approaching a second open-circuit coil. Fig. 5.10 shows measured values of the self-inductances when the coupled coil is at a distance *d*. The ETD-core coil suffers the largest increase whereas the air-core coil is unaffected.

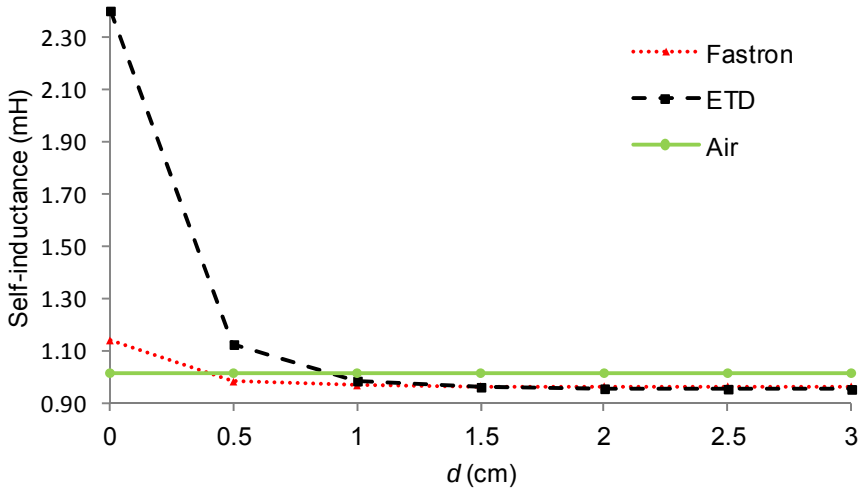

Fig. 5.10 Measured self-inductance of the different coil types under the influence of a coupled coil of the same type placed at several distances.

Fig. 5.11 presents the simulation results of *k* (absolute value) versus *d* without (in black) and with (in grey/red) the metallic plate placed at 1 cm below coil 1. Regarding first the results

without the metallic plate, the ETD-core coil achieves a higher k than the Fastron coil at all distances. At zero distance, the ETD-core coil achieves an ideal k of 1. On the other hand, the air-core coil achieves a higher k than the Fastron coil at all distances and than the ETD-core coil at distances higher than *ca*. 1 cm, thanks to its larger winding diameter. As for the results with the metallic plate, again the highest influence (decrease of k) is on the air-core coil and the lowest on the ETD-core coil.

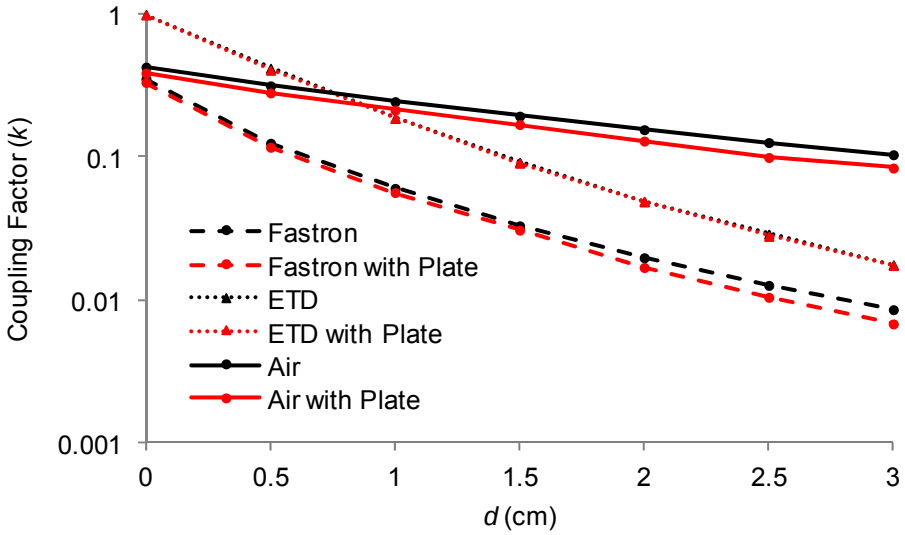

Fig. 5.11 Simulation of the evolution of *k* over *d* for the different coil types without (in black) and with (in grey/red) the metallic plate placed 1 cm below coil 1.

5.3 IPT

This section extends the work presented in Chapter 4 by adding the results of the new coil types and assessing the effects of metallic objects. An increase of the coil resistance values in Fig. 5.2 lead, from (4.26) and (4.34), to a decrease of the maximum transferred power. Quality factors Q_1 and Q_2 will also decrease and thus d_c. In addition, the decrease of the self-inductance values will change the resonant frequencies and detune the primary and secondary networks, which, in general, will also reduce the transferred power. This power decrease effect is shown in [90] and in Appendix B for a change of the capacitor values of the resonant networks. On the other hand, based on the results obtained in Fig. 5.11, the ETD-core coil achieves a higher k than the Fastron coil at all distances, which will lead, as mentioned in Chapter 4, to a higher d_{max} and d_c.

Experimental tests were carried out with the three types of coils and with and without a metallic plate. The mechanical setup presented in Fig. 3.16 was used to fix the distance between the primary and secondary networks, which were implemented in two separate PCB boards. The bottom and top boards correspond respectively to the primary and secondary networks. Distance

was adjusted manually. For the experiments, we used the SS topology. The circuit of Fig. 4.11 was used for the primary network. In this case, we used the MOSFETs BS108 (ON Semiconductor) for the primary network with a calculated R_{on} of 4 Ω. As for the secondary network, we used, for the sake of simplicity, the circuit shown in Fig. 4.4 with R_{Load} = 100 Ω. This value is within the range of limiting values of R_{Load} found in 4.7 when using the bridge rectifier.

Appropriate capacitors values (C_1 and C_2) were used for the three types of coils. First, the frequency of the class D amplifier was tuned to the primary resonant tank. Then, the resonant frequency of the secondary tank was finely tuned by using a capacitor trimmer placed in parallel with C_2, using the same technique mentioned in section 4.8. Resonant frequency was around 120 kHz. Table 5.2 shows the values of the coil resistances at the resonance frequency, which were previously shown in Fig. 5.4. For both ETD-core coils we used a winding wire with a cross-section diameter of 0.2 mm. As for the air-core coils, we used a winding wire with a cross-section diameter of 0.4 mm for the primary coil and of 0.2 mm for the secondary coil. This resulted in a lower coil resistance value for the primary coil.

Table 5.2 Measured resistances of the selected coils at *ca.* 120 kHz.

Coil	Parameter	Value
Fastron	R_{L1}, R_{L2}	22 Ω
ETD	R_{L1}, R_{L2}	16 Ω
Air Coil	R_{L1}, R_{L2}	23 Ω, 28 Ω

Load power (P_{Load}) was measured at different distances between the coils for each coil type without (in black) and with (in grey/red) a metallic plate (40 cm long, 30 cm width, 0.8 mm thick) placed at a distance of 1 cm from the bottom (primary) coil. Power was estimated by measuring the voltage drop across R_{Load} with a floating oscilloscope.

Fig. 5.12 shows the results. As for the results without the metallic plate (solid lines, in black), air-core coils presented the highest d_c, which agrees with the conclusion drawn from Fig. 5.11. However when referred to its coil diameter, ferrite-core coils overperform air-core coils. On the other hand, ETD-core coils provided the highest $P_{Load,max}$, due to their lower coil resistances (Table 5.2). Fig. 5.12 also shows a straight line corresponding to $P_{Load,req}$, which was chosen of 116 mW. This value is within the range of values found for P_{Load} in section 4.7 for the limiting values of R_{Load} . As can be seen, the resulting values of d_{max} were slightly higher than 1.5 cm and 3 cm for the Fastron and ETD-core coils, respectively. This highlights the benefits of using an ETD-core. For the air-core coils d_{max} was far larger than 3.5 cm, thanks to their much larger winding diameter. As for the effect of the metallic plate, a large power decrease was observed for the air-core coils, not being possible to reach $P_{Load,req}$. This large power

decrease was due to the generated eddy currents in the metal plate, which waste some of the transferred power to the load and change the self-inductance of the coils, detuning the primary and secondary networks. No significant effects were observed with the ferrite-core coils.

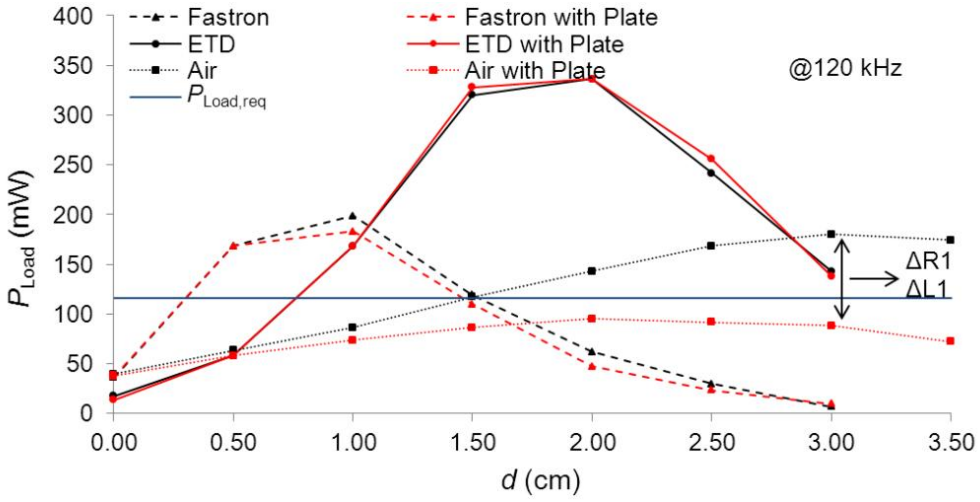

Fig. 5.12 P_{Load} vs distance (d) for the different coil types with R_{Load}=100 Ω. Results without (in black) and with (in grey/red) a metallic plate placed 1 cm below the bottom (primary) coil.

In the case of the air-core coils, in order to reduce the effects of the metallic plate, we retuned the frequency of the class D amplifier in order to cope with the inductance change of the primary coil. The capacitor trimmer in parallel with C_2 was also readjusted. The results are shown Fig. 5.13 (Air with Plate Tuned) together with the previous results shown in Fig. 5.12 for the air-core coils. As can be seen, the effects of the metallic plate over the IPT system are partially mitigated. Some effects still remain as the increase of the coil resistances, specially of R_{L1}, which according to (4.26), reduces the value of $P_{Load,max}$.

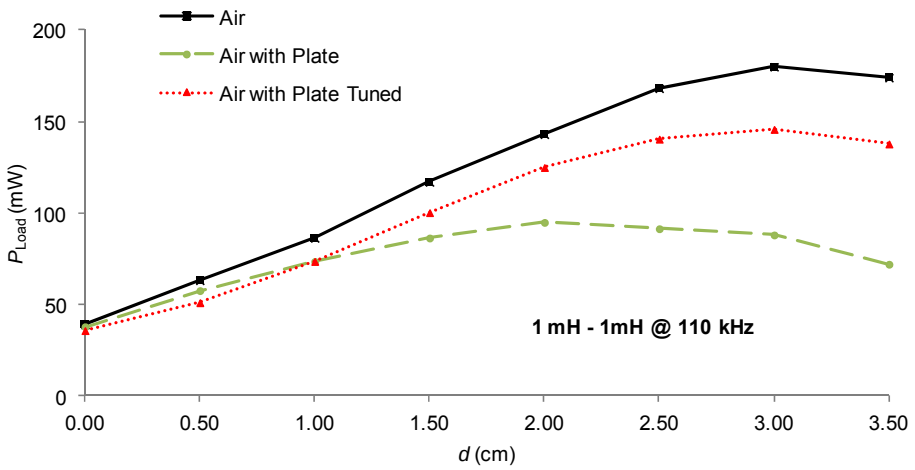

Fig. 5.13 P_{Load} vs distance (d) for different scenarios with the air core coils. The plate is placed 1 cm below the primary coil.

5.4 Passive Detection

This section extends the work presented in Chapter 3 by adding the results of the new coil types and assessing the effects of metallic objects. The same mechanical and measurement setups described in section 3.5 were used.

Fig. 5.14 shows the results of R_{in} for the ETD-core coils at d = 0.5 cm. The four captured data of R_{in} corresponding to the four cases mentioned in section 3.3 are superposed. The same as in Fig. 3.17 with the Fastron coils, the respective resonant frequencies can be clearly distinguished. As can be seen from Fig. 5.5, the value of Q_{L2} around 40 kHz is similar in both cases and thus, from (3.32), the value of Q_T and the frequency selectivity. On the other hand, the maximum values were higher than in Fig. 3.17 because of the larger value of k.

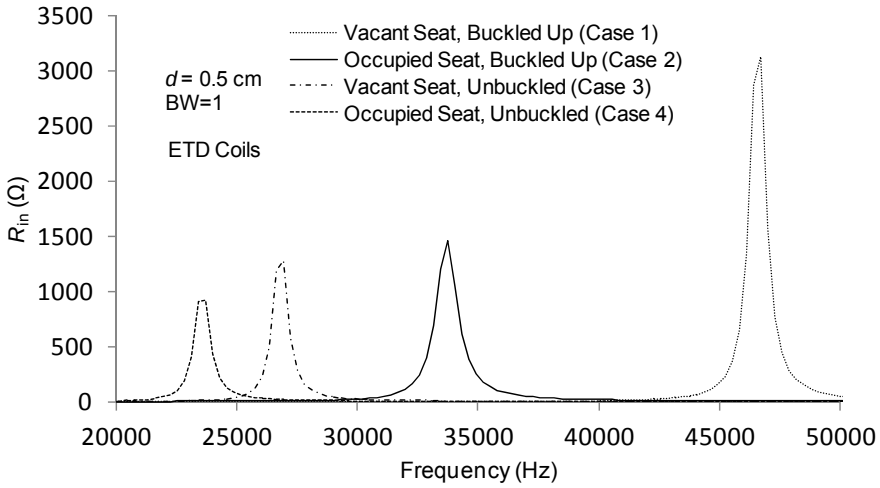

Fig. 5.14 R_{in} for the four different cases of the seat detectors at d=0.5 cm with ETD core coils.

Fig. 5.15 shows the results of R_{in} for the air-core coils at d = 0.5 cm. Now, the frequency selectivity is worse, which is due to the lower value of Q_{L2} (see Fig. 5.5) and thus of Q_T. Even so, the four cases can still be distinguished.

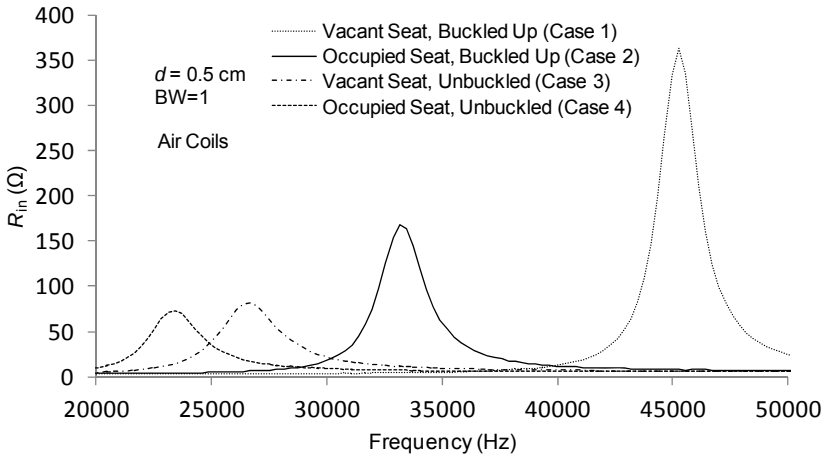

Fig. 5.15 R_{in} for the four different states of the seat sensors at d=0.5 cm with air core coils.

Fig. 5.16 shows the measured values for R_{in} for case 4 at six different values of d (0.5 cm, 1 cm, 1.5 cm, 2 cm, 3 cm, 4 cm) using the ETD-core coils. As can be seen, $R_{in,max}$ decreases for increasing distances. On the other hand, the same as in Fig. 3.18 for the Fastron coils, the resonant frequency decreases for the shortest distances. This effect is due to the increase of the self-inductance of the coils at short distances when using magnetic-core coils (Fig. 5.10).

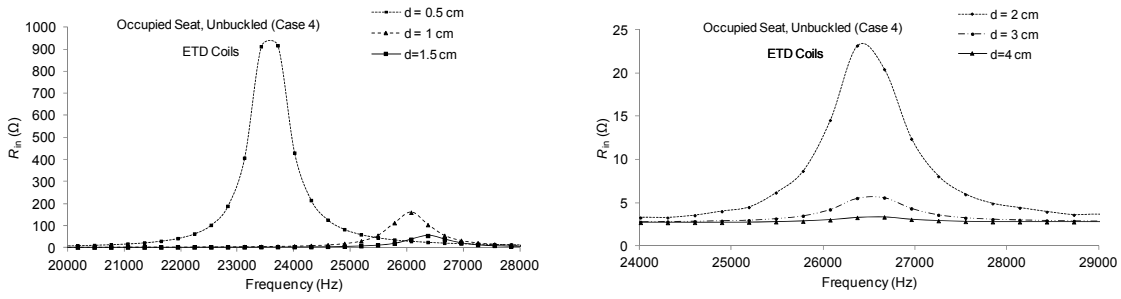

(a) (b)

Fig. 5.16 R_{in} for case 4 at different distances between the coils using ETD coils.

Fig. 5.17 shows the measured values for R_{in} for case 4 using air core coils. Again, $R_{in,max}$ decreases for increasing distances. However, now there is no change on the resonant frequency at short distances as, from Fig. 5.10, no change of the self-inductance is observed for the air-core coils.

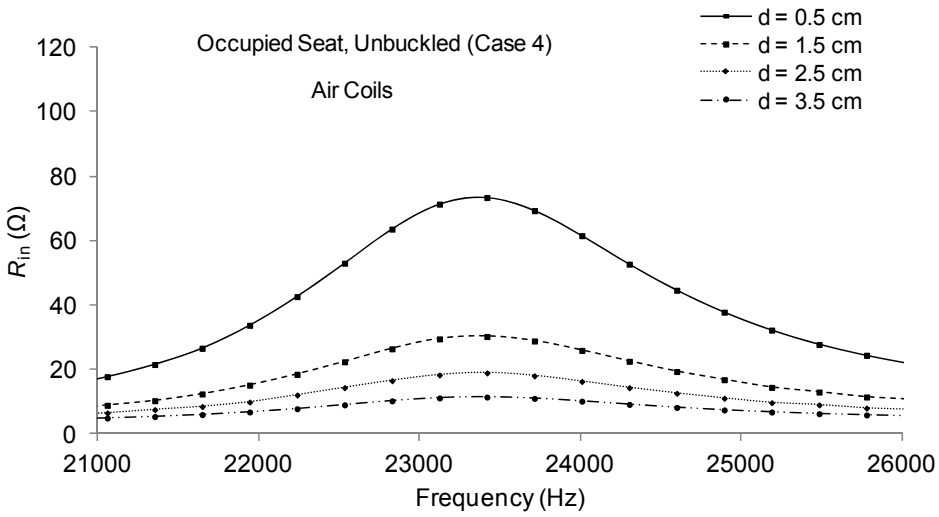

Fig. 5.17 R_{in} for case 4 at different distances between the coils using air-core coils.

The effects of the metallic objects were only assessed for the air-core coils as no significant effect is previewed for the magnetic-core coils. Fig. 5.18 shows the captured values of R_{in} for d = 7.5 cm and for the four cases with the impedance analyzer adjusted for maximum accuracy (BW = 5). Once again, captured data are superposed. The black and grey/red curves respectively correspond to the cases without and with the metallic plate placed 1 cm below the bottom (primary) coil. The metallic plate will mainly affect the primary coil by increasing its resistance and decreasing its self-inductance, as stated by (5.1). This explains, from (3.13), the higher base value of R_{in} and lower relative increase of the curves with the metallic plate against those without the metallic plate. Still, all four cases are detectable with and without the metallic plate.

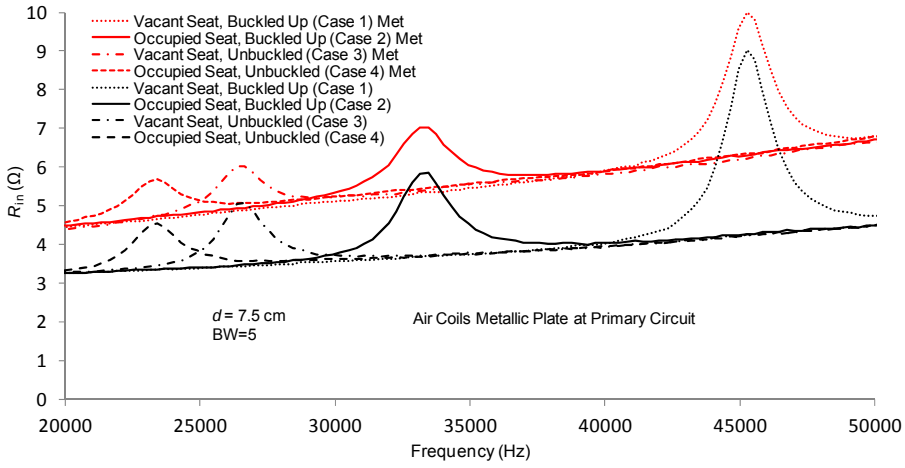

Fig. 5.18 R_{in} for case 4 with d=7.5 cm between the air-core coils with (grey/red) and without (black) a metallic plate 1 cm below the primary coil.

Chapter 6 Conclusions

This thesis proposes the use of inductive links for one application in vehicles where wiring the detectors to an electronic control unit (ECU) can become unpractical or unfeasible. The selected application is occupancy and belt detection in removable vehicle seats. Two alternatives have been considered: 1) passive sensing from a readout coil and 2) remote power transmission to the sensing unit and subsequent data transmission by a wireless transceiver. In both cases, we consider a pair of aligned coils placed respectively in the chassis floor and at the bottom of the removable seat. The topic has been introduced in chapter 1.

In chapter 2, the physical principles of magnetic induction have been introduced. The fundamental laws of electromagnetism have been reviewed and the relevant parameters involved in the scope of the thesis, such as the self-inductance of coils and the mutual inductance and coupling factor between coils, have been presented. Finite element modeling of coils has been presented as a means to numerically obtain the relevant parameters in cases where an analytical solution is not feasible. In order to calculate values of coil self-inductances and of mutual inductances and coupling factors between coils. We also show a summary of the guidelines from the International Commission on Non-Ionizing Radiation Protection (ICNIRP) in order to limit human exposure to time-varying Electromagnetic fields (EMF) with the aim of preventing adverse health effects.

In chapter 3, we have provided a comprehensive analysis for monitoring switch-type sensors that form part of an *LC* resonant circuit from a magnetically coupled readout circuit. This type of sensors can be roughly modeled as switches and mainly present two states: closed and open. Each sensor is placed in series with a capacitor and then all sensor branches are placed in parallel and wired to a coil, forming a resonant network. The state of the sensors is attained by first measuring the input resistance of a readout coil and then estimating its resonant frequency. A high peak value of the measured resistance of the readout coil facilitates an accurate determination of the resonant frequency. The peak resistance value at the resonant frequency increases with increasing values of the coupling factor and with the quality factors of the readout coil and of the resonant *LC* network. It is shown that the equivalent sensor capacitance of the resonant network is equal to the addition of all the associated capacitances of the closed sensors. The equivalent sensor resistance is a weighted sum of the individual resistances of each closed sensor. A compact expression for the overall quality factor of the resonant circuit has also been deduced. The overall value depends on the contribution of the coil quality factor and the quality factors corresponding to the closed sensor branches. Sensors with a relative high resistance can present low quality factors, adversely affecting the value of the

overall quality factor. However, by associating those sensors with the lowest valued capacitors among those selected, their detrimental influence can be minimized.

Subsequently we have particularized the analysis for the commercial seat detectors, which can be modeled as switch-type sensors. Attending to the states (open or closed) of the related occupancy sensor and belt buckle switch, four different resonant frequencies result. Working frequencies has been restricted to tens of kilohertz in order to avoid the inductive effects of the occupancy sensor and to ease an upcoming design of the electronic circuitry for the measurement of the real part of the impedance. Because the application is space-constrained, small-size coils were required. Magnetic-core coils have been considered in order to achieve high coil quality and coupling factors at frequencies of tens of kilohertz. Commercial coils of 1 mH from Fastron have been selected. A mechanical setup has been fabricated to fix the distance between the coils. Experimental tests have been carried out connecting an impedance analyzer to the readout coil and the commercial seat detectors to the resonant network. Results show that four resonant frequencies can be clearly distinguished, corresponding to the four possible states, up to distances of 3 cm. The peak resistance value decreases with increasing distances because of the lower coupling factor. The instrument uncertainty can also limit the accurate location of the resonant frequency and thus limit the maximum detection distance. On the other hand, the quality factor of the resonant circuit has been estimated. The cases where the occupancy sensor is closed present a reduced quality factor, which is due to the relative high value of its parasitic resistance in comparison with that of the belt buckle switch. Even so, the selection of the lowest capacitor value for the occupancy sensor partially mitigates this effect.

In chapter 4, the feasibility of using IPT for autonomous sensors and in particular for belt and occupancy detection in removable vehicle seats has been explored. The final aim has been to maximize the power efficiency and the powering distance range between the coupled pair of coils in order to relax the mechanical constraints. We have considered a power demand of the autonomous sensor of around 100 mW, which is the typical power consumption of radio-frequency (RF) transceivers used in them. As a means to transfer power at “mid-range” distances (higher than the radius of the coils), two loosely coupled coils tuned in resonance have been considered. The selected application was considered to be space-constrained, so that small-size coils had to be used. Autonomous sensors require a DC voltage supply. So, the use of a rectifier and voltage regulation stages has been considered. A comprehensive analysis of the impact on the system efficiency of different voltage regulators has been provided and the best regulator type determined. Both analytical derivations and experimental results have been provided.

As for the resonant tanks, both series and parallel compensation capacitors have been considered. Parallel compensation at the transmitting (primary) network shows a dependence on

both the load to be powered and the distance between the coils, which can be tricky for the tuning process. So, its use for this thesis has been discarded. As for the receiving (secondary) network, parallel compensation also shows a dependence on the load. So, series compensation both for the primary and secondary networks (ie., SS topology) has been mainly considered here. To drive the transmitting resonant network, a commercial class D amplifier was used. A rather low frequency of operation (< 150 kHz) was selected for two reasons: 1) to better comply with the reference levels for general public exposure to time-varying electric and magnetic fields, and 2) to reduce the circuit complexity and power losses of the power amplifier. Commercial (from Fastron) ferrite-core coils have been selected against air-core coils as they lead to higher coupling and quality factors. The first value of each decade provided by the manufacturer was selected, i.e. 10 μH, 100 μH, 1 mH, and 10 mH. Then, their coil resistances and quality factors have been measured from 1 kHz to 150 kHz. Resistance values increase with frequency, which is due to the joint combination of skin and proximity effects and the losses of the ferrite. Their quality factors increase steeply at low frequencies. A maximum has been achieved around 40 kHz for 100 μH and 1 mH. For the other two coils, 10 μH and 10 mH, the maximum value has been achieved at the highest tested frequency, approximately 120 kHz. On the other hand, the achieved maximum value at a given frequency increased with an increase of the coil value. Thus, the highest two coil values, 1 mH and 10 mH, have been selected for the primary and secondary coils of the SS topology.

A rectifier and some kind of voltage regulation are required in the secondary network when its load is an autonomous sensor, which requires a fixed DC voltage supply. Two different rectifiers have been considered: bridge and half-wave. Four types of voltage regulators have been analyzed, such as linear shunt and series regulators, and buck and boost switching converters. Here, their impact on the system power efficiency had been assessed. Through computations and experimental results, we have demonstrated that the shunt regulator provides the maximum overall efficiency. On the other hand, switching regulators can lead to an unstable behavior, which here mainly affects the boost converter.

Computations have been carried out for the different combinations of coils and two resonant frequencies: 40 kHz and 120 kHz. An equivalent load of 100 Ω has been used for the autonomous sensor. Five cases have been computed for both current-driven bridge and half-wave rectifiers. Computed graphs show that, in all the cases, the operating points for the shunt regulator always lead to a lower equivalent load resistance (R_{Load}) and, thus, to a higher power efficiency. In addition, the use of rechargeable batteries instead of the regulators have been considered. Batteries behave as shunt regulators but with the advantage of gathering the surplus in the provided energy to the autonomous sensor, otherwise wasted in the regulator. Thus, higher efficiencies are achieved with batteries with respect to using shunt regulators. Special

attention must be paid, though, to the regulations that affect the disposal of batteries. Experimental tests have been carried out using a mechanical setup to fix the distance between the coils. Experimental results mainly agree with computed results. Achieved power efficiencies were around 40 %, 25 %, and 10 % for coil distances of 1 cm, 1.5 cm, and 2 cm, respectively, which is remarkable considering the inner diameter of the coils, 0.6 cm. Experimental tests also showed that the autonomous sensor, which included the seat detectors and a wireless transceiver, was properly powered up to coil distances of 2.5 cm. The data about the state of the sensors were wirelessly transmitted to a base unit.

In chapter 5, the work of chapter 3 and 4 have been extended in order to assess different types of coils and analyze the effect of metallic structures. Three different coil types, two with ferrite-core and one with an air-core, were used. Numerical results show that ferrite-core coils, in especial that with an ETD-core, are less affected by the presence of metallic structures. Experimental results show that the air-core coils provided the maximum powering distance thanks to its much larger winding diameter, 6.5 cm. However, when approaching a metallic plate, the transferred power with the air-core coils to the load was insufficient for the intended application. On the other hand, ferrite-core coils barely noticed the presence of the metallic plate, achieving the ETD-core coils the highest powering distance, around 3 cm. As for the passive detection, the presence of a metallic plate below the primary air-core coil slightly affected the measured resistance values but detection of the four possible states of the seat detectors was still possible. A distance of 7.5 cm between the coils has been successfully tested when using the air-core coils.

Several appendices have been added. Appendix A shows the calculation of the measurement uncertainty of the impedance analyzer used for the experimental tests in Chapter 3. Appendix B, C, and D add new results to that of Chapter 4. In appendix B, the load power is obtained, both with computations and with experimental tests, with respect to the distance between the coils when using a fixed resistance for the load. In appendix C, related with section 4.7, new graphs for the SS topology with the half-wave rectifier are presented. In appendix D, detailed results of the efficiencies defined in section 4.6.5 are shown. Finally, appendix E assess the accomplishment of the ICNIRP regulations.

References

[1] J., Turley, "*Motoring with Microprocessors,*" Embedded Systems Design. August 11, 2003. Access date: January, 4. 2012. [Online]. Available on: - http://www.embedded.com/columns/significantbits/13000166?_requestid=265679

[2] Center for Automotive Research. *"Automotive Technology: Greener Vehicles, Changing Skills,"*. May 2011. Access date: January, 4. 2012. [Online]. Available on: http://drivingworkforcechange.org/reports/electronics.pdf

[3] K. F. Reinhart, and M. Illing, "*Automotive Sensor Market,*" Sensors Update. Volume 12, Issue 1 pp. 213-230. February 25, 2003. Access date: January, 4. 2012. [Online]. Available on: <http://www3.interscience.wiley.com/cgi-bin/fulltext/103519894/PDFSTART>.

[4] Council Directive 70/156/EEC of 6 February 1970 on the approximation of the laws of the Member States relating to the type-approval of motor vehicles and their trailers. Official Journal L 42, 23/02/1970.

[5] Regulation No. 64 of the Economic Comission for Europe of the United Nations, Nov. 26, 2010 , "Uniform provisions concerning the approval of vehicles with regard to their equipment which may include: a temporary-use spare unit, run-flat tyres and/or a run-flat system, and/or a tyre pressure monitoring system," Official Journal L 310, 26/11/2010.

[6] R. Elfrink, S. Matova, C. de Nooijer, M. Jambunathan, M. Goedbloed, J. van de Molengraft, V. Pop, R.J.M Vullers, M. Renaud, R. van Schaijk, "Shock induced energy harvesting with a MEMS harvester for automotive applications," *IEEE International Electron Devices Meeting (IEDM) 2011*, pp.29.5.1-29.5.4, Dec. 2011.

[7] S. Roundy, "Energy harvesting for tire pressure monitoring systems: design considerations" Proceedings Power MEMS, pp 1-6, 2008.

[8] T.J Kazmierski and S. Beeby , "Energy harvesting systems: principles, modeling and applications", Springer, ISBN: 9781441975642, 2011.

[9] H. Zervos, "*Energy Harvesting for automotive Application,"* IDTechEx Ltd, 2011, Access date: January, 5. 2012. [Online]. Available on: http://media.idtechex.com/pdfs/en/S2142B5538.pdf

[10] NHTSA Technical Report, "Results of the Survey on the Use of Passenger Air Bag Onn-Off Switches," DOT HS809 689, Nov. 2003.

[11] A. Lie, A. Kullgren, M. Krafft, and C. Tingvall, "Intelligent Seat Belt Reminders — Do they Change Driver Seat Belt use in Europe?," *Traffic Injury Prevention*, vol. 9, no. 5, pp. 446-449, 2008.

[12] T. Janitzek, F. Achterberg, “Seat Belt Reminders. Implementing advanced Safety Technology in Europe’s Cars,” European Transport Safety Council, 2006.

[13] Euro NCAP, “Assessment Protocol - Safety Assist,” Version 5.4, June 2011.

[14] Gloucesterpharma Website. Access date: February, 4. 2012. [Online]. Available on: http://www.gloucesterpharma.com/do-seatbelts-really-save-lives/

[15] Fact Sheet . IEE company. Access date: February, 4. 2012. [Online]. Available on: http://www.iee.lu/includes/content_jdm_framework/contenus/fichiers/el_1978_fichier_1/2012-05-16-FS-SBR_web.pdf

[16] J. Garcia-Canton, A. Merlos, and A. Baldi, “A wireless LC chemical sensor based on a high quality factor EIS capacitor,” *Sensors and Actuators B,* vol.126, pp.648-654, 2007.

[17] Sajeeda and T. J. Kaiser , "Passive Telemetric Readout System," *IEEE Sensors Journal*, vol.6, no.5, pp.1340-1345, Oct. 2006.

[18] D. Marioli, E. Sardini, and M. Serpelloni, "Passive Hybrid MEMS for High-Temperature Telemetric Measurements," *IEEE Transactions on Instrumentation and Measurement*, vol.59, no.5, pp.1353-1361, May 2010.

[19] G. J. Radosavljevic, L. D. Zivanov; W. Smetana, A. M. Maric, M. Unger and L. F. Nad”, A Wireless Embedded Resonant Pressure Sensor Fabricated in the Standard LTCC Technology," IEEE Sensors Journal, vol.9, no.12, pp.1956-1962, Dec. 2009.

[20] M.M. Andringa, D.P. Neikirk, N.P. Dickerson, and S.L. Wood, "Unpowered wireless corrosion sensor for steel reinforced concrete," in *IEEE Sensors 2005,* Oct. 30-Nov. 3, 2005.

[21] J. Wu and W. Wu, “Study on wireless sensing for monitoring the corrosion of reinforcement in concrete structures,” *Measurement*, vol. 43, no. 3, pp. 375-380, April 2010.

[22] R. Darraba, “A Movable or Removable Seat for a Motor Vehicle,” World patent, WO 2004/098943 A1, Nov 18, 2004.

[23] G. L. Johnson, "*Building the world's largest Tesla coil-history and theory*," in *Power Symposium, 1990. Proceedings of the Twenty-Second Annual North American*, 1990, pp. 128-135.

[24] G. A. Landis, "*Photovoltaic receivers for laser beamed power in space*," in IEEE Photovoltaic Specialists Conference, pp. 1494-1502 vol.2, 1991.

[25] A. Dolgov, R. Zane, and Z. Popovic, "*Power Management System for Online Low Power RF Energy Harvesting Optimization*," *IEEE Transactions on Circuits and Systems I: Regular Papers,* vol. 57, pp. 1802-1811, 2010.

[26] C. Liu, A. P. Hu, and N. K. C. Nair, "*Coupling study of a rotary capacitive power transfer system,*" in *IEEE International Conference on Industrial Technology, ICIT 2009*, pp. 1-6, 2009.

[27] Z. Wenqi and M. Hao, "Steady-*State Analysis of the Inductively Coupled Power Transfer System,*" in *IEEE 32nd Annual Conference on Industrial Electronics*, Paris, France, pp. 2438-2443, 2006.

[28] R. H. Nansen, "*Wireless power transmission: the key to solar power satellites*," *IEEE Aerospace and Electronic Systems Magazine,* vol. 11, pp. 33-39, 1996.

[29] J. Benford, "*Space Applications of High-Power Microwaves*," IEEE Transactions on Plasma Science, vol. 36, pp. 569-581, 2008.

[30] C.S. Wang, O. H. Stielau, and G. A. Covic, "Design considerations for a contactless electric vehicle battery charger," *IEEE Trans. Industrial Electronics*, vol. 52, no. 5, pp. 1308–1314, Oct. 2005.

[31] A. P. Hu, "Selected Resonant Converters for IPT Power Supplies," PhD thesis, Department of Electrical and Computer Engineering, University of Auckland, Auckland, 2001.

[32] H. L. Li, "High Frequency Power Converters Based on Energy Injection Central for IPT Systems" PhD thesis, Department of Electrical and Computer Engineering, University of Auckland, Auckland, 2011.

[33] M. Budhia, G.A. Covic, J.T. Boys, "Design and Optimization of Circular Magnetic Structures for Lumped Inductive Power Transfer Systems," *IEEE Transactions on Power Electronics*, vol.26, no.11, pp. 3096-3108, Nov. 2011.

[34] H.H. Wu, G.A. Covic, J.T. Boys, D.J. Robertson, "A Series-Tuned Inductive-Power-Transfer Pickup With a Controllable AC-Voltage Output," *IEEE Transactions on Power Electronics*, vol.26, no.1, pp.98-109, Jan. 2011.

[35] H.L. Li, A.P. Hu, G.A. Covic, "A Direct AC–AC Converter for Inductive Power-Transfer Systems," *IEEE Transactions on Power Electronics*, vol.27, no.2, pp.661-668, Feb. 2012.

[36] N.A. Keeling, G.A. Covic, and J.T. Boys, "A Unity-Power-Factor IPT Pickup for High-Power Applications," *IEEE Trans. Industrial Electronics*, vol. 57, no.2, pp.744-751, Feb. 2010.

[37] H.H. Wu, J.T. Boys, and G.A. Covic, "An AC Processing Pickup for IPT Systems," *IEEE Trans. Power Electronics*, vol.25, no.5, pp.1275-1284, May 2010.

[38] D. C. J. Krop, E. A. Lomonova, J. W. Jansen, and J. J. H. Paulides, "A study on the integration of contactless energy transfer in the end teeth of a PM synchronous linear motor," *J. Applied Physics*, vol. 105, 07F115, 2009.

[39] J. de Boeij, E. Lomonova, and J. Duarte, "Contactless Planar Actuator With Manipulator: A Motion System Without Cables and Physical Contact Between the Mover and the Fixed World," *IEEE Trans. Industry Applications*, vol.45, no.6, pp.1930-1938, Nov-Dec. 2009.

[40] A. J. Moradewicz and M. P. Kazmierkowski, "Contactless Energy Transfer System With FPGA-Controlled Resonant Converter," *IEEE Trans. Industrial Electronics*, vol.57, no.9, pp.3181-3190, Sept. 2010.

[41] L, Xun and S.Y. Hui, "Optimal Design of a Hybrid Winding Structure for Planar Contactless Battery Charging Platform," *IEEE Trans. Power Electronics*, vol.23, no.1, pp. 455-463, Jan. 2008.

[42] S.Y.R. Hui and W.W.C. Ho, "A new generation of universal contactless Battery Charging platform for portable Consumer Electronic equipment," *IEEE Trans. Power Electronics*, vol.20, no.3, pp. 620- 627, May 2005.

[43] P. Tipler, A. Mosca, "Physics for Scientists and Engineers," W. H. Freeman Company, ISBN 0716743892, 2004.

[44] W. Benenson, J. Harris, H. Stocker, H. Lutz, "Handbook of Physics," Springer, ISBN 0387952691, 2002.

[45] D. Fleisch, "A Student's Guide to Maxwell's Equations," Cambridge, ISBN 97805218777619, 2008.

[46] P. Lorrain, D. Corson, "Campos y Ondas Electromagnéticas," Selecciones Científicas, ISBN 8485021290, 1990, (in Spanish).

[47] T. Jäger, "Drathloses spindelintegriertes Sensorsystem zur Überwachnung der HSK-Schnittstelle bei automatischen Werkzeugwechsel," Der Andere Verlag, ISBN:9783862470228, 2010 (in German).

[48] Phillips report HB2009, "Soft Ferrite and Accessories", April 2000.

[49] F. Terman, "Radio Engineers Handbook," McGrawHill, 1943.

[50] Y. Lee, "Antenna Circuit Design for RFID Applications," AN710 Microchip, Access date: January, 7. 2012. [Online]. Available on: http://ww1.microchip.com/downloads/en/appnotes/00710c.pdf

[51] K, Van Schuylenberd, R. Puers, “Inductive Powering. Basic Theory and Applications to Biomedical Systems,” Springer, ISBN 9789048124114, 2009.

[52] R. Ericsson, “Fundamentals of Power Electronics, Kluwer Academic Publications, 2000.

[53] Mohan, Undeland, Robbins, “Power Electronics Converter, Applications and Design,” ISBN:0471226939, 2009.

[54] B. Lenaerts, R. Puers, “Omnidirectional Inductive Powering for Biomedical Implants”, Springer, ISBN 9781402090745, 2009.

[55] ICNIRP International Comission on Non-Ionizing Radiation Protection, “Guidelines for limiting Exposure to Time-Varying Electric, Magnetic, and Electro-Magnetic Fields (Up to 300 GHz,” Health Physics, vol. 74, no. 4, pp. 494-522, 1998. January, 7. 2012. [Online]. Available on: http://www.icnirp.de/documents/emfgdl.pdf

[56] 1999/5/EC, “Radio Equipment and Telecommunications Terminal Equipment and the Mutual Recognition of their Conformity,” Official Journal of the European Communities no. L 91/10, Mar. 9, 1999. January, 7. 2012. [Online]. Available on: http://eur-lex.europa.eu/LexUriServ/LexUriServ.do?uri=OJ:L:1999:091:0010:0010:EN:PDF

[57] 1999/519/EC, “Council Recommendation of 19 July on the limitation of exposure of the general public to electromagnetic fields (0 Hz to 300 GHz),” Official Journal of the European Communities no. L 199/59, Jul. 12, 1999. January, 7. 2012. [Online]. Available on: http://ec.europa.eu/enterprise/sectors/electrical/files/lv/rec519_en.pdf

[58] T. J. Harpster, S. Hauvespre, M. R. Dokmeci, and K. Najafi, “A passive humidity monitoring system for in situ remote wireless testing of micropackages,” Journal of Microelectromechanical Systems, vol. 11, no. 1, pp. 61–67, Feb. 2002.

[59] O. Akar, T. Akin, and K. Najafi, “A wireless batch sealed absolute capacitive pressure sensor,” Sens. Actuators A, vol. 95, no. 1, pp. 29–38, Dec. 2001.

[60] A. Baldi, W. Choi, and B. Ziaie, “A self-resonant frequency-modulated micromachined passive pressure transensor,” IEEE Sensors Journal, vol. 3, no. 6, pp. 728–733, Dec. 2003.

[61] J. C. Butler , A. J. Vigliotti , F. W. Verdi and S. M. Walsh "Wireless, passive, resonant-circuit, inductively coupled, inductive strain sensor," Sensors and Actuators A, vol.102, pp.61-66, 2002.

[62] R. Nopper, R. Niekrawietz, and L. Reindl, "Wireless Readout of Passive LC Sensors," *IEEE Transactions on Instrumentation and Measurement*, vol.59, no.9, pp.2450-2457, Sept. 2010.

[63] R. Nopper, R. Has, and L. Reindl, "A Wireless Sensor Readout System—Circuit Concept, Simulation, and Accuracy," *IEEE Transactions on Instrumentation and Measurement*, vol.60, no.8, pp.2976-2983, Aug. 2011.

[64] J. Coosemans, M. Catrysse, and R. Puers, "A readout circuit for an intraocular pressure sensor," Sens. Actuators A, Phys., vol. 110, no. 1–3, pp. 432–438, Feb. 2004.

[65] Agilent, "4294A. Precision Impedance Analyzer. Operation Manual," Access date: February, 4. 2012. [Online]. Available on: http://cp.literature.agilent.com/litweb/pdf/04294-90060.pdf

[66] D.M. Dobkin, *The RF in RFID. Passive UFH RFID in Practice*. Amsterdam: Newnes-Elsevier, 2008.

[67] S.Y.R. Hui and W.W.C. Ho, "A new generation of universal contactless Battery Charging platform for portable Consumer Electronic equipment," *IEEE Trans. Power Electronics*, vol.20, no.3, pp. 620- 627, May 2005.

[68] A. Kurs, A. Karalis, R. Moffatt, J.D. Joannopoulos, P. Fisher, and M. Soljačić, "Wireless Power Transfer via Strongly Coupled Magnetic Resonances," *Science*, Vol. 317, pp. 83-866, July 2007.

[69] A.P. Sample, D.A. Meyer, and J.R. Smith, "Analysis, Experimental Results, and Range Adaptation of Magnetically Coupled Resonators for Wireless Power Transfer," *IEEE Trans. Industrial Electronics*, vol.58, no.2, pp.544-554, Feb. 2011.

[70] C. Chih-Jung, C. Tah-Hsiung, L. Chih-Lung, and J. Zeui-Chown, "A Study of Loosely Coupled Coils for Wireless Power Transfer," *IEEE Trans. on Circuits and Systems II: Express Briefs* , vol.57, no.7, pp.536-540, July 2010.

[71] B.L. Cannon, J.F. Hoburg, D.D. Stancil, and S.C. Goldstein, "Magnetic Resonant Coupling As a Potential Means for Wireless Power Transfer to Multiple Small Receivers," *IEEE Trans. Power Electronics*, vol.24, no.7, pp.1819-1825, July 2009.

[72] A. K. RamRakhyani, S. Mirabbasi, and M. Chiao, "Design and Optimization of Resonance-Based Efficient Wireless Power Delivery Systems for Biomedical Implants," *IEEE Trans. on Biomedical Circuits and Systems*, vol.5, no.1, pp.48-63, Feb. 2011.

[73] W.H. Ko, S.P. Liang, and C.D.F. Fung, "Design of radio-frequency powered coils for implant instruments," Medical and Biological Engineering and Computing, vol. 15, no. 6, pp. 634-640, 1977.

[74] M.W. Baker, R. Sarpeshkar, "Feedback Analysis and Design of RF Power Links for Low-Power Bionic Systems," *IEEE Trans. Biomedical Circuits and Systems*, vol.1, no.1, pp.28-38, March 2007.

[75] ETV Corporation Pty Limited. Access date: February, 4. 2012. [Online]. Available: http://www.etv.com.au/

[76] NHTSA Technical Report, "Results of the Survey on the Use of Passenger Air Bag Onn-Off Switches," DOT HS809 689, Nov. 2003.

[77] X Liu, W.M.Ng, C.K.Lee and S.Y.Hui "Optimal operation of contactless transformers with resonance in secondary circuits" in Proc 23rd annual IEEE Applied Power Electronics Conference, Austin Texas, Feb 24-28 2008, pp 645-650.

[78] C.-S. Wang, G. A. Covic and O. H. Stielau, "Power transfer capability and bifurcation phenomena of loosely coupled inductive power transfer systems," IEEE Trans. on Indus. Electron., vol. 51, no. 1, pp. 148 - 157, Feb. 2004, 2004.

[79] C. S. Wang, O. H. Stielau and G. A. Covic, "Design considerations for a contactless electric vehicle battery charger," IEEE Trans. Ind. Electronics, vol. 52, no. 5, pp. 1308-1314, Oct. 2005.

[80] H.L. Li, A.P. Hu, G.A. Covic and C.S. Tang, "Optimal coupling condition of IPT system for achieving maximum power transfer," Electronics Letters , vol.45, no.1, pp.76-77, Jan. 2009.

[81] C. Chih-Jung, C. Tah-Hsiung, L. Chih-Lung, and J. Zeui-Chown, "A Study of Loosely Coupled Coils for Wireless Power Transfer," *IEEE Trans. Circuits and Systems II: Express Briefs* , vol.57, no.7, pp.536-540, July 2010.

[82] T.D. Dissanayake, A.P. Hu, S. Malpas, L. Bennet, A. Taberner, L. Booth, D. Budget", Experimental Study of a TET System for Implantable Biomedical Devices," *IEEE Trans. on Biomedical Circuits and Systems,* , vol.3, no.6, pp.370-378, Dec. 2009.

[83] P.C. Crepaldi, T.C. Pimenta, R.L. Moreno, E.C. Rodriguez, "A Low Power CMOS Voltage Regulator for a Wireless Blood Pressure Biosensor," *IEEE Trans. Instrumentation and Measurement*, vol.61, no.3, pp.729-739, March 2012.

[84] R. Carta, M. Sfakiotakis, N. Pateromichelakis, J. Thoné, D.P. Tsakiris, R. Puers, "A multi-coil inductive powering system for an endoscopic capsule with vibratory actuation," *Sensors and Actuators A*, vol. 172, no. 1, pp. 253-258, December 2011.

[85] 2006/66/EC, “Batteries and Accumulators and Waste Batteries and Accumulators and Repealing Directive 91/157/EEC,” Official Journal of the European Communities no. L 266/1, Sep. 6, 2006. January, 7. 2012. [Online]. Available on: http://eur-lex.europa.eu/LexUriServ/LexUriServ.do?uri=OJ:L:2006:266:0001:0014:en:PDF

[86] H. Zangl, A. Fuchs, T. Bretterklieber, M.J. Moser, G. Holler, "Wireless Communication and Power Supply Strategy for Sensor Applications Within Closed Metal Walls," *Instrumentation and Measurement, IEEE Transactions on* , vol.59, no.6, pp.1686-1692, June 2010.

[87] T. Jager, P. Sulzberger, K. Wulff, L. M. Reindl, "Integrated low-power RFID-S-system for online temperature and high-resolution displacement monitoring on high speed spindle rotors," *Wireless Sensing, Local Positioning, and RFID, 2009. IMWS 2009. IEEE MTT-S International Microwave Workshop on* , vol., no., pp.1-4, 24-25 Sept. 2009.

[88] J. Albesa, T. Jáger, L. M. Reindl, and M. Gasulla, “Wireless Power Transmission for Low-Power Autonomous Sensors in Vehicles,” in *Proc. IEEE Vehicular Technology Conference*, 5-8 September 2011.

[89] J. Albesa, M. Gasulla, “Voltage Regulation on Inductive Power Links for Autonomous Sensors”, *Proc. of IEEE I2MTC*, Graz, Austria.

[90] H.H. Wu, A.P. Hu, S.C. Malpas, D.M. Budgett,"Determining optimal tuning capacitor values of TET system for achieving maximum power transfer," *Electronics Letters* , vol.45, no.9, pp.448-449, April 23, 2009.

[91] C. Gabriel *et al*, “Electrical conductivity of tissue at frequencies below 1 MHz,” *Phys. Med. Biol.* 54 4863, 2009.

Publications

International Conferences

[1] J. Albesa, R. Casas, M. T. Penella, and M. Gasulla, "REALnet: An environmental WSN Testbed," in *International Conference on Sensor Technologies and Applications, 2007. SensorComm*, 2007, pp. 502-507.

[2] J. Albesa, and M. Gasulla, "Intra-vehicular Wireless Sensor Networks", in FITICA'09- *Fórum Internacional de las TIC en la automoción 2009*, Jan, 26, 2009.

[3] M. T. Penella, J. Albesa, and M. Gasulla, "Powering Wireless Sensor Nodes: Primary Batteries versus Energy Harvesting," in *I2MTC 2009 - International Instrumentation and Measurement Technology Conference*, Singapore, May, 5-7., 2009, pp. 1625-1630.

[4] J.Albesa and M.Gasulla, "Seat Occupancy and Belt Detection in Removable Seats via Inductive Coupling," in *VTC-Fall 2011 – Vehicular Technology Conference,* San Francisco, Sept. 5-8., 2011.

[5] J.Albesa, T.Jäger, L.Reind and M.Gasulla, "Wireless Power transmission for Autonomous Sensors in Removable Vehicle Seats," in *VTC-Fall 2011 – Vehicular Technology Conference,* San Francisco, Sept. 5-8., 2011.

[6] J. Albesa, M. Gasulla, "Voltage Regulation on Inductive Power Links for Autonomous Sensors", in *I2MTC 2012 - International Instrumentation and Measurement Technology Conference*, Graz, Austria.

[7] J. Albesa, M. Gasulla, "Inductive Power Transfer for Autonomous Sensors in Presence of Metallic Structures", in *I2MTC 2012 - International Instrumentation and Measurement Technology Conference*, Graz, Austria.

Journals

[1] J. Albesa, M. Gasulla, J. Higuera, M. T. Penella, J. Polo,"REALnet: An environmental Wireless Sensor Network" in "Pervasive Computing Approaches to Environmental Sustainability," *IEEE Pervasive Computing*, vol. 8, pp. 55-55, 2009.

[2] J. Albesa, M. Gasulla, "Monitoring Switch-Type Sensors via Inductive Coupling: Application to Occupancy and Belt Detection in Removable Vehicle Seats," *IEEE Transactions on Power Electronics,* (Accepted).

Patents

[1] J. Albesa, M. Gasulla, "Dispositivo para la transmisión de energía para sensores autónomos en asientos extraíbles de vehículos vía acoplo inductivo," Spanish Patent, P201131449. September 5, 2011.

[2] J. Albesa, M. Gasulla, "Método para la monitorización del estado de detectores en asientos extraíbles de vehículos vía acoplo inductivo", Spanish Patent, P201131451. September 5, 2011.

Appendices

Appendix A Measurement Uncertainty

This appendix shows how we calculated the parameter E in section 3.5 from the manufacturer specifications. The impedance analyzer allows the measurement of a two-parameters model, i.e. an inductance in series with a resistance (R_s). The uncertainty specified for the resistance measurements is

$$R_S = \pm \frac{E}{D_{\mathrm{X}}}[\%] \tag{A.1}$$

for $Q_x > 10$, where

$$D_{\mathrm{x}} = \frac{1}{Q_{\mathrm{X}}} = \frac{R}{X} \tag{A.2}$$

being R and X the real and imaginary parts of the tested impedance.

E is given by.

$$E = E'_{\mathrm{p}} + \left(\frac{Z'_{\mathrm{S}}}{|Z_{\mathrm{X}}|} + Y'_{\mathrm{p}} \cdot |Z_X| \right) \times 100 \tag{A.3}$$

where Z_x is the tested impedance and

$$\begin{gathered} E'_{\mathrm{p}} = E_{\mathrm{PL}} + E_{\mathrm{PBW}} + E_{\mathrm{POSC}} + E_{\mathrm{P}}[\%] \\ Y'_0 = Y_{\mathrm{OL}} + K_{\mathrm{BW}} \times K_{Y_{osc}} \times (Y_{\mathrm{ODC}} + Y_{\mathrm{O}})[\mathrm{S}] \\ Z'_{\mathrm{S}} = Z_{\mathrm{SL}} + K_{\mathrm{BW}} \times K_{Z_{\mathrm{OSC}}} \times Z_{\mathrm{S}} \end{gathered} \tag{A.4}$$

where E_{PL}, Y_{oL} and Z_{SL} are zero in our case.

The measurements are fulfilled with a voltage oscillator of V_{osc} = 500mV, frequency under 50 kHz and BW = 1 or BW = 5. Thus, the values for the rest of parameters of the expression (A.3) are

$$E_{\mathrm{POSC}} = 0.03 \times \left(\frac{500}{V_{\mathrm{OSC}}} \right) = 0.03$$

$$E_{\mathrm{PBW=5}} = 0, E_{\mathrm{PBW=1}} = 0.8$$

$$K_{\mathrm{Yosc}} = \frac{500}{V_{\mathrm{osc}}} = 1 \tag{A.5}$$

$$K_{\mathrm{Zosc}} = \frac{500}{V_{\mathrm{osc}}} = 1$$

$$K_{\mathrm{BW=5}} = 1, K_{\mathrm{BW=1}} = 6$$

$$Y_{\mathrm{DC}} = 0$$

Y_o, E_p, Z_s are calculated using Table A.1, resulting in Y_0 = 2.5 ns, E_p = 0.075 % and Z_s = 2.5 mΩ.

Table A.1 Y_o, E_p, Z_s in function of the frequency and the setup of the impedance analyzer [65].

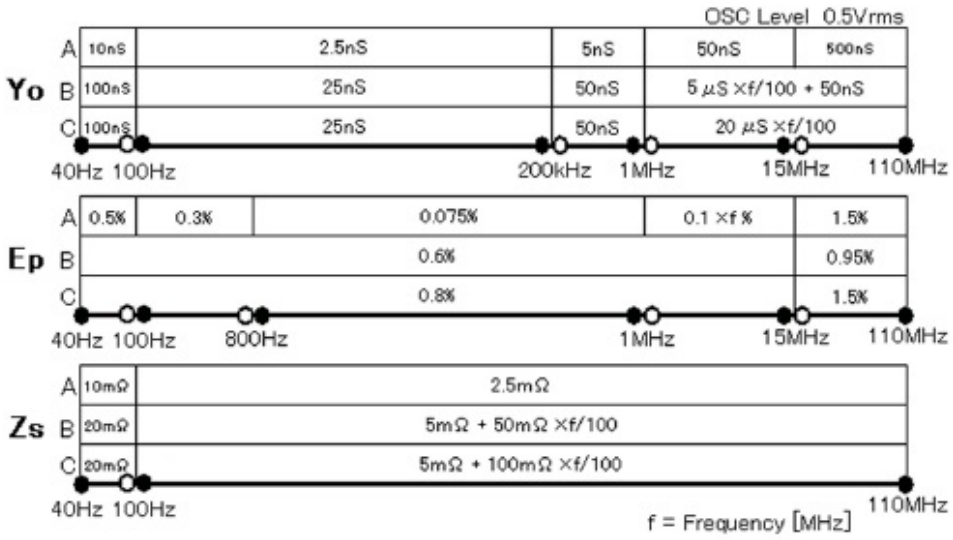

A = HP 4294A front panel 4 terminal pair port (no extension),
B = 7-mm one port (with HP 42942A).
C = Probe 3.5-mm port (with HP 42941A).
For accuracy at probe tip, add the following error factors (typical):
Yo: + 2πf×0.1 μS
Zs: + 20mΩ

Finally, the resulting values for E are 0.88 % and 0.08 % for BW = 1 and BW = 5 respectively.

Appendix B P_{Load} versus distance. Computations and Experimental Results

B.1 Computations

Computations of (4.18) were carried out in order to obtain P_{Load} versus distance for two topologies (SS and SP) and for two resonant frequencies (40 kHz and 120 kHz). For both topologies we considered the bridge rectifier of Fig. 4.15. We used 1 mH and 10 mH for the coils of the series resonant networks, whereas 10 μH and 100 μH were used for the parallel networks.

The circuit schematic of the primary network is shown in Fig. 4.11. For the experimental setup, the model BS108 (ON Semiconductor) was used for the MOSFETs. The MOSFET manufacturer specifies an ON resistance (R_{ON}) of 8 Ω (@ V_{GS} = 2.8 V). In our case, we measured a lower value, around 4 Ω, due to the resulting higher value of V_{GS}. In order to keep the power dissipation across the MOSFET within the safe limit recommended by the manufacturer (350 mW), the overall resistance of the primary network, R_1+R_r, needs to be higher than 18 Ω. For this purpose, we added a resistance (R_p) in series with the L_1C_1 resonant tank. Thus, $R_s = R_{ON}+R_p$ in Fig. 4.4. As $R_1 = R_s+R_{L1}$, the appropriate value of R_p will depend on the value of R_{L1}, which depends on the selected coil and resonance frequency.

Table B.1 shows the parameters values used for the computations of (4.18). The values of k were taken from the simulations of the ferrite-core coil presented in Fig. 3.14 and were used to calculate R_r from (4.19); resistance values of the coils were taken from Fig. 4.9; ; R_1 was found as the addition of R_{ON}, R_p and R_{L1}; and R_p was conveniently selected to accomplish with the safe limit recommended by the MOSFET manufacturer.

Table B.1 Values of the parameters used for computations.

Parameter		Values	
$V_{1,rms}$		5.4 V	
$R_{GS,ON}$, R_L		4 Ω, 90 Ω	
k @ d=0.5, 1, 1.5 cm		0.126, 0.061, 0.033	
f_r		40 kHz	120 kHz
Coil Inductance and Resistance	10 μH	0.21 Ω	0.52 Ω
	100 μH	0.84 Ω	3.4 Ω
	1 mH	6.45 Ω	22 Ω
	10 mH	44 Ω	117 Ω
R_p	L_1=1 mH	10 Ω	0 Ω
	L_1=10 mH	0 Ω	0 Ω

As for the secondary network, we assumed a supply voltage, V_L, of 3 V set by a linear voltage regulator and R_L = 90 Ω. So, P_L = 100 mW results. From section 4.6.3.2, the minimum required power will be given at $V_{reg} = V_L$, being $P_{Load,req} \approx 126$ mW. From, (4.54), assuming $V_{reg} = V_L$, $R_{Load} \approx 90$ Ω for a SS topology series resonant tank. From [54], for the SP topology and bridge rectifier, we get

$$R_{\mathrm{Load}} = \left(1 + \frac{2V_{\mathrm{D}}}{V_{\mathrm{reg}}}\right)\frac{R_{\mathrm{reg}}}{2} \tag{B.1}$$

which, for $V_{reg} = V_L$, results in $R_{Load} \approx 57$ Ω.

Fig. B.1 shows the results for the SS topology at a resonant frequency of 40 kHz. In the legend, the sequence L_1/L_2 was adopted. $P_{Load,req}$, is marked with a straight line. As can be seen, $P_{Load,max}$ decreases when increasing L_2 from 1 mH to 10 mH due to the higher value of R_{L2}. From (4.21), this leads to a lower value of η_2 and, thus, from (4.26), to a lower value of $P_{Load,max}$. On the other hand, d_c increases due to the higher values of Q_{L2} (see Fig. 4.10) and Q_{Load} and, thus, from (4.31), of Q_2. An increase of L_1 produces a similar behavior. Now, R_{L1} increases which, from (4.26), reduces $P_{Load,max}$. The decrease of $P_{Load,max}$ is much more pronounced when increasing L_1 than when increasing L_2. At the same time, Q_{L1} and Q_S increase and, thus, from (4.28), Q_1, hence increasing d_c. Overall, the curve that leads to a higher d_{max} at 40 kHz is that corresponding to L_1 = 1 mH and L_2 = 10 mH, achieving a value of ca. 1.7 cm.

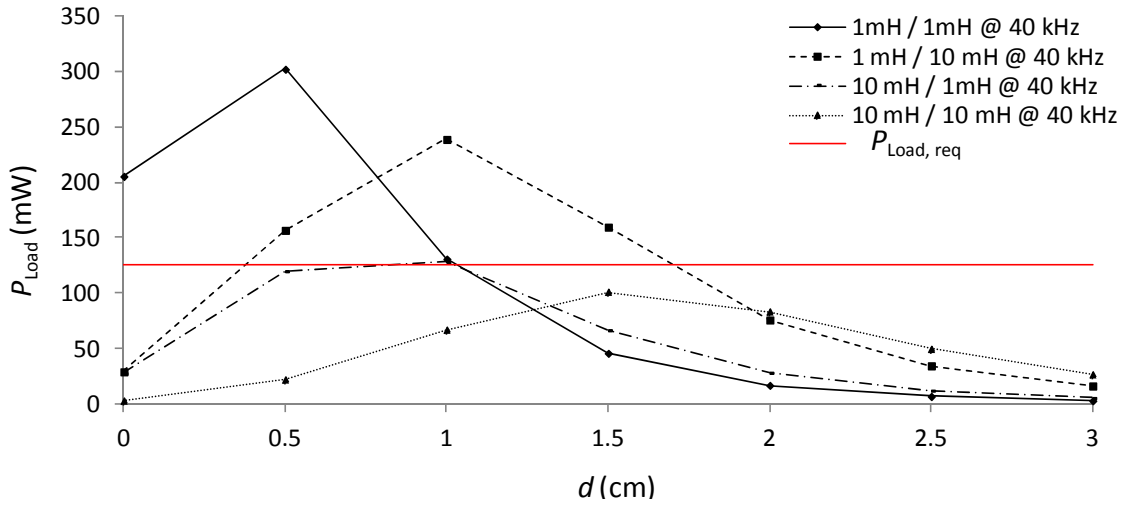

Fig. B.1 Computations of P_{Load} vs d for the SS topology and different combinations of inductances at 40 kHz.

Fig. B.2 shows the same cases of Fig. B.1 but for a resonance frequency of 120 kHz. An increase of frequency leads to an increase of the coil resistances. This leads both to an increase of R_1 and to a decrease of η_2 and, thus, from (4.26), to a decrease of $P_{Load,max}$. On the other hand, Q_s and Q_{Load} increase. As for the coil quality factors, they slightly decrease for the 1 mH coils

but increase for the 10 mH coils (see Fig. 4.10). The net result is an increase of d_c in all the cases. Even so, the only curve that surpass $P_{Load,req}$ ($L_1 = L_2 = 1$ mH) achieves a lower d_{max} than the best curve of Fig. B.1.

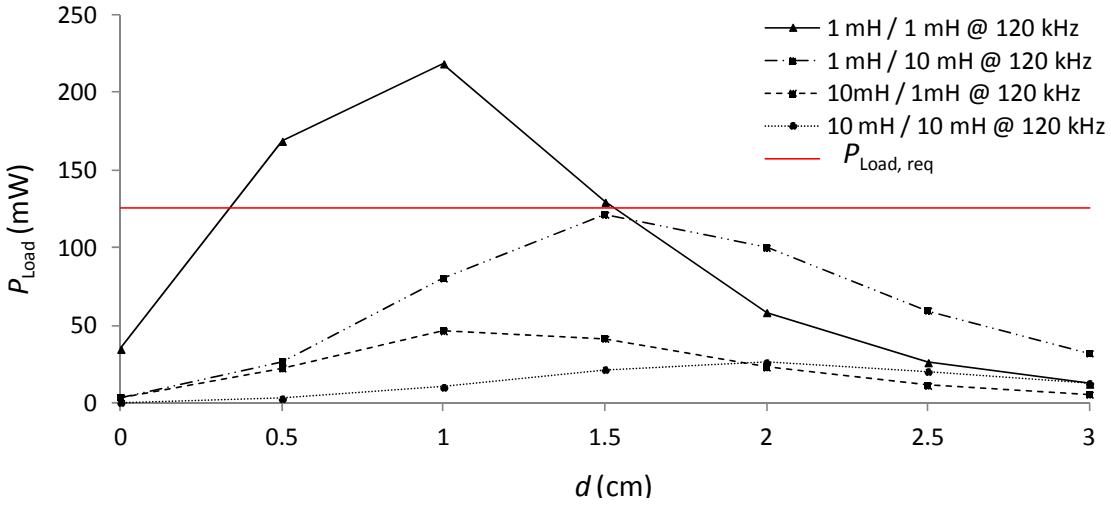

Fig. B.2 Computations of P_{Load} vs d for the SS topology and different combinations of inductances at 120 kHz.

Fig. B.3 and Fig. B.4 show P_{Load} for the resonant frequencies of 40 kHz and 120 kHz, respectively, when using the SP topology for the case where (4.12) and (4.13) are accomplished and with C_2 that of (4.42). In Fig. B.4, we only represented the results with L_2 = 10 µH, as (4.43) was not accomplished for L_2 = 100 µH. As can be seen, the achieved maximum distance is lower than that achieved with the SS topology. This is due to the lower quality factors of the coils used now for the secondary network, which leads to a lower d_c.

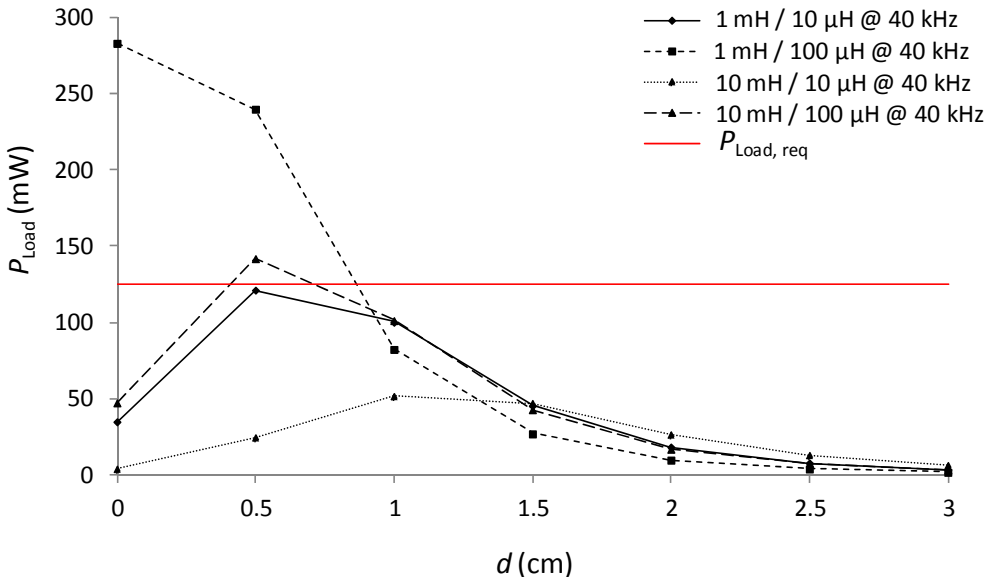

Fig. B.3 Computations of P_{Load} vs d for the SP topology and different combinations of inductances at 40 kHz.

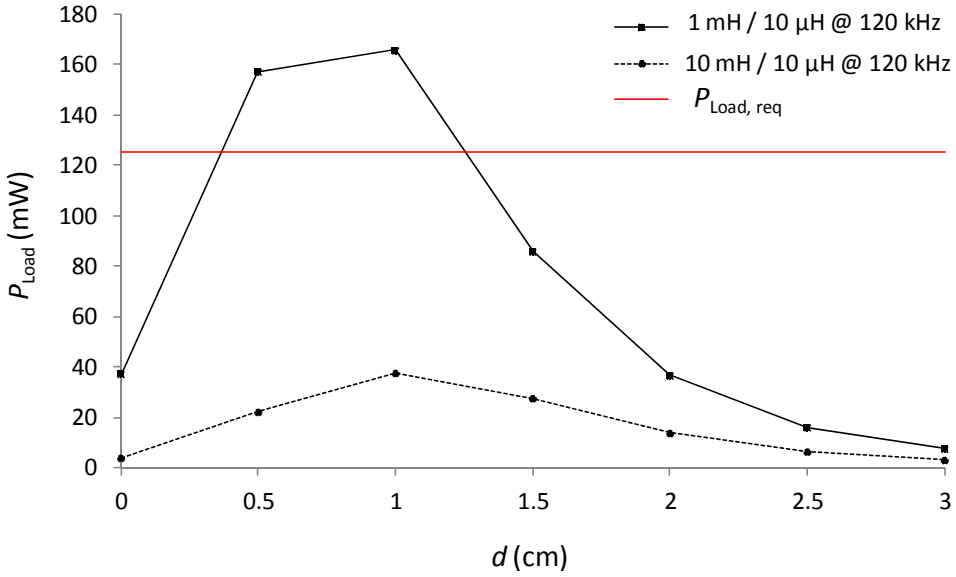

Fig. B.4 Computations of P_{Load} vs d for the SP topology and different combinations of inductances at 120 kHz.

Fig. B.5 shows the efficiency, η_T, for the best two cases, i.e. 1) L_1 = 1 mH, L_2 = 10 mH, f_r = 40 kHz, and 2) $L_1 = L_2$ = 1 mH, f_r = 120 kHz. As can be seen, efficiencies are similar for distances larger than 1 cm, being *ca*. 15 % at a distance of 1.5 cm. To increase the efficiency, a lower distance should be used. For example, an efficiency around 60 % can be achieved at a distance of 0.5 cm, still being P_{Load} higher than $P_{Load,req}$. Hereafter, the first case will only be further analyzed as it provides a larger powering distance (d_{max}) than the second case with the same efficiency.

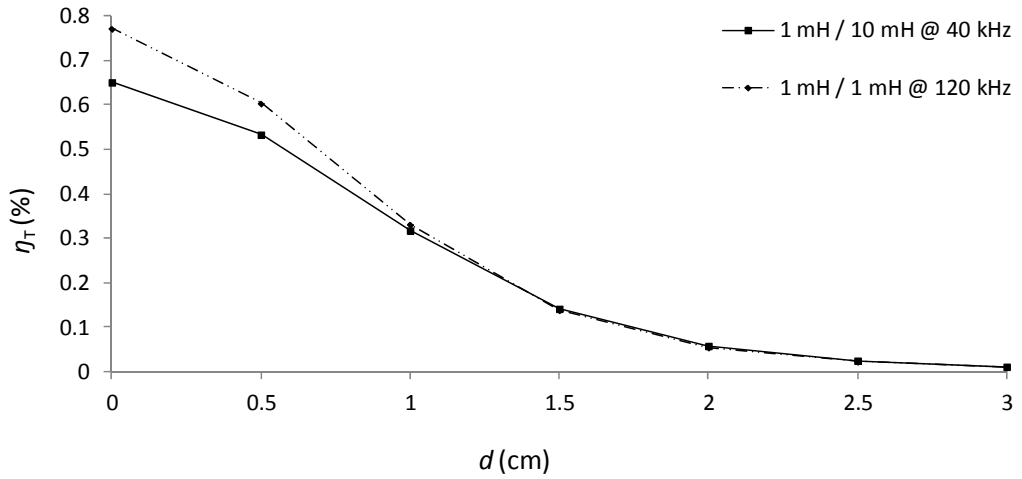

Fig. B.5 Overall efficiency for two cases: 1) L_1=1 mH, L_2=10 mH, f_r=40 kHz, and 2) L_1=L_2=1 mH, f_r=120 kHz.

For the selected case of 1 mH/10 mH @ 40 kHz more computations were carried out using (4.7). As capacitors we used the nominal values used later in the experimental setup (B.2), i.e. C_1 = 15 nF and C_2 = 1.5 nF. So, the resulting nominal value of the resonant frequency was 41.1 kHz. Fig. B.6 shows the effect of a mismatch of the operating frequency of the power amplifier (Fig. 4.11) with respect to the resonant frequency, given by (4.16). At distances lower than d_c, the resonant frequency does not provide the maximum power and two peaks appear at both sides of the resonant frequency. Thus, a frequency detuning of the power amplifier at these short distances can even be advantageous. On the other hand, for distances higher than d_c, the maximum power occurs at the resonant frequency and the delivered power begins to fall off steeply at both sides. A similar behavior was also shown in [69] and [74]. Further, we have checked that the half-power bandwidth is inversely proportional to the overall quality factor, i.e. $\sqrt{Q_1 Q_2}$. Thus, higher quality factors lead to narrower bandwidths, becoming the tuning of the driver frequency more tricky.

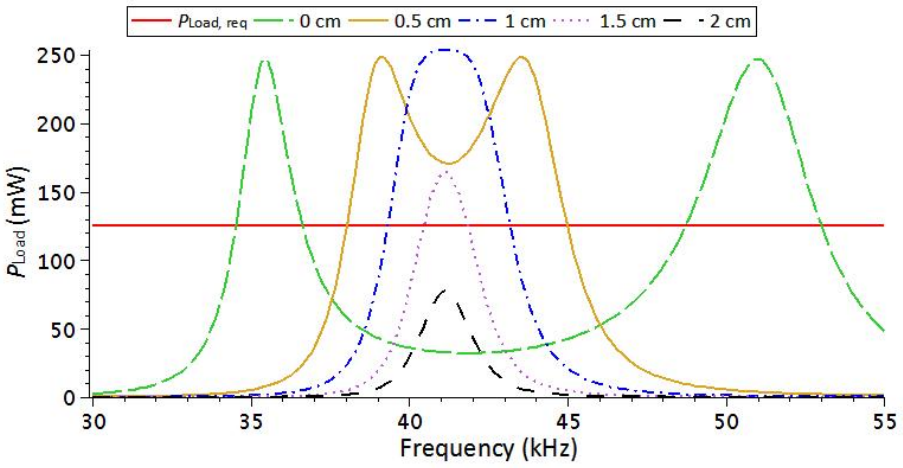

Fig. B.6 Computed P_{Load} vs the driver frequency at different distances.

Transmitting and receiving resonant frequencies can differ because of the tolerance and drift of the components used in the resonant tanks (capacitors and inductors). So, capacitors with a low temperature-drift should be selected. Fig. B.7 shows P_{Load} versus C_1 at different distances. The driver frequency is assumed to be fixed and equal to the resonant frequency of the receiving network and to that of the transmitting network for the nominal (central) value of C_1, i.e. 15 nF. At distances lower than d_c, the relative change of P_{Load} is low. Again, at distances higher than d_c, the width of the power curves is inversely proportional to the overall quality factor. From Fig. B.7 and for a distance of 1.5 cm, $P_{Load} > P_{Load,req}$ within a tolerance band of ±5.3 % around C_1 = 15 nF. Fig. B.8 shows the case where the varying parameter is C_2. Now, for a distance of 1.5 cm, $P_{Load} > P_{Load,req}$ within a tolerance band of ±3.8 % around C_2 = 1.5 nF (nominal value).

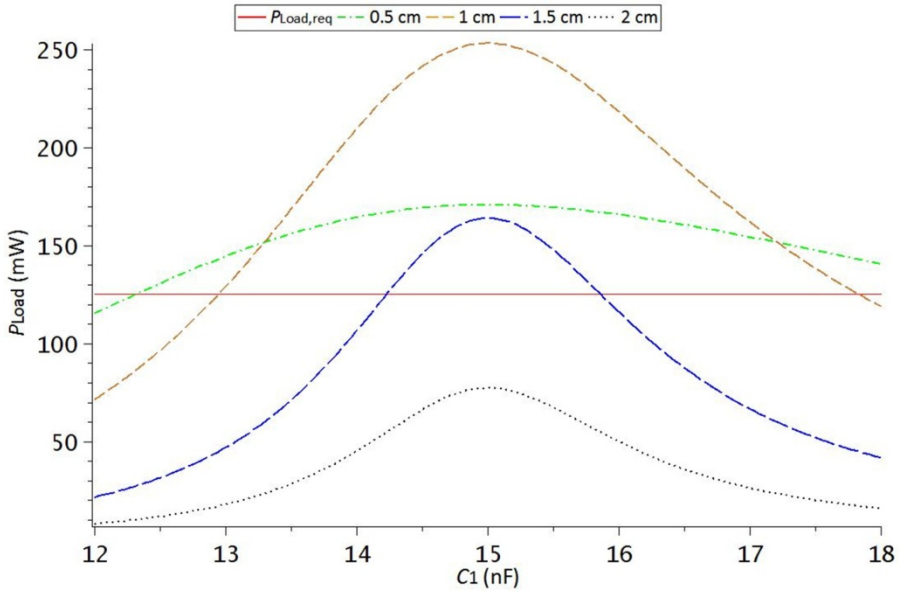

Fig. B.7 Computed P_{Load} vs.C_1 at different distances.

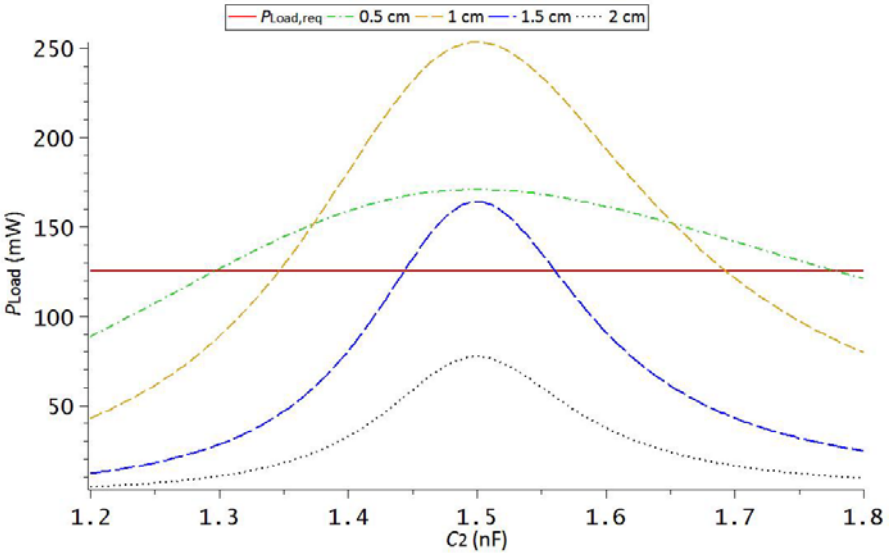

Fig. B.8 Computed P_{Load} vs. C_2 at different distances.

B.2 Experimental Results

We implemented the configuration that provides the maximum distance from the computations, i.e. L_1 = 1 mH, L_2 = 10 mH, f_r = 40 kHz, and the SS topology. Low temperature-drift capacitors were used with values C_1 = 15 nF and C_2= 1.5 nF. As for the secondary network, we first used the circuit shown in Fig. 4.4 with R_{Load} = 91 Ω (commercial value). Then, we used the circuit of Fig. 4.12 both with an R_L = 91 Ω and with the autonomous sensor described in section 4.6.1 connected at the output of the regulator.

The procedure to work at the resonance frequency was the following: first, the driver frequency was adjusted at the resonance frequency of the primary resonant tank by measuring a maximum in the voltage drop (measured with a floating oscilloscope) of R_p (= 10 Ω, see Table B.1). In this case, the secondary network was not present. Then, the secondary network was placed at a distance higher than the computed d_c in Fig. B.1 and was tuned by adjusting a capacitor trimmer (100 pF), placed in parallel with C_2, in order to achieve a maximum voltage drop in R_{Load}.

Load power was estimated by measuring the voltage drop across R_{Load} by using a floating oscilloscope. Fig. B.9 shows computed (reproduced from Fig. B.1) and experimental results. Both results show a good agreement. The distance range at which $P_{Load} > P_{Load,req}$ was [0.4 cm, 1.7 cm], in agreement with the computed results.

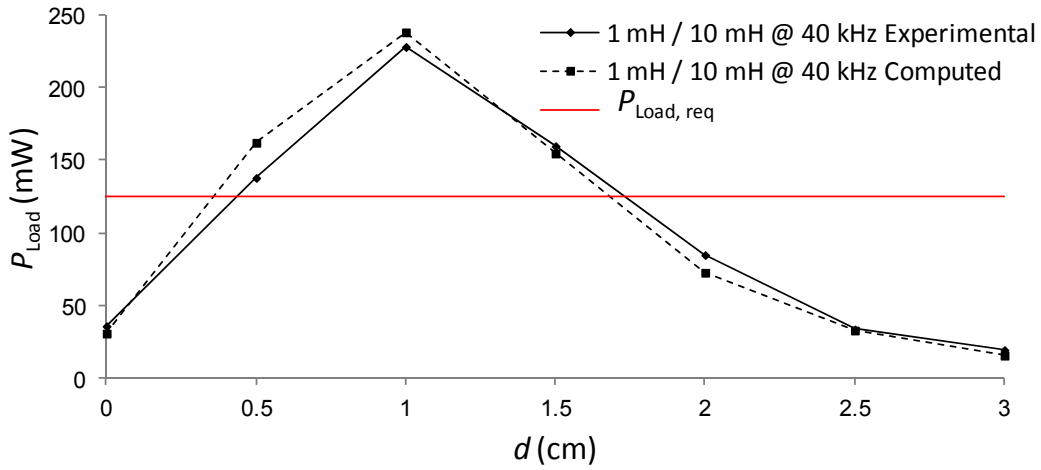

Fig. B.9 Computed and experimental results of P_{Load} @ 40 kHz with L_1=1 mH, L_2=10 mH, and R_{Load}=91 Ω (90 Ω for the computations).

In order to provide a suitable DC voltage to the load. Fig. B.10 shows the detailed circuit implementation used for the secondary network. As can be seen, a bridge rectifier was jointly used with a stabilization capacitor (C_d). An ensuing linear regulator (LP2980) was added to provide a voltage (V_L) of 3 V across the load (R_L = 91 Ω). A 10 V zener diode D_e was used for protecting the input of the linear regulator from overvoltage.

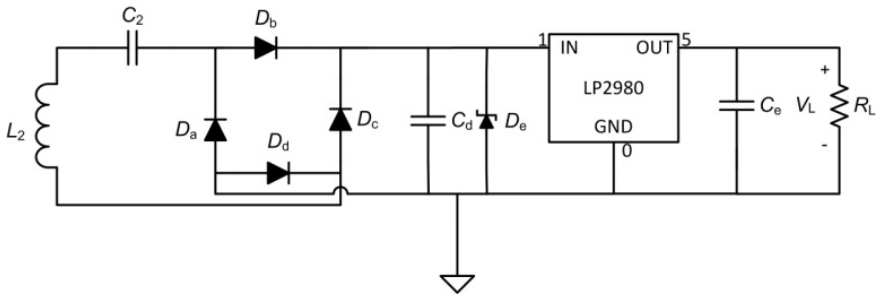

Fig. B.10 Schematic circuit of the secondary network used for the experimental setup.

Fig. B.11 shows V_L versus distance. For V_L = 3 V, a power of 100 mW was dissipated across R_L. As can be seen, the distance range at which V_L = 3 V was [0.5 cm, 1.7 cm], in agreement with the results of Fig. B.9. At distances lower than 0.5 cm, V_L achieved the required 3 V just by detuning the primary driver as predicted from Fig. B.6. Another alternative was to misalign the primary and secondary coils. This leads to a decrease of k and thus of d_c, hence increasing P_{Load} at the lowest distances.

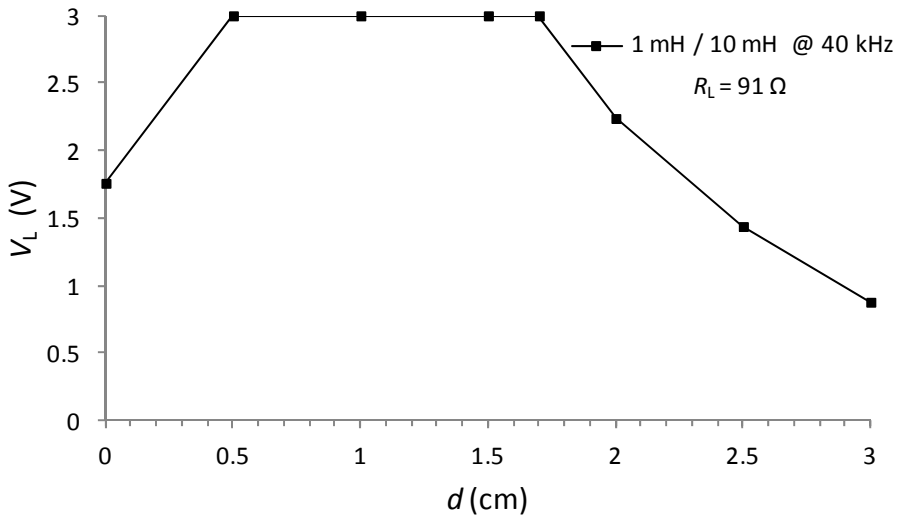

Fig. B.11 V_L @ 40 kHz L_1=1 mH, L_2=10 mH, and R_L=91 Ω for the secondary network.

Finally R_L was substituted by the autonomous sensor presented in section 4.6.1. Fig. 4.32 shows the experimental setup with the autonomous sensor (top board) that includes the occupancy and belt detectors. Another ETRX-2 device was connected to the USB port of a PC in order to receive and process the transmitted data. The autonomous sensor transmitted the data correctly up to a distance of 2.5 cm. This distance was larger than 1.7 cm as the transceiver part of the autonomous sensor worked properly down to a supply voltage of 1.8 V.

Appendix C Computations for the SS topology and Half-wave Rectifier

This appendix shows the graphs of P_{Load} versus R_{Load} for the five cases of Table 4.3 using the half-wave rectifier. The limiting values of R_{Load} are one quarter of that found for the bridge rectifier, i.e. 25.7 Ω, 25.2 Ω and 23.1 Ω for the linear shunt, linear series, and switching regulators, respectively. The respective power values are the same than that found for the bridge rectifier.

Fig. C.1 shows the results for case 1. Linear shunt as well as the linear series regulators provide five operating points from d = 0.5 cm to d = 2.5 cm. Buck regulators provide only 4 operating points from d = 0.5 cm to d = 2 cm. On the other hand, the switching boost regulator only provides one stable operating point at d = 2.5 cm.

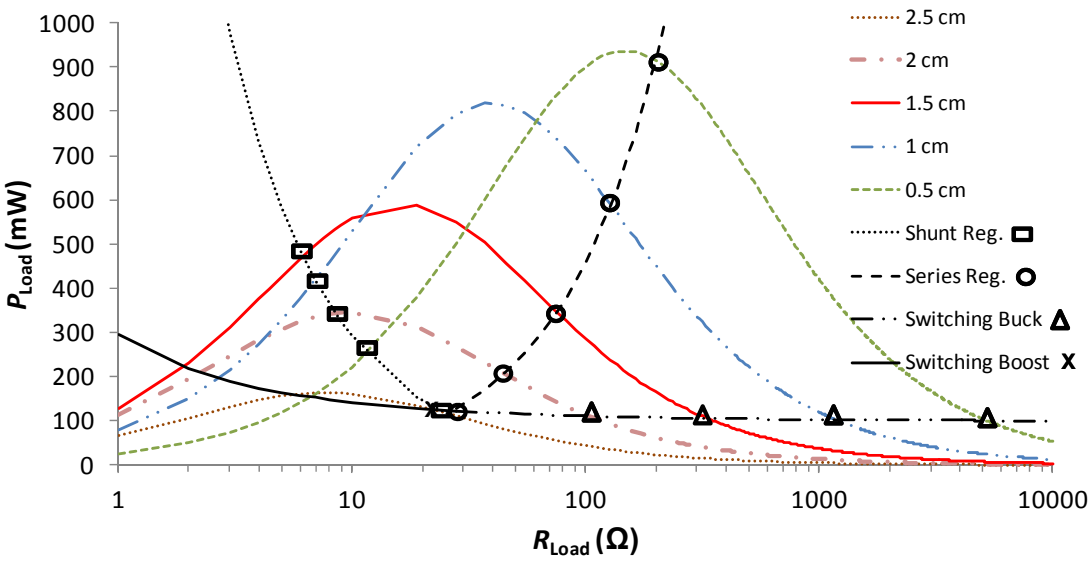

Fig. C.1 *Computed* P_{Load} vs R_{Load} for the four types of regulators at different distances (Case 1, half-wave rectifier).

Fig. C.2 shows case 2. Now, the linear and buck regulators achieve a larger distance, up to 3 cm. However, only the buck regulator is able to work at d = 0.5 cm. The switching boost regulator provides no stable operating point.

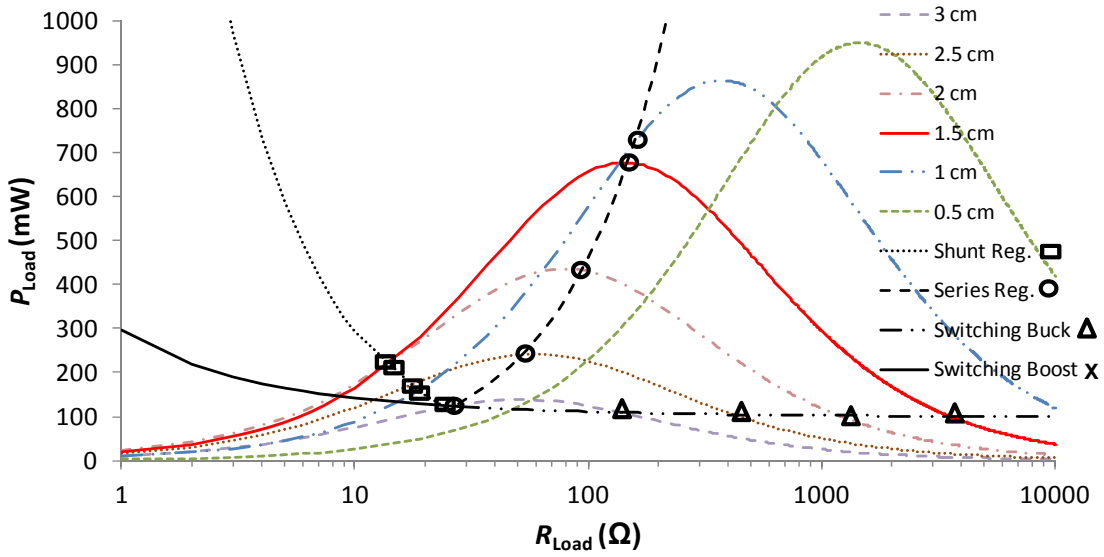

Fig. C.2 *Computed* P_{Load} vs R_{Load} for the four types of regulators at different distances (Case 2, half-wave rectifier)..

Fig. C.3 shows case 3. As can be seen, only two operating points are provided by the linear regulators at d = 1 cm and d = 1.5 cm and two points for the switching buck regulator at d = 0.5 cm and d = 1 cm. No operating point is found for the boost regulator and linear series regulator.

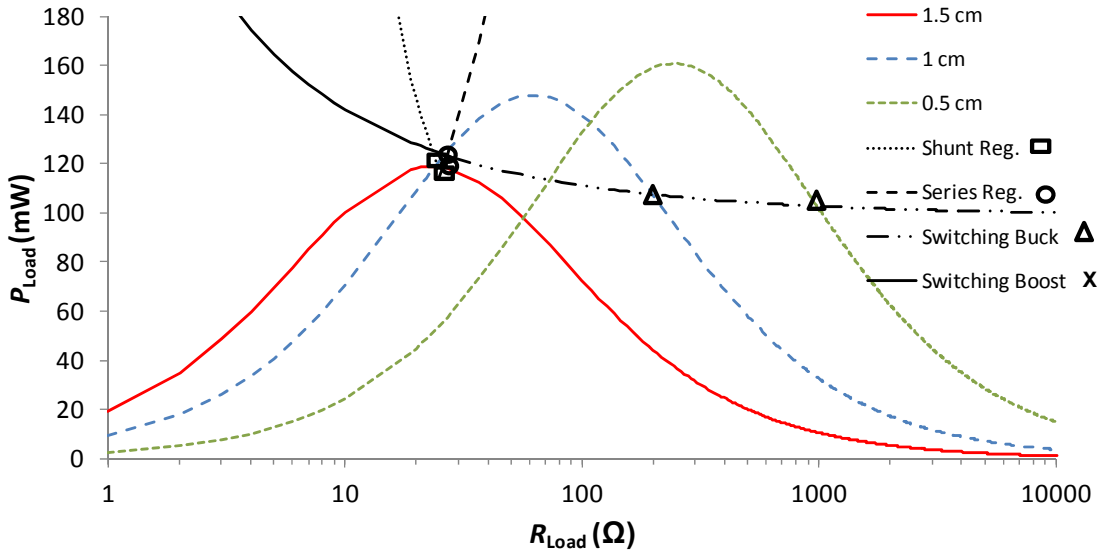

Fig. C.3 *Computed* P_{Load} vs R_{Load} for the four types of regulators at different distances (Case 3, half-wave rectifier).

Fig. C.4 shows case 4. Two operating points for the case 4 are provided by the linear shunt and series regulators at d = 1 cm and d = 1.5 cm and three points for the switching buck regulator at distances from d = 0.5 cm to d = 1.5 cm. No operating point is found for the boost regulator.

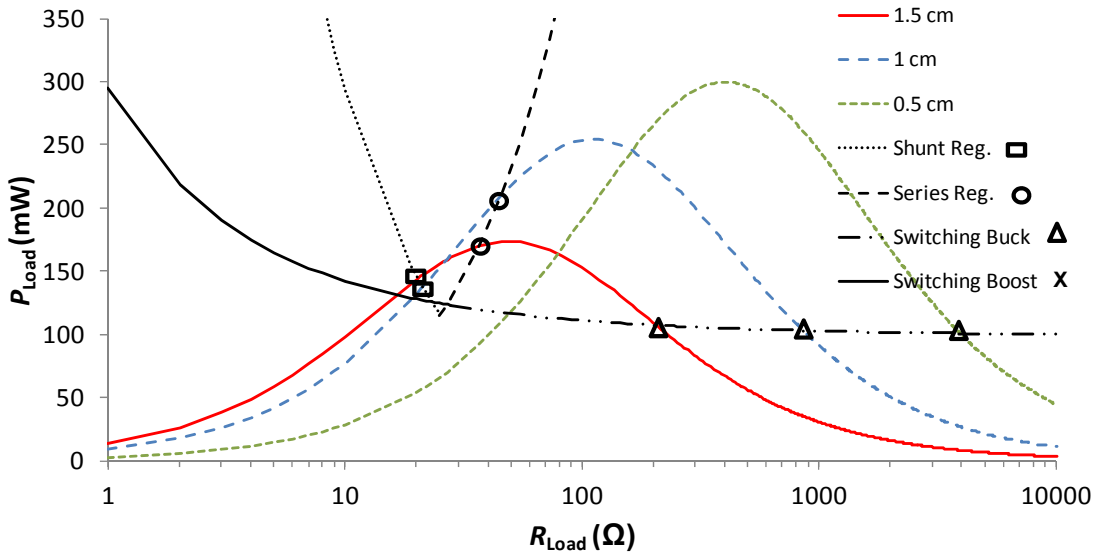

Fig. C.4 *Computed* P_{Load} vs R_{Load} for the four types of regulators at different distances (Case 4, half-wave rectifier).

Fig. C.5 shows case 5. No operating point exists for linear and switching boost regulators. Four operating point at distances from d = 0.5 cm to 2 cm are found for the switching buck regulator.

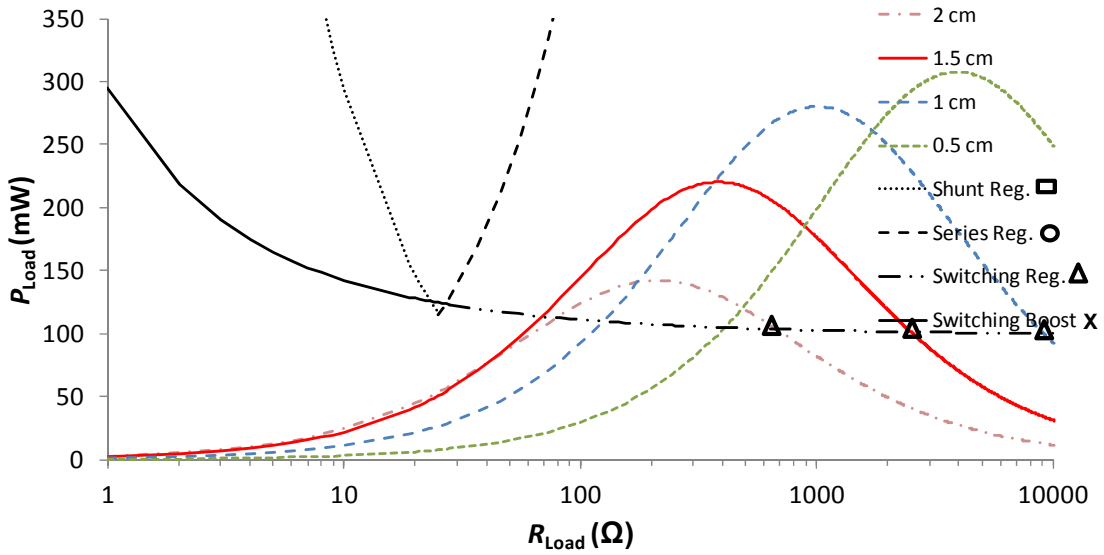

Fig. C.5 *Computed* P_{Load} vs R_{Load} for the four types of regulators at different distances (Case 5, half-wave rectifier).

Appendix D Partial Efficiencies for the Case 2 with Bridge Rectifier

This appendix shows the results of the partial efficiencies defined in (4.20), (4.21), (4.85), (4.87), and (4.88) for case 2 in Table 4.3 with the bridge rectifier.

Fig. D.1 shows the efficiencies for the linear shunt regulator. From Fig. 4.26, low values of R_{Load} are achieved and thus, at short distances, high values of R_{r} and η_1. From (4.86), $\eta_{\text{R}} \approx 0.8$.

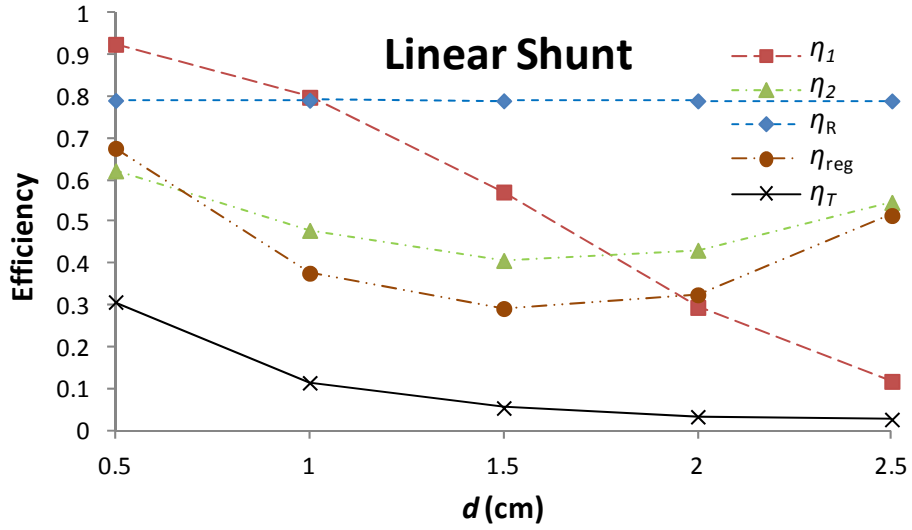

Fig. D.1 Efficiencies corresponding to the linear shunt regulator.

Fig. D.2 shows the efficiencies for the linear series regulator. From Fig. 4.26, higher values of R_{Load} are achieved, which lowers, a part of η_1, the value of η_{reg}.

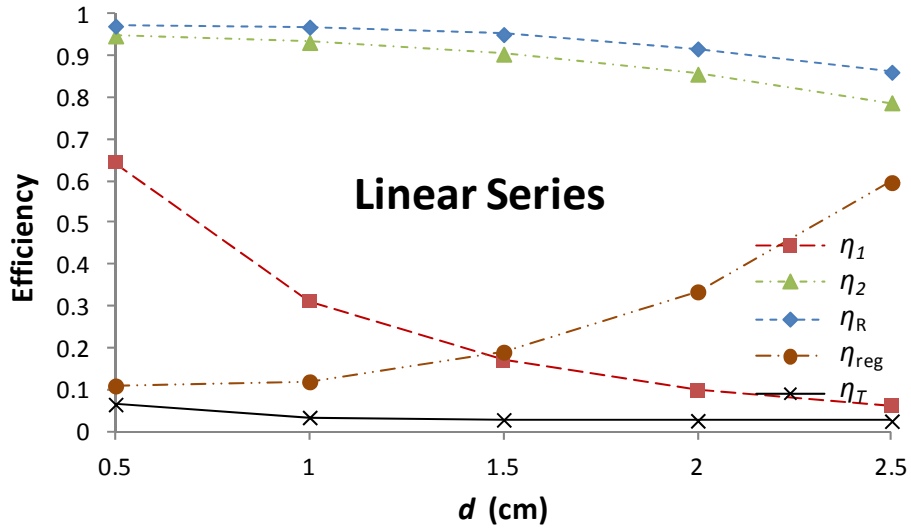

Fig. D.2 Efficiencies corresponding to the linear series regulator.

Fig. D.3 shows the efficiencies for the switching buck regulator. Now, from Fig. 4.26, very large values of R_{Load} are achieved and thus, extremely low values of R_r and η_1.

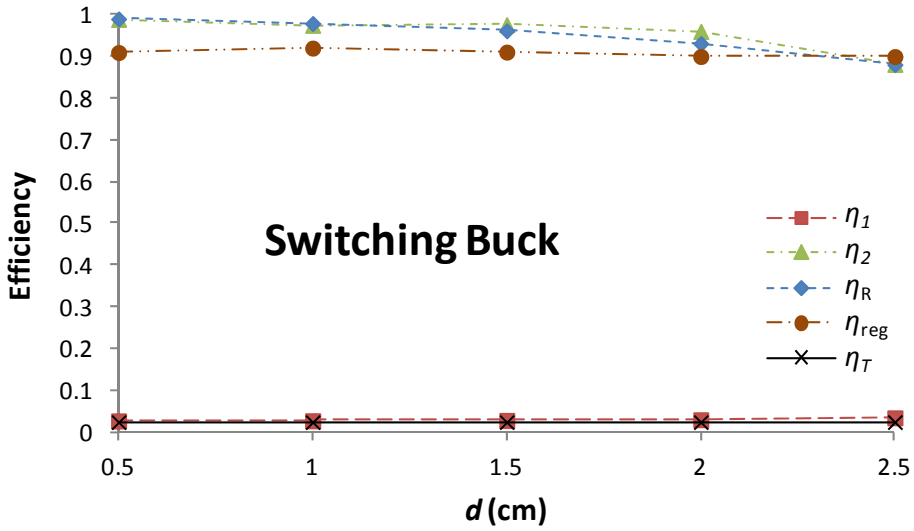

Fig. D.3. Efficiencies corresponding to the switching buck regulator.

Fig. D.4 shows the efficiencies when using a battery with V_B = 3 V. Now, η_1, η_2 and η_R are the same as for the shunt regulator. On the other hand, η_{reg} does not contribute and thus the achieved value η_T is higher than that of the shunt regulator.

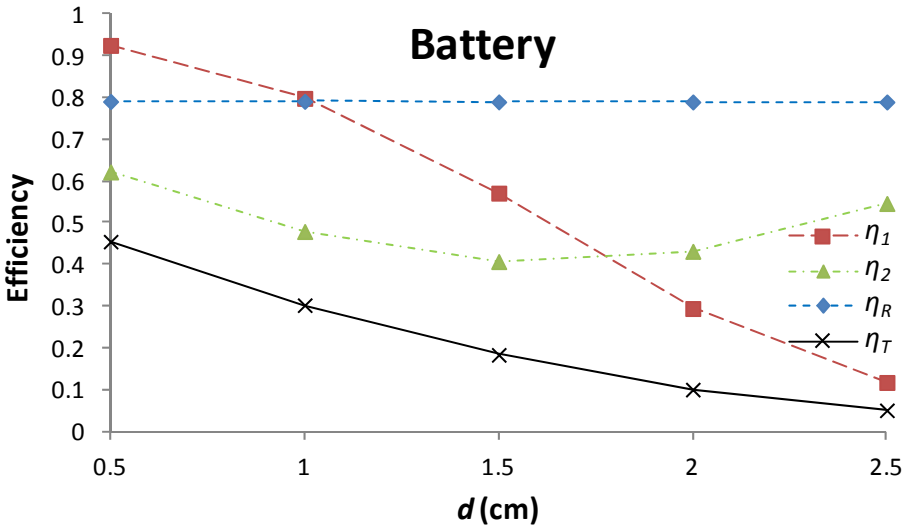

Fig. D.4 Efficiencies corresponding to the battery.

Appendix E Assessment of Exposure Limits to Time-varying *EMF*

According to the tables (Table 2.1, Table 2.2) provided by ICNIRP [55] we have developed one model for extracting conclusions on the field-tissue interaction and compliance with EM exposure regulations.

Fig. E.1 depicts an axisymmetric FE model of the 2 coils system (Fastron coils) embedded into a biological tissue plate. The resonant current was fixed to 0.725 A ($I_1 = V_1/R_1$ assuming the worst case for L_1 = 1 mH and R_1 = 7.45 Ω in Chapter 4) and considering a resonance frequency of 40 kHz. α-Fe determines the Ferrite areas with a relative permeability of μ_r = 2000. Biological tissue surrounds the coils with a conductivity of σ_{bio} = 0.85 S/m [91], which simulates the hypothetical case of someone touching the IPT system. This extreme case permits us to verify the degree compliance of the ICNIRP norms.

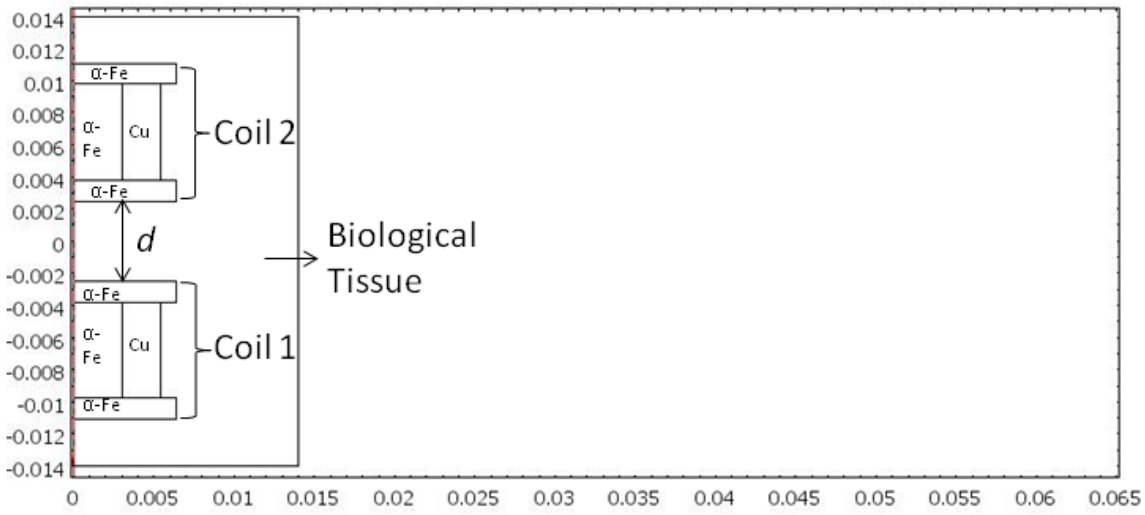

Fig. E.1 Cross-sectional plot of a pair of Fastron coils embedded into a biological tissue plate using axial axysimmetry with COMSOL Multiphysics.

The current density induced in the tissue according to [54] and derived from (2.2) is

$$J_{bio} = \sigma_{bio}\left|-j\omega A_{\varphi}\right| \tag{E.1}$$

The simulations demonstrates that biological tissue has a negligible influence on the magnetic field. With a distance d = 0 cm between the coils (worst case), the current density in the vicinity of the coil is lower than 80 mA/m^2 (upper limit, Table 2.1) at distances higher than 0.5 mm from the coils. We conclude that restrictions on induced current are respected because the system would be protected by a plastic box or similar.

Another important parameter is the called SAR (Specific Absorption Rate), approached by

$$SAR = \frac{1}{2}\sigma_{\text{bio}}\left|-j\omega A_{\varphi}\right|^2 \tag{E.2}$$

where the units are W/kg, assuming according to [54] a mass density of 1 kg/dm^3. In the simulation can be seen that modeled SAR is far less than the constraints of ICNIRP (≤ 0.4 W/kg).

Fig. E.2 and Fig. E.3 show the results obtained for our model for the E-field strength (V/m) and H-field strength (A/m), respectively. ICNIRP constraints at 40 KHz are 87 V/m and 5 A/m respectively. As can be seen, the levels of the electric field are far lower than the ICNIRP limit. On the other hand, outside the cross section area of the coils, at distances higher than 0.8 cm, the levels for the H field are lower than the limit permitted by the ICNIRP. We can thus consider the system safe and fully satisfying the constraints imposed by the ICNIRP because the minimum distance required is reasonable.

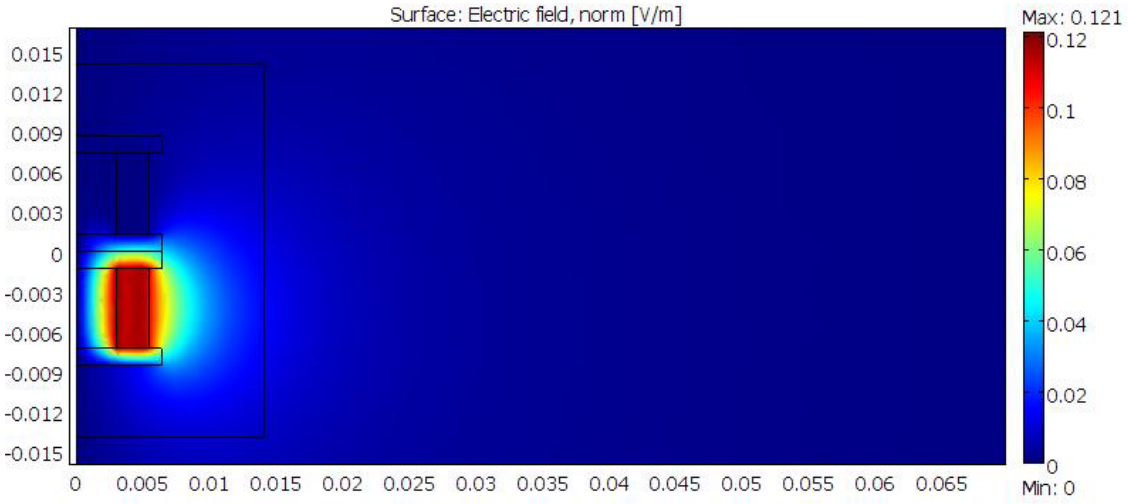

Fig. E.2 COMSOL simulation of the electric field strength.

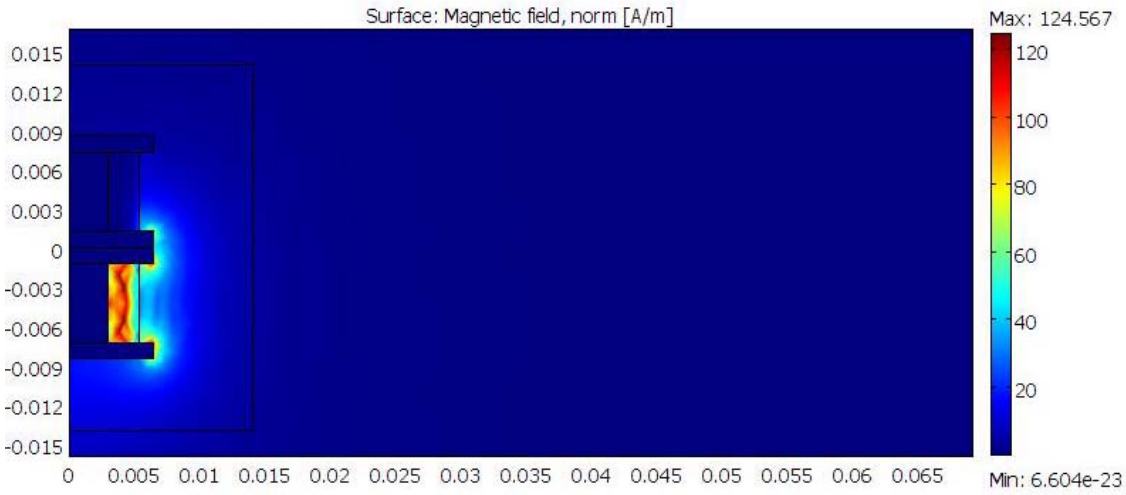

Fig. E.3 COMSOL simulation of the magnetic field strength.